Correlative Techniques for Lensless Fluorescence Imaging

Dissertation

zur Erlangung des Doktorgrades

an der Fakultät für Mathematik, Informatik

und Naturwissenschaften

Fachbereich Physik

der

Universität Hamburg

vorgelegt von

Lars Tamme Wollweber

Hamburg

2025

Gutachter/innen der Dissertation:	Prof. Dr. Henry N. Chapman Dr. Kartik Ayyer
Zusammensetzung der Prüfungskommission:	Prof. Dr. Franz X. Kärtner Prof. Dr. Henry N. Chapman Prof. Dr. Arwen Pearson Prof. Dr. Nina Rohringer Dr. Kartik Ayyer
Vorsitzende/r der Prüfungskommission:	Prof. Dr. Arwen Pearson
Datum der Disputation:	30.09.2025
Vorsitzender des Fach-Promotionsausschusses PHYSIK:	Prof. Dr. Wolfgang J. Parak
Leiter des Fachbereichs PHYSIK:	Prof. Dr. Markus Drescher
Dekan der Fakultät MIN:	Prof. Dr.-Ing. Norbert Ritter

Acknowledgements

First, I would like to thank my supervisor, Dr Kartik Ayyer, for the continuous support throughout my doctoral studies. Kartik has been a great mentor, always patient and willing to help. I am particularly grateful for his understanding of the challenges that come with balancing a Ph.D and family life. I could not have wished for a better supervisor.

Furthermore, I would like to thank my co-supervisor, Prof Henry Chapman, for his ever useful advice and discussions. Of course, I would also like to thank the entire team — Abhishek, Shen Zhou, Parichita, Omkar, Alba and Yulong — for their shared support, friendship and the many beamtimes and coffee breaks we had together. I would also like to thank Fabian Scheiba for all his help with the optical experiments.

Most importantly, I would like to thank my wife, Kristina, for her emotional support and understanding over the past years. She has always believed in my strengths and has been a constant source of motivation. Last but not least, I want to thank my children, Fridjof and Janne, for their smiles, laughter and pure love. They remind me of what truly matters in life — every single day.

Für Kristina, Fridjof und Janne.

Abstract

Incoherent Diffractive Imaging (IDI) is an emerging technique that utilizes intensity correlations of nominally incoherent fluorescence radiation to achieve element-specific imaging at the nanoscale. This method requires exposure and measurement times on the order of the fluorescence coherence time, which is now accessible through X-ray free-electron laser (XFEL) sources. While prior proof-of-principle experiments have established the capability of IDI for characterizing incident pulse profiles and durations, this work presents, for the first time, true imaging of individual nanostructures smaller than the incident beam. Through the use of conventional coherent diffractive imaging (CDI) for calibration and orientation determination, this study achieves the highest spatial-resolution structural reconstructions using IDI reported to date (20 nm). Additionally, IDI reveals new signatures of amplified spontaneous emission in copper nanoparticles.

The single particle approach further enables the investigation of nonlinear phenomena such as (reverse) saturable absorption over a broad range of incident fluences. By analyzing the statistical properties of the emitted fluorescence, an unprecedented self-gating effect is observed, with profound implications for IDI.

Building on the methodologies and challenges of IDI, this thesis introduces a novel technique: Spectral Incoherent Diffractive Imaging (SIDI). SIDI enables dark-field imaging of nanostructures with heterogeneous oxidation states by resolving shifts in the photoemission profiles. This allows independent imaging of the emitter distributions corresponding to each spectral line. In the X-ray domain, SIDI offers unique insights that go beyond the conventional combination of diffraction and X-ray emission spectroscopy (XES). Applied at XFELs, it holds promise as a versatile tool for exploring a wide range of systems, offering unprecedented opportunities for detailed characterization of heterogeneous nanostructures for catalysis and energy storage, including their ultrafast dynamics.

Finally, the prospects of extending IDI and SIDI to the visible regime at room temperature are discussed. In this context, the techniques could enable spatially resolved sensing of the local chemical environment at the nanoscale, offering new opportunities for studying material properties. However, our optical experiments reveal several fundamental challenges that limit the applicability of IDI and SIDI in the visible regime at room temperature.

Zusammenfassung

Inkohärente Diffraktive Bildgebung (IDI) ist eine aufstrebende Technik, die Intensitätskorrelationen von nominal inkohärenter Fluoreszenz nutzt, um elementspezifische Bildgebung im Nanomaßstab zu ermöglichen. Diese Methode erfordert Belichtungs- und Messzeiten in der Größenordnung der Kohärenzzeit der Fluoreszenz, die heute durch Freie Elektronen Röntgen Laser (XFEL) erreicht werden können. Während frühere Machbarkeitsstudien die Fähigkeit von IDI zur Charakterisierung von einfallenden Pulsprofilen und -dauern etabliert haben, zeigt diese Arbeit erstmals die Bildgebung von einzelnen Nanostrukturen, die kleiner sind als der einfallende Strahl. Durch den Einsatz der konventionellen kohärenten diffraktiven Bildgebung (CDI) zur Kalibrierung und Bestimmung der Teilchenorientierung werden in dieser Studie die bislang höchsten räumlichen Auflösungen in strukturellen Rekonstruktionen mit IDI erzielt (20 nm). Darüber hinaus zeigt IDI neue Signaturen von verstärkter spontaner Emission in Kupfernanopartikeln.
Der Ansatz der Einzelteilchen-Bildgebung ermöglicht zudem die Untersuchung nichtlinearer Phänomene wie (umgekehrte) sättigbare Absorption über einen weiten Bereich einfallender Fluenzen. Durch die Analyse der statistischen Eigenschaften der emittierten Fluoreszenz wird ein bislang unerreichter Selbst-Gating-Effekt beobachtet, der tiefgreifende Auswirkungen auf IDI hat.
Aufbauend auf den Methoden und Herausforderungen von IDI führt diese Arbeit eine neuartige Technik ein: Spektrale Inkohärente Diffraktive Bildgebung (SIDI). SIDI ermöglicht die Dunkelfeld-Bildgebung von Nanostrukturen mit heterogenen Oxidationszuständen, indem Verschiebungen in den Photoemissionsprofilen aufgelöst werden. Dies ermöglicht eine unabhängige Bildgebung der Emitterverteilungen, die zu jeder spektralen Linie gehören. Im Röntgenbereich bietet SIDI einzigartige Einblicke, die über die konventionelle Kombination von kohärenter Diffraktion und Röntgenemissionsspektroskopie (XES) hinausgehen. Angewendet an XFELs verspricht es ein vielseitiges Werkzeug zur Untersuchung einer breiten Palette von Systemen zu werden und eröffnet beispiellose Möglichkeiten für die detaillierte Charakterisierung heterogener Nanostrukturen in den Bereichen der Katalyse und Energiespeicherung, einschließlich ihrer ultraschnellen dynamischen Prozesse.
Schließlich werden die Perspektiven der Erweiterung von IDI und SIDI in den visuellen Bereich bei Raumtemperatur diskutiert. In diesem Zusammenhang

könnten diese Techniken die räumlich aufgelöste Messung der lokalen chemischen Umgebung im Nanomaßstab ermöglichen und neue Chancen für das Studium von Materialeigenschaften eröffnen. Unsere optischen Experimente zeigen jedoch grundlegende Einschränkungen auf, die die Anwendbarkeit von IDI und SIDI im sichtbaren Spektralbereich bei Raumtemperatur limitieren.

Contents

1 Introduction **1**

2 Theoretical Background **7**

2.1 Wave field propagation in free space 7

2.2 Light-matter interaction 10

2.2.1 Elastic Scattering 10

2.2.2 Inelastic Scattering 12

2.3 Single Particle Imaging 15

2.3.1 EMC algorithm 15

2.3.2 Absolute fluence estimation 17

2.3.3 Ewald Sphere 18

2.3.4 Solid angle and polarization correction 19

2.4 Coherence 20

2.4.1 Temporal coherence 20

2.4.2 Spatial coherence 21

2.5 Incoherent Diffractive Imaging 22

2.6 Speckles and photon statistics 25

2.7 Simulations 26

3 The Nature of Hard X-Ray Fluorescence from Nanoparticles under Extreme Conditions **29**

3.1 Single Particle Imaging and Fluorescence Experiment 29

3.1.1 Incident spectrum and pulse duration 31

3.2 Degree of second-order coherence of K_α fluorescence 32

3.3 IDI of single particles 37

3.4 (Reverse) Saturable Absorption 37

3.5 Photon statistics 41

3.6 Summary 42

4 Nanoscale X-Ray Imaging with High Spectral Sensitivity Using Fluorescence Intensity Correlations 45

4.1 Simulations 47
4.2 Coherence between K_α decay channels 49
4.3 Nanoscale mapping of oxidation states 51
4.4 Summary 53

5 Perspectives for Optical Sensing at Room Temperature Using Fluorescence Intensity Correlations 55

5.1 Experimental Setup and Methods 56
5.2 Detector characterization 59
5.3 2D IDI in the visible regime 61
5.4 SIDI in the visible regime 64
5.5 1D IDI 66
5.6 Challenges of Optical IDI 67

6 Conclusion 69

A The Nature of Hard X-Ray Fluorescence from Nanoparticles under Extreme Conditions 73

A.1 Sample preparation 73
A.2 Theoretical modelling of RSA 74

B Nanoscale X-Ray Imaging with High Spectral Sensitivity Using Fluorescence Intensity Correlations 75

B.1 Signal estimation 75

C Perspectives for Optical Sensing at Room Temperature Using Fluorescence Intensity Correlations 77

Bibliography 79

List of Publications 89

List of Figures 93

Chapter 1

Introduction

Imaging is a powerful tool for understanding the details of the world around us, from the smallest particles to the largest cosmic scales. While imaging helps us visualize large objects or nanoscale structures it also provides insights about the fundamental physical processes that otherwise would stay hidden.
A particularly powerful imaging tool is X-ray imaging due to the high penetration power of X-rays compared to e.g. optical light or electrons [1, 2]. This allows us to look inside objects and materials and is used in many fields, such as materials science, biology, medicine or environmental sciences [3]. When it comes to the imaging of small nanoscale objects, X-ray imaging is often limited by the numerical aperture (NA) and the focal spot size of the imaging system [4, 5]. To overcome these limitations of traditional X-ray imaging, diffraction-based techniques, such as *X-ray Crystallography* [6, 7] and *Coherent Diffractive Imaging* (CDI) [5] have been developed. Both techniques use the interference pattern produced by the elastic scattering of a coherent light field by the sample to determine its structure [8, 9]. However, the crystallization to a sufficiently large size of biological samples, such as membrane proteins, can be challenging [10], and the crystalline disorder due to thermal motion (Debye-Waller-factor) can lead to a significant loss of resolution in the resulting diffraction patterns [11]. In addition, the high dose deposited into the system by the incident X-ray beam leads to radiation damage within the first tens of femtoseconds, limiting the maximum achievable spatial resolution [12–14]. These challenges lead to the development of X-ray free electron lasers (XFELs), which are capable of producing extremely intense and short X-ray pulses [15, 16]. One of the key foundational goals of XFELs was to enable *Single particle imaging* (SPI) — the study of the structure and dynamics of single particles and biomolecules in their near-native state, without the

need for crystallization [17]. This is achieved by using the extremely high peak brilliance of XFELs to produce diffraction patterns from single inorganic particles [18], viruses [19, 20] or proteins[21], before they are destroyed by radiation damage [19, 22–24]. The resulting diffraction patterns can then be analyzed using advanced computational techniques to classify the data according to shape and particle orientation to ultimately reconstruct the three-dimensional structure of the underlying scattering object [25]. While SPI is nowadays a standardized technique for imaging small objects [18], the resolution achieved is still limited by the high gas scattering background which drowns the signal from the sample at high scattering angles, especially for biological samples [26].
In the imaging of heterostructures, the elemental contrast achieved through coherent diffraction techniques scales only with the square of the atomic number of the constituent elements [26, 27]. Poor elemental contrast and low specificity also used to be a common challenge in other imaging fields, such as bright-field microscopy, which paved the way for the development of dark-field imaging techniques, such as fluorescence microscopy [28]. Here, the fluorescence emitted from distinct elements is measured, providing full contrast.
Exploiting fluorescence in diffraction-based experiments, however, has long been considered impossible due to the incoherent nature of fluorescence photons which do not produce static interference patterns in the far field [29]. However, in 1954 the astronomers Hanbury Brown & Twiss [30] already demonstrated with their method called *Intensity interferometry* that thermal light can indeed contain information about the spatial distribution of the emitting object. Instead of measuring wave-field amplitudes (first-order coherence), Hanbury Brown & Twiss exploited the second-order intensity correlation to measure the angular extent of a star [30]. The only requirement for their technique was that the photons were detected on the same timescales as their coherence time — the time during which the relative phases are considered stable [31] — which is inversely related to the spectral width of the light field. They achieved this by using narrow band-pass filters to select only a small spectral range of the starlight.

With the advent of XFEL sources featuring ultra-short pulse durations on timescales similar to the coherence time of characteristic X-ray fluorescence emission lines, the possibility of using X-ray fluorescence for imaging has been revisited [33]. Classen *et al.* termed this novel imaging technique *Incoherent Diffractive Imaging* (IDI). IDI has the potential to bridge the critical resolution gap between local probes, such as *Extended X-ray Absorption Fine Structure* (EX-

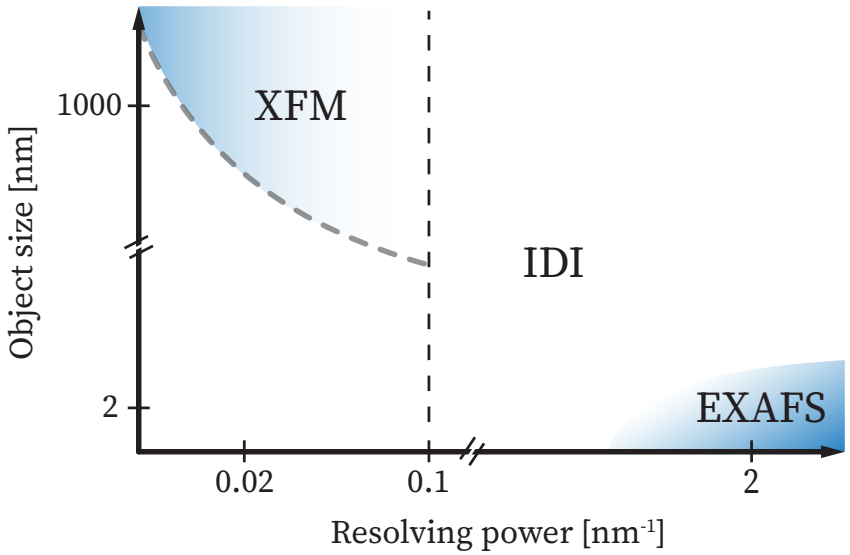


Figure 1.1: Schematic showing the resolution gap between EXAFS and XFM techniques, and the potential of Incoherent Diffractive Imaging (IDI) to bridge this gap. EXAFS provides atomic-scale but locally limited information about the surrounding structure of a specific element, while the resolution in XFM is limited by the spot size of the focused X-ray beam ($\sim 10\,\mathrm{nm}$) [32]. The gray dashed line indicates the quadratic relation between the object size and the resolving power, when scanning large 2D objects. IDI has the potential to provide high spatial resolution while maintaining elemental contrast, enabling dark-field imaging of substructures of a single element within heterostructures.

AFS), and lower-resolution *X-ray Fluorescence Microscopy* (XFM) techniques (see Fig. 1.1). EXAFS, originally a spectroscopic technique, can indirectly provide atomic-scale information about the local chemical environment of the absorbing atom. It achieves this by measuring the absorption of X-rays as a function of energy above an absorption edge. The resulting photoelectron, or equivalently the electron wave, which is emitted from the absorbing atom, can scatter from the surrounding atoms, leading to interference between the outgoing and the back-scattered waves. This interference causes oscillations in the absorption spectrum that can be used to extract information about the local atomic structure around the absorbing atom [34]. EXAFS is capable of achieving atomic-scale resolution, typically on the order of 1 Å, and can provide information about the local chemical environment, such as oxidation states and coordination numbers [35]. However, this technique provides only one-dimensional spatial information along the radial direction from the absorbing atom, and does not provide information about the

spatial distribution of elements within a sample. This makes EXAFS suitable for studying local structures around specific elements, but not for imaging of larger structures with complex elemental distributions. XFM, on the other hand, is a technique that uses X-ray fluorescence to provide elemental contrast in imaging. Specific elements can be excited above their respective absorption edge, leading to the emission of characteristic X-ray fluorescence photons. XFM is typically performed by raster-scanning a focused X-ray beam across the sample to produce spatially resolved elemental maps, which inherently limits its ability to capture ultrafast dynamics — unlike IDI or EXAFS. Consequently, although XFM facilitates the investigation of large-area samples, the need to maintain reasonable acquisition times typically necessitates the use of larger probe beams, thereby also compromising spatial resolution.
IDI has the potential to bridge this resolution gap between EXAFS and XFM by combining the high spatial resolution of a diffractive technique with the elemental contrast of fluorescence, enabling dark-field imaging of substructures of a single element within heterostructures. However, the signal-to-noise ratio (SNR) requirements in IDI are stringent and depend on factors such as the number of detected photons per frame, the incident pulse duration, and the dimensions and geometry of the emitting object [36]. To increase the SNR, IDI requires detecting a large number of photons per frame, making larger samples with more emitters more favorable. Conversely, smaller samples enhance reciprocal space sampling, which is essential for the reconstruction of the sample structure. Additionally, the sample size transverse to the sample-detector axis is constrained by the finite coherence length of the fluorescence emission [37]. If the transverse extent of the sample exceeds the coherence length, the contrast in IDI will be reduced significantly. These requirements for sample structure and data volume pose significant challenges for applying IDI across diverse systems. In pioneering proof-of-principle experiments, copper K_α fluorescence from bulk copper samples was used to determine the focus profile and the pulse duration of an XFEL pulse [38, 39]. This was followed by the imaging of non-trivial 2D structures using this approach [40].

This work continues the development of IDI by exploring new applications and techniques to enhance the range of applicable systems. Two major unresolved questions in the field are being addressed: (i) Is IDI of single particles feasible, and can thus be used for element-specific imaging of nanoparticles. The ability to image single particles using IDI would represent a significant advancement in the field of X-ray imaging and could provide valuable insights into the structure and

dynamics of nanoparticles. (ii) Can IDI be extended to the visible regime, enabling spatially-resolved sensing of the local chemical environment of the sample? In the visible regime, fluorescence-based dark-field imaging is well-established [28] and using sight-specific fluorescence emission has led to a number of advanced super-resolution microscopy techniques, such as *Structured Illumination Microscopy* (SIM) [41] and *Stimulated Emission Depletion* (STED) [42], that can provide resolutions beyond the Abbe limit. Recent advances, such as *Minflux*, even allow for the tracking of fluorophores in live cells with 1 nm precision while at the same time achieving a spatial resolution of 6 nm [43]. However, this technique requires a sparse distribution of fluorescent emitters, and is therefore not suitable for generic imaging of dense samples.

Therefore, the motivation for using IDI in the visible regime is predominantly to exploit its high spectral sensitivity to local changes in the chemical environment of the emitters, such as the oxidation state. The excitation and emission processes happen in the outer valence states of the atoms, where electrons can couple to phonons and the local electric and magnetic fields. This is a key difference to the X-ray regime, where the core-shell fluorescence is typically well-isolated from any environmental effects.

These characteristics are particularly important for applications in the field of materials science, where the local chemical environment can have a significant impact on the properties of the material [44–46]. Using IDI in the visible regime could therefore provide a new way to study the chemical properties of materials at the nanoscale, with potential applications in fields such as catalysis, energy storage, and environmental science.

The thesis is structured as follows:

In chapter 2 the basic principles of the imaging techniques CDI, SPI and IDI are introduced. In chapter 3, the first demonstration of IDI of single particles is presented. Moreover, the SPI approach allows us to investigate into the fundamental light-matter interactions and coherence properties of core-shell hard X-ray fluorescence.

To overcome the experimental challenges associated with IDI, and, furthermore, enable imaging that is sensitive to spectral line shifts associated with different oxidation states of the underlying emitters, we introduced a novel approach called *Spectral Incoherent Diffractive Imaging* (SIDI) that combines IDI with an analyzer crystal [47]. This approach, described in chapter 4, allows us to exploit the energy dependence of the emitted fluorescence, which is sensitive to the local chemical

environment and oxidation state of the sample which is not possible with traditional IDI techniques. In Chapter 5, the concepts of IDI are extended to the visible regime, exploring the feasibility of using IDI and SIDI as a new approach for optical sensing. Finally, in Chapter 6, the implications of these results are discussed, and future directions for research in this field are outlined.

Chapter 2

Theoretical Background

In this chapter, fundamental concepts of wave propagation in free space and light-matter interaction, including elastic and inelastic scattering in the X-ray regime are introduced. As many of these concepts are well-established and covered in textbooks [48, 49], the following sections will provide a concise summary. Additionally, different imaging techniques and their specific theoretical backgrounds are discussed.

2.1 Wave field propagation in free space

Let's consider a wave field $\psi(\boldsymbol{r}, t)$ propagating in free space with a frequency ω, using the scalar theory:

$$\psi(\boldsymbol{r}, t) = \psi(\boldsymbol{r}) e^{-i\omega t} \tag{2.1}$$

In the X-ray regime the temporal amplitude of the wave field oscillates at a frequency $w > 1.5 \times 10^{18} \mathrm{s}^{-1}$, which is much faster than the time resolution of any detector. Hence, we can neglect the time-dependence of the wave field and consider only the spatial part $\psi(\boldsymbol{r})$. This is called the time-independent wave field. The wave field $\psi(\boldsymbol{r})$ satisfies the time-independent homogeneous Helmholtz equation:

$$\left(\nabla^2 + k^2\right) \psi(\boldsymbol{r}) = 0, \tag{2.2}$$

where $k = |\mathbf{k}|$ is the modulus of the so-called wave vector, which is related to the wavelength λ of the wave field by $k = \frac{2\pi}{\lambda}$.

A solution for equation 2.2 is given by plane waves:

$$\psi(\boldsymbol{r}) = e^{i\boldsymbol{k}\cdot\boldsymbol{r}} = e^{i(k_x x + k_y y + k_z z)}. \tag{2.3}$$

Let's assume that the wave field is propagating in the positive z-direction, then we can separate the propagated and unpropagated parts using $k^2 = k_x^2 + k_y^2 + k_z^2$:

$$\psi(x, y, z) = e^{i(k_x x + k_y y)} \cdot e^{iz\sqrt{k^2 - k_x^2 - k_y^2}}. \tag{2.4}$$

The unpropagated wave field can be decomposed into plane waves using the Fourier transform:

$$\psi(x, y, z = 0) = \frac{1}{2\pi} \iint_{-\infty}^{\infty} \tilde{\psi}(k_x, k_y, z = 0) e^{i(k_x x + k_y y)} dk_x dk_y, \tag{2.5}$$

where $\tilde{\psi}(k_x, k_y, z = 0)$ is the Fourier transform of the wave field $\psi(x, y, z = 0)$. The wave field at $z > 0$ can be obtained by multiplying the Fourier transform with the free-space propagator $e^{iz\sqrt{k^2 - k_x^2 - k_y^2}}$:

$$\psi(x, y, z) = \frac{1}{2\pi} \iint_{-\infty}^{\infty} \tilde{\psi}(k_x, k_y, z = 0) e^{i(k_x x + k_y y)} e^{iz\sqrt{k^2 - k_x^2 - k_y^2}} dk_x dk_y. \tag{2.6}$$

Using the Fourier-convolution theorem[1], we can write the wave field at $z > 0$ as a convolution of the Fourier transform of the wave field at $z = 0$ with the propagator:

$$\begin{aligned} \psi(x, y, z) &= \psi(x, y, z = 0) * \frac{1}{2\pi} \iint_{-\infty}^{\infty} e^{iz\sqrt{k^2 - k_x^2 - k_y^2}} e^{i(k_x x + k_y y)} dk_x dk_y \\ &= \psi(x, y, z = 0) * P_{\mathrm{H}}, \end{aligned} \tag{2.7}$$

[1] The Fourier-convolution theorem states: $\mathcal{F}[f(x) * g(x)] = \mathcal{F}[f(x)] \cdot \mathcal{F}[g(x)]$, where $*$ is the convolution operator.

where P_{H} is the so-called Helmholtz propagator. Let us now apply the paraxial approximation, which states that the wave field deviates only slightly from the optical axis: $k_z^2 \gg k_x^2 + k_y^2$. In this case, we can approximate the square root in the propagator of equation 2.7 using the Taylor expansion:

$$\sqrt{k^2 - k_x^2 - k_y^2} \approx k - \frac{k_x^2 + k_y^2}{2k}. \tag{2.8}$$

Hence, the propagator can be rewritten as:

$$P_{\mathrm{H}} = \frac{1}{2\pi} \iint_{-\infty}^{\infty} e^{ikz} e^{-iz\frac{k_x^2+k_y^2}{2k}} e^{i(k_x x + k_y y)} dk_x dk_y. \tag{2.9}$$

The integrals can now be solved analytically and yield the so-called Fresnel propagator:

$$P_{\mathrm{F}} = \frac{-ik}{2\pi z} e^{ikz} e^{i\frac{k}{2z}(x^2+y^2)}, \tag{2.10}$$

which describes the paraxial equivalent of the Helmholtz propagator and can likewise be used to propagate the wave field in free space. Consequently, equation 2.7 becomes:

$$\begin{aligned} \psi(x,y,z) &\approx \frac{-ik}{2\pi z} e^{ikz} \iint_{-\infty}^{\infty} \psi(x,y,z=0) e^{i\frac{k}{2z}\left((x-x')^2+(y-y')^2\right)} dx' dy' \\ &= \frac{-ik}{2\pi z} e^{ikz} e^{i\frac{k}{2z}(x^2+y^2)} \iint_{-\infty}^{\infty} \psi(x,y,0) e^{-i\frac{k}{z}(xx'+yy')} e^{i\frac{k}{2z}\left((x')^2+(y')^2\right)} dx' dy'. \end{aligned} \tag{2.11}$$

Now, if the propagation distance z is large compared to the transverse dimensions of the wave field at $z = 0$, we can neglect the second term in the exponent of the Fresnel propagator. This is called the far-field approximation or Fraunhofer approximation. In this case, the wave field can be approximated as:

$$\psi(x,y,z) \approx \frac{-ik}{2\pi z} e^{ikz} e^{i\frac{k}{2z}(x^2+y^2)} \tilde{\psi}\left(k_x = \frac{kx}{z}, k_y = \frac{ky}{z}, z = 0\right). \tag{2.12}$$

Consequently, measuring intensities $I = |\psi|^2$ in the far-field is equivalent to measuring the Fourier transform of the wave field at $z = 0$.
This approximation will be used throughout this work to relate measured intensities in the far-field to the underlying wave field at the sample position.

2.2 Light-matter interaction

There are two main types of interactions between X-rays and matter: elastic and inelastic scattering. Elastic scattering is the process where the energy of the X-ray photon is conserved, while in inelastic scattering the energy of the X-ray photon is transferred to the sample. Inelastic scattering processes include photoabsorption, Compton scattering and pair production.

2.2.1 Elastic Scattering

Let's apply the approximations of section 2.1 to the elastic scattering ($|\boldsymbol{k}_{in}| = |\boldsymbol{k}_{out}|$) of X-rays by a sample with refractive index $n(\boldsymbol{r})$. The Helmholtz equation 2.2 can be rewritten as:

$$\left(\nabla^2 + k^2 n^2(\boldsymbol{r})\right) \psi(\boldsymbol{r}) = 0, \tag{2.13}$$

which yields the inhomogeneous Helmholtz equation:

$$\left(\nabla^2 + k^2\right) \psi(\boldsymbol{r}) = k^2 \left(1 - n^2(\boldsymbol{r})\right) \psi(\boldsymbol{r}). \tag{2.14}$$

Differential equations of this form can be solved by convolving the right-hand side of equation 2.14 with the so-called Green's function $G(\boldsymbol{r})$:

$$\psi(\boldsymbol{r}) = \psi_0(\boldsymbol{r}) - \frac{k^2}{4\pi} \iiint_{-\infty}^{\infty} \left(1 - n^2(\boldsymbol{r})\right) \psi(\boldsymbol{r'}) G(\boldsymbol{r} - \boldsymbol{r'}) d^3r', \tag{2.15}$$

where $\psi_0(\boldsymbol{r})$ is the solution of the homogeneous Helmholtz equation 2.2. The Green's function is the impulse response function, which represents the solution for the inhomogeneous Helmholtz equation of the kind:

$$\begin{aligned}\left(\nabla^2 + k^2\right) G(\boldsymbol{r}) &= -4\pi\delta(\boldsymbol{r}) \\ \Rightarrow G(\boldsymbol{r}) &= \frac{e^{\pm ikr}}{r}.\end{aligned} \tag{2.16}$$

The solution for the Green's function has the shape of a spherical wave, which, in the case of a positive sign in the exponent, corresponds to an outgoing wave. Equation 2.15 can now be solved by applying *perturbation theory* [50], a common approach in quantum mechanics, which allows us to iteratively solve for $\psi(\boldsymbol{r})$, starting with the initial guess $\psi_0(\boldsymbol{r})$:

$$\begin{aligned}\psi(\boldsymbol{r}) = \psi_0(\boldsymbol{r}) &- \frac{k^2}{4\pi} \iiint_{-\infty}^{\infty} \left(1 - n^2(\boldsymbol{r'})\right) \psi_0(\boldsymbol{r'}) G(\boldsymbol{r} - \boldsymbol{r'}) d^3r' \\ &+ \frac{k^4}{16\pi^2} \iiint_{-\infty}^{\infty} \iiint_{-\infty}^{\infty} \left(1 - n^2(\boldsymbol{r'})\right) \left(1 - n^2(\boldsymbol{r''})\right) \psi_0(\boldsymbol{r''}) \\ &\quad \cdot G(\boldsymbol{r} - \boldsymbol{r'}) G(\boldsymbol{r'} - \boldsymbol{r''}) d^3r'' d^3r' \\ &- \ \ldots\end{aligned} \tag{2.17}$$

For weak scatterers ($1 - n^2(\boldsymbol{r}) \ll 1$), the first-order term is dominant, and we can neglect the higher-order terms. This first Born approximation [51] is based on the assumption that the photons are only scattered once when interacting with the sample (also known as *kinematic diffraction* [52]). For an incident plane wave $\psi_0(\boldsymbol{r}) = e^{i\boldsymbol{k}_0\boldsymbol{r}}$, we obtain:

$$\psi(\boldsymbol{r}) = e^{i\boldsymbol{k}_0\boldsymbol{r}} - \frac{k^2}{4\pi} \iiint_{-\infty}^{\infty} \left(1 - n^2(\boldsymbol{r'})\right) e^{i\boldsymbol{k}_0\boldsymbol{r'}} \frac{e^{\pm ik|\boldsymbol{r} - \boldsymbol{r'}|}}{|\boldsymbol{r} - \boldsymbol{r'}|} d^3r'. \tag{2.18}$$

Now, we can apply the Fraunhofer (far-field) approximation and assume that the scattering object is compact and small compared to the distance where the wave field is evaluated: $n(\boldsymbol{r}) \neq 1$ only for $r' \ll r$. This leads to the following approximation:

$$\begin{aligned}|\boldsymbol{r}-\boldsymbol{r'}| &= \sqrt{x^2+y^2+z^2+x'^2+y'^2+z'^2-2(xx'+yy'+zz')} \\ &\approx \sqrt{r^2-2\boldsymbol{r}\boldsymbol{r'}} \\ &\approx r^2-\boldsymbol{r}\boldsymbol{r'}. \end{aligned} \tag{2.19}$$

Thus, the wave field can be expressed as:

$$\psi(\boldsymbol{r}) = e^{ikr} + \frac{k^2 e^{i\boldsymbol{k_f}\boldsymbol{r}}}{4\pi r} \iiint_{-\infty}^{\infty} \left(n^2(\boldsymbol{r'})-1\right) e^{i(\boldsymbol{k_f}-\boldsymbol{k}_0)\boldsymbol{r'}} d^3r', \tag{2.20}$$

where $\boldsymbol{k_f}$ is the scattered wave vector. Using the relation between the refractive index and the electron density $\rho(\boldsymbol{r}) \propto (n^2(\boldsymbol{r})-1)$ [53], we can see that the scattered wavefunction in the far-field is proportional to the Fourier transform of the electron density:

$$\psi(\boldsymbol{r}) \propto \iiint_{-\infty}^{\infty} \rho(\boldsymbol{r}) e^{i(\boldsymbol{k_f}-\boldsymbol{k}_0)\boldsymbol{r'}} d^3r'. \tag{2.21}$$

This relationship is the fundamental principle of coherent X-ray scattering and is the basis for many imaging techniques, such as CDI. It allows one to unveil the spatial distribution of the electron density of the underlying object from the scattered wave field. It shall be pointed out that only a two-dimensional subset of spatial frequencies contribute to the three-dimensional Fourier transform — the points in Fourier space that satisfy the relation $|\boldsymbol{k_f}| = |\boldsymbol{k}_0|$ form a two-dimensional surface, the so-called Ewald sphere (see section 2.3.3).
In X-ray experiments only the intensities of scattered photons can be measured and the phase information of $\psi(\boldsymbol{r})$ remains unknown. This so-called *phase problem* is a central challenge in coherent X-ray imaging, but can be solved using iterative phase retrieval algorithms [54, 55]. In this work, we focus only on the measurement and reconstruction of the scattered intensities as the phase retrieval can be treated as a separate problem.

2.2.2 Inelastic Scattering

The two primary inelastic scattering processes at photon energies in the lower keV-range are Compton scattering and photoabsorption. In Compton scattering, the

energy of an incoming X-ray photon is partially transferred to an electron, which is then ejected from the atom. In photoabsorption, the X-ray photon is fully absorbed by the atom, which then can follow two distinct relaxation processes — Auger-Meitner decay and fluorescence emission. In the scope of this thesis, we will focus on photoabsorption only, as it is the dominant inelastic scattering process for X-ray photons with energies below 20 keV [53]. The attenuation of X-rays in matter in an infinitesimal sheet of thickness dz at depth z can be described by the Beer-Bouguer-Lambert law:

$$-dI = I(z)\mu dz, \tag{2.22}$$

which leads to the exponential attenuation law:

$$I(z) = I_0 e^{-\mu z}. \tag{2.23}$$

The number of absorption events is proportional to I, the number of atoms per unit area $\rho_{at}dz$, and the absorption cross-section σ_a:

$$I(z)\rho_{at}dz\sigma_a = I(z)\mu dz. \tag{2.24}$$

Thus, the linear absorption coefficient μ is proportional to the absorption cross-section:

$$\mu = \left(\frac{\rho_m N_A}{M}\right)\sigma_a, \tag{2.25}$$

where ρ_m is the mass density, N_A is Avogadro's number, and M is the molar mass.

When an X-ray photon interacts with an inner atom shell, the electron is ejected and a hole is left in that shell. The hole is subsequently filled by an electron from a higher shell and the energy difference associated with the two energy levels is released via two decay channels — fluorescence emission and Auger-Meitner-decay. In fluorescence emission, the energy is released as a characteristic X-ray photon, whereas in Auger–Meitner decay, it is carried away by an Auger electron. This electron can then interact with surrounding atoms, triggering an ionization cascade that may ultimately lead to highly ionized neighboring atoms. The energy

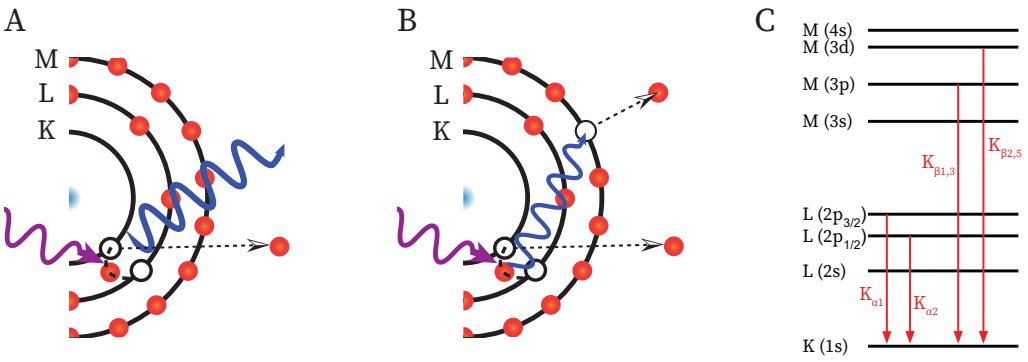


Figure 2.1: Atomic relaxation processes after photoionization: (**A**) Fluorescence emission and (**B**) Auger-Meitner-decay. (**C**) Characteristic X-ray fluorescence emission lines and their corresponding electronic energy levels for copper.

levels of the atom and the inter-level transitions that correspond to the characteristic X-ray emission lines are shown schematically in Figure 2.1.
Table 2.1 lists the important specifications of these emission lines, namely the central energy, their relative contribution to the full emission spectrum, the respective widths and the corresponding coherence times τ_c. For the K_α emission, we calculate the coherence for both sub-lines $K_{\alpha1}$ and $K_{\alpha2}$ combined, as these lines can typically not be distinguished without a spectrometer:

$$\tau_{c,K_{\alpha1,2}} = \frac{2\hbar}{\frac{2}{3}\Gamma_{K_{\alpha1}} + \frac{1}{3}\Gamma_{K_{\alpha2}}} \tag{2.26}$$

Table 2.1: Characteristic X-ray emission line energies, relative intensities, spectral widths and corresponding coherence times of copper and manganese.[56, 57]

Element	Emission line	Energy [eV]	Intensity	Γ [eV]	τ_c [fs]
Copper	K_{α_1}	8047	0.577	2.35	0.49[2]
	K_{α_2}	8027	0.294	3.41	
	$K_{\beta_{1,3}}$	8905	0.084	5.92	0.22
Manganese	K_{α_1}	5899	0.581	2.47	0.50
	K_{α_2}	5888	0.293	2.92	
	$K_{\beta_{1,3}}$	6490	0.124	2.97	0.44

[2]Note that Inoue *et al.* [39] and Trost *et al.* [40] use a different reference (Krause & Oliver [58]) for the emission line widths which also leads to a different coherence time of $\tau_c \approx 0.62$ fs

2.3 Single Particle Imaging

Single Particle Imaging (SPI) is a lensless imaging technique that allows for the reconstruction of the three-dimensional electron density of single particles from their scattered X-ray intensities. SPI is based on the principle of CDI (see section 2.2.1), but instead of measuring the diffracted intensities of an ensemble average such as in *powder diffraction* or *Small Angle X-ray Scattering* (SAXS), the particles are directed to the X-ray beam one at a time. The diffraction patterns can then be analyzed for each particle individually. For each diffraction pattern there are three uncertainties — the statistical shot noise, the incident fluence and the orientation of the particle. The statistical shot noise is due to the finite number of photons detected in each diffraction pattern. The incident fluence on the particle varies a lot due to the particle's random position with respect to the X-ray focus [26, 27], and the orientation uncertainty is due to the random orientation of the particle in the beam.
Reconstruction algorithms for SPI, like the *Expand-Maximize-Compress* (EMC) algorithm [25, 59] solve these uncertainties in a self-consistent manner.

2.3.1 EMC algorithm

The EMC algorithm is widely used in SPI experiments [18, 60]. It consists of three iterative steps: expand, maximize, and compress. Each iteration aims to refine the model to better match the measured detector data. In the expand step, the model is transformed from model space to detector space based on a set of sampled hidden parameters. Typically, the model consists of a grid of 3D intensities, while the hidden parameters represent orientations and incident fluence on the particles. This step involves interpolating the 3D intensities along the Ewald sphere surface (see section 2.3.3), rotated according to the given orientation and scaled by the relative fluence, followed by applying standard polarization and solid angle corrections (see section 2.3.4) to generate the predicted detector intensities. Next, the maximize step updates these detector views using the expectation maximization procedure, incorporating a noise model. Additionally, the maximum likelihood fluence factors are usually determined. This results in a set of updated views with a higher likelihood, though they may not necessarily align with a single 3D intensity. Finally, the compress step ensures consistency across the updated views. A common approach is to reinterpolate the detector views back into the

3D model after reversing the detector corrections. [25]
Once the 3D intensity converges, standard iterative phase retrieval algorithms are applied to obtain the electron density [18, 54, 55].
In this work, we will use only the two-dimensional implementation of the EMC algorithm. In this case, the models are two-dimensional representations, and the relative particle orientations are confined to a single plane.
Consider the Poisson noise model for a set of two-dimensional intensities W. Let the number of photons at pixel number t in a two-dimensional data frame d be K_{dt}, and for a given orientation r the predicted mean intensity at the same pixel be W_{rt}. Since Poisson process at each pixel is independent, the probability of the pattern being generated by a 2D model W_r is

$$R_{dr} = \prod_{t=1} \frac{(W_{rt}\phi_d)^{K_{dt}}}{K_{dt}!} e^{-W_{rt}\phi_d}, \tag{2.27}$$

where ϕ_d is a scaling factor which is proportional to the fluence of the X-ray beam on the particle. The scaling factor ϕ_d is assumed to be the same for all pixels in a given frame d. These fluence factors are later used to estimate the absolute incident fluence on the particles (see 2.3.2). The particle orientation is the same for each pixel. Hence, the probability of frame d having orientation r can be obtained by averaging over all orientations:

$$P_{dr} = \frac{R_{dr}}{\sum_r R_{dr}}. \tag{2.28}$$

The model log-likelihood is then given by the expectation of the total log-likelihood of the data being generated by a new model W'_{rt} and ϕ'.

$$Q(W\prime, \phi\prime, W, \phi) = \sum_d \sum_r \sum_t P_{dr} \left[K_{dt} \log(W'_{rt}\phi'_d) - W'_{rt}\phi'_d\right], \tag{2.29}$$

neglecting model-independent constants.

Since there is no analytical solution to simultaneously update both W'_{rt} and ϕ'_d, the update rules are derived separately, while keeping the other parameter fixed. In order to maximize the log-likelihood, we can take the partial derivative of the log-likelihood with respect to W'_{rt} and ϕ' and set it to zero:

$$W_{rt} \rightarrow W'_{rt} = \frac{\sum_d P_{dr} K_{dt}}{\sum_d P_{dr} \phi_d}. \tag{2.30}$$

$$\phi_d \rightarrow \phi'_d = \frac{\sum_t K_{dt}}{\sum_{r,t} P_{dr} W_{rt}}. \tag{2.31}$$

For the data classification of XFEL diffraction patterns we use the *Dragonfly* package [25], which implements the EMC algorithm and provides a *Python* interface for the analysis of single particle diffraction data.

2.3.2 Absolute fluence estimation

The elastically scattered intensity I_{el} scales linearly with the incident fluence Φ on the particles [27]:

$$I_{\text{el}}(\mathbf{q}) = \Phi \cdot \left(2\pi \cdot d^3 \cdot \Delta n \cdot \frac{1}{\lambda^2}\right)^2 \cdot \left|\mathcal{F}(\mathbf{q})\right|^2 \cdot \Omega(\mathbf{q}), \tag{2.32}$$

where d is the particle diameter, Δn the refractive index of the underlying sample, λ the incident photon wavelength, and $\Omega(\mathbf{q})$ the integrated solid angle of the detector pixels where the elastic signal was measured (see section 2.3.4). $\left|\mathcal{F}(\mathbf{q})\right|^2$ in equation 2.32 are the normalized Fourier amplitudes for the respective pixel at a scattering vector $\mathbf{q}$. For example, for cubic samples, $F(\boldsymbol{q})$ is given by:

$$\mathcal{F}(\mathbf{q}) = \frac{\sin(\pi \mathbf{q} d)}{\pi \mathbf{q} d}. \tag{2.33}$$

From the *Dragonfly* 2D class averages the average sample size and the incident fluence can be estimated from reference diffraction patterns using equation 2.32. During the classification process, *Dragonfly* calculates the relative intensity scaling between different diffraction patterns in order to calculate a weighted class average (see section 2.3.1). Using the calculated fluence for the reference diffraction patterns, the fluence for all diffraction patterns can easily be estimated by applying the relative scaling factors.

2.3.3 Ewald Sphere

As mentioned in section 2.2.1, the scattered intensities can only be measured on the surface of the Ewald sphere. The Ewald sphere is a geometric construction that relates the scattering vector $\boldsymbol{q}$ to the incident and scattered wave vectors $\boldsymbol{k}_0$ and $\boldsymbol{k}_f$, respectively.

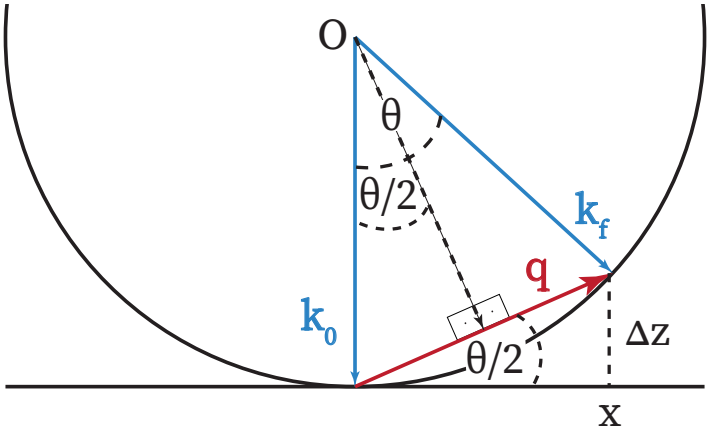


Figure 2.2: Ewald sphere construction. The incident and the scattered wave vectors $\boldsymbol{k}_0$ and $\boldsymbol{k}_f$ are shown in blue and the momentum transfer vector $\boldsymbol{q}$ is shown in red. The radius of the Ewald sphere is $1/\lambda$, where λ is the wavelength of the incident X-ray beam.

Suppose the incident X-ray beam with a photon wavelength of λ travels along the positive z-axis. In the following, we will use the crystallographer's convention for the wave vectors:

$$\boldsymbol{k}_0 = \{0, 0, 1/\lambda\}\,. \tag{2.34}$$

For a scattered wave vector $\boldsymbol{k}_f$ measured at pixel $\{x, y, z_D\}$ on the detector, the elastically scattered photon has a reciprocal wave vector of

$$\boldsymbol{k}_f = \frac{1}{\lambda}\frac{\{x, y, z_D\}}{\sqrt{x^2 + y^2 + z_D^2}}. \tag{2.35}$$

Hence, the pixel measures the kinematic diffraction intensities at the spatial frequency $\boldsymbol{k_f} - \boldsymbol{k_0}$ (from Eq. 2.21):

$$\boldsymbol{k_f} - \boldsymbol{k}_0 = \frac{1}{\lambda}\left[\frac{\{x, y, z_D\}}{\sqrt{x^2 + y^2 + z_D^2}} - \{0, 0, 1\}\right]. \tag{2.36}$$

Equation 2.36 describes the mapping of the pixel coordinates of the planar detector onto the curved surface of the Ewald sphere, which intersects with the scatterer's zero frequency (origin of the reciprocal space), or, equivalently, the unscattered wave vector $\boldsymbol{k}_0$.

2.3.4 Solid angle and polarization correction

To obtain the correct Fourier amplitudes in a diffraction experiment, the measured intensities must be corrected for experiment-specifc geometric factors, such as the solid angle of the detector pixels and the polarization of the incident beam.
The integrated solid angle Ω of a detector with pixel size s_p and positioned at a distance D from the interaction region can be approximated as:

$$\Omega \approx \sum_{\theta} \cos^3(\theta) \cdot \frac{s_p^2}{D^2}, \tag{2.37}$$

where θ is the angle between the incident beam and the detector pixel s_p which is much smaller than the detector distance D. Here, two cosine factors account for the reduced solid angle of the planar detector pixels that have to be mapped onto the Ewald sphere. The third cosine factor accounts for the fact that the pixels are not perpendicular to the scattered wave vector, $\mathbf{k_f}$.
The polarization correction compensates for the reduced scattering cross-section in the plane of the incident beam's polarization. Consider an incident X-ray beam which is polarized along $\hat{x} = \{1, 0, 0\}$. Then, the scattered intensity at a pixel is reduced by the polarization correction factor P [25]:

$$P = 1 - |\hat{\boldsymbol{x}} \cdot \hat{\boldsymbol{v}}(x, y, z_D)|^2 = \cos^2(\theta), \tag{2.38}$$

where $\hat{v}(x, y, z_D)$ is the unit vector of the scattered wave vector $\boldsymbol{k}_f$ at the pixel $\{x, y, z_D\}$ on the detector.

2.4 Coherence

The coherence of light is a measure of the correlation between the electric fields at different points in space and time. To quantify coherence, Michelson [61] defined the visibility ν as the ratio of the difference between the maximum and minimum intensity of interference fringes to the sum of the maximum and minimum intensity:

$$\nu = \frac{I_{\max} - I_{\min}}{I_{\max} + I_{\min}}. \tag{2.39}$$

The coherence of light can be classified into two types: spatial coherence and temporal coherence. Spatial coherence is a measure of the correlation between the electric fields at different points in space, while temporal coherence is a measure of the correlation between the electric fields at different points in time.

2.4.1 Temporal coherence

The temporal coherence of a wave $\psi(t) = Ae^{i\omega t}$ with frequency ω and amplitude A can be quantified by the complex degree of coherence $g^{(1)}(\tau)$, which is defined as the normalized cross-correlation function of the electric field at two different times t and $t + \tau$ [62]:

$$g^{(1)}(\tau) = \frac{\langle \psi(t)\psi^*(t+\tau)\rangle_t}{\langle \psi(t)\psi^*(t)\rangle_t}, \tag{2.40}$$

where $\langle\cdot\rangle_t$ denotes the temporal average. Zernike [63] showed that the modulus of the complex degree of coherence $|g^{(1)}(\tau)| = \nu$ is equivalent to the definition of Michelson [61]. Furthermore, we can define the coherence time τ_c as the time during which the relative phases of the waves remain constant [62]:

$$\tau_c = \int_{-\infty}^{\infty} |g^{(1)}(\tau)|^2 d\tau. \tag{2.41}$$

The complex degree of coherence is also called the first-order coherence function. There exist also higher orders of coherence functions, most importantly the

second-order coherence function $g^{(2)}(\tau)$, which is commonly used for coincidence measurements:

$$g^{(2)}(\tau) = \frac{\langle \psi(t)\psi(t+\tau)\psi^*(t)\psi^*(t+\tau)\rangle_t}{\langle \psi(t)\psi^*(t)\rangle_t^2} = \frac{\langle I(t)I(t+\tau)\rangle_t}{\langle I(t)\rangle_t^2}. \tag{2.42}$$

If the waves are fully independent, we can apply the so-called Siegert relation [64]:

$$g^{(2)}(\tau) = 1 + |g^{(1)}(\tau)|^2. \tag{2.43}$$

The derivation of the Siegert relation is shown for the case of spatial correlations in section 2.5.
In their ground-breaking experiments Hanbury Brown & Twiss [30] observed the so-called photon-bunching effect for chaotic light — on short timescales of the order of the coherence time of the light field, the second-order coherence function yields $|g^{(2)}(0)|^2 > 1$. For single photon emitters however, the second-order coherence function yields anti-bunching $|g^{(2)}(0)|^2 < 1$, as it is not possible to detect a photon on two separated detectors at the same time [65–67]. Both effects, the photon-bunching and the anti-bunching are commonly referred to as Hanbury Brown and Twiss (HBT) effects.

2.4.2 Spatial coherence

Complementary to the temporal coherence, the spatial coherence refers to the phase relations at two different points $\boldsymbol{r_1}$ and $\boldsymbol{r_2}$ in space:

$$g^{(1)}(\boldsymbol{r_1}, \boldsymbol{r_2}) = \frac{\langle \psi(t, \boldsymbol{r_1})\psi^*(t, \boldsymbol{r_2})\rangle_t}{\sqrt{\langle \psi(t, \boldsymbol{r_1})\psi^*(t, \boldsymbol{r_1})\rangle_t \langle \psi(t, \boldsymbol{r_2})\psi^*(t, \boldsymbol{r_2})\rangle_t}}. \tag{2.44}$$

Using the van Cittert-Zernike theorem [63], which states that the spatial coherence of an incoherent light source increases with distance to the source, the first-order spatial coherence function $g^{(1)}(\boldsymbol{r_1}, \boldsymbol{r_2})$ in the far-field can be related to the intensity distribution $I(x, y)$ of the light field via the Fourier transform $\mathcal{F}$:

$$g^{(1)}(\boldsymbol{r_1}, \boldsymbol{r_2}) = \frac{\mathcal{F}(I(x, y))}{\mathcal{F}(I(0, 0))}. \tag{2.45}$$

The coherence area A_c, where the light is considered spatially coherent, is then defined as:

$$A_c = \int\int |g^{(1)}(\Delta x, \Delta y)|^2 d\Delta x d\Delta y \approx \frac{(\lambda z)^2}{A_s}, \tag{2.46}$$

where λ is the wavelength of the light, z is the distance to the source, and A_s is the area of the source.

2.5 Incoherent Diffractive Imaging

Incoherent Diffractive Imaging (IDI) is a lensless imaging technique that leverages transient spatio-temporal coherence properties of a light source otherwise regarded as incoherent to reconstruct the underlying emitter distribution. In the far-field approximation, a classical wave field emitted from N independent point-like emitters can be described as a superposition of plane waves:

$$\psi(\boldsymbol{k}) = \sum_{j=1}^{N} e^{2\pi i \boldsymbol{k}\cdot\boldsymbol{r}_j + \phi_j}, \tag{2.47}$$

where $\boldsymbol{k}$ is the wave vector, ϕ_j is the phase of the j-th emitter with $\phi_j \in [0, 2\pi)$. Here, the term for the radial decay $1/|\boldsymbol{r}_j|$ is omitted for simplicity. Incoherent light with random and uncorrelated phases ϕ will, on average, result in a uniform intensity distribution in the far-field [33]:

$$\begin{aligned} \langle I(\boldsymbol{k})\rangle &= \langle \psi(\boldsymbol{k})\psi^*(\boldsymbol{k})\rangle \\ &= \sum_{j=1}^{N}\sum_{l=1}^{N} e^{2\pi i \boldsymbol{k}\cdot(\boldsymbol{r}_j - \boldsymbol{r}_l)} \langle e^{i(\phi_j - \phi_l)}\rangle_\phi = N, \end{aligned} \tag{2.48}$$

since the phase term $\left\langle e^{i(\phi_j - \phi_l)}\right\rangle = \delta_{j,l}$ is only non-zero for $j = l$. Equivalent to equation 2.42, let us now consider the spatial second-order correlation function $g^{(2)}(\boldsymbol{q})$, where $\boldsymbol{q} = \boldsymbol{k_i} - \boldsymbol{k_j}$ is the wave vector difference between two points $\boldsymbol{k}_i$ and $\boldsymbol{k}_j$ in the far-field.

$$g^{(2)}(\boldsymbol{q}) = \frac{\langle I(\boldsymbol{k})I(\boldsymbol{k}+\boldsymbol{q})\rangle_{\boldsymbol{k}_{i,j}}}{\langle I(\boldsymbol{k})\rangle^2_{\boldsymbol{k}_{i,j}}} \tag{2.49}$$

Let us first analyze the numerator of equation 2.49:

$$\begin{aligned}\langle I(\boldsymbol{k}_1)\cdot I(\boldsymbol{k}_2)\rangle &= \langle \psi(\boldsymbol{k}_1)\psi^*(\boldsymbol{k}_1)\cdot\psi(\boldsymbol{k}_2)\psi^*(\boldsymbol{k}_2)\rangle \\ &= \sum_{j=1}^{N}\sum_{j'=1}^{N}\sum_{l=1}^{N}\sum_{l'=1}^{N} e^{2\pi i\boldsymbol{k}_1\cdot(\boldsymbol{r}_j-\boldsymbol{r}_{j'})}e^{2\pi i\boldsymbol{k}_2\cdot(\boldsymbol{r}_l-\boldsymbol{r}_{l'})}\langle e^{i(\phi_j-\phi_{j'}+\phi_l-\phi_{l'})}\rangle_\phi\end{aligned} \tag{2.50}$$

The phase term $\langle e^{i(\phi_j-\phi_{j'}+\phi_l-\phi_{l'})}\rangle$ is non-zero in two different cases:

Case 1: $j = j'$ and $l = l'$:

$$\sum_{j=1}^{N}\sum_{l=1}^{N} e^{2\pi i\boldsymbol{k}_1\cdot(\boldsymbol{r}_j-\boldsymbol{r}_j)}e^{2\pi i\boldsymbol{k}_2\cdot(\boldsymbol{r}_l-\boldsymbol{r}_l)} = N^2, \tag{2.51}$$

Case 2: $j = l'$ and $l = j'$:

$$\sum_{j=1}^{N}\sum_{l=1}^{N} e^{2\pi i\boldsymbol{k}_1\cdot(\boldsymbol{r}_j-\boldsymbol{r}_l)}e^{2\pi i\boldsymbol{k}_2\cdot(\boldsymbol{r}_l-\boldsymbol{r}_j)} = \sum_{j=1}^{N}\sum_{l=1}^{N} e^{2\pi i(\boldsymbol{k}_1-\boldsymbol{k}_2)\cdot(\boldsymbol{r}_j-\boldsymbol{r}_l)} = \left|\sum_{j=1}^{N} e^{2\pi i\boldsymbol{q}\cdot\boldsymbol{r}_j}\right|^2 \tag{2.52}$$

Hence, in cases where the *van Cittert - Zernike theorem* applies and when the light is detected on timescales similar to its coherence time τ_c, the spatial second-order coherence function $g^{(2)}(\boldsymbol{k}, \boldsymbol{k}+\boldsymbol{q})$ holds spatial information about the underlying emitter distribution:

$$\begin{aligned} g^{(2)}(\boldsymbol{q}) &= \frac{\langle I(\boldsymbol{k})I(\boldsymbol{k}+\boldsymbol{q})\rangle_{\boldsymbol{k}_{i,j}}}{\langle I(\boldsymbol{k})\rangle^2_{\boldsymbol{k}_{i,j}}} \\ &= 1+\nu\left|g^{(1)}(\boldsymbol{q})\right|^2 \\ &= 1+\nu\frac{|\mathcal{F}(\boldsymbol{q})|^2}{|\mathcal{F}(0)|^2}. \end{aligned} \tag{2.53}$$

Here, the Siegert relation was modified by the additional factor ν to account for a reduction of the visible interference fringes of partially coherent light [68]. The sources of partial coherence can be attributed to many different effects, such as polarizations, measurement times longer than the coherence time τ_c, the finite size of the source and the finite bandwidth of the light. Ultimately, these effects can be described by the number of incoherent modes M in the light-field, which relates to the visibility as $\nu = 1/M$ [36].

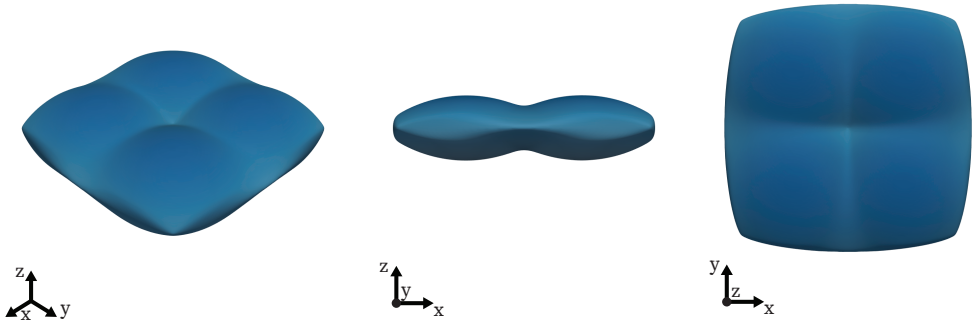


Figure 2.3: Schematic of the surface of the three-dimensional $g^{(2)}(\boldsymbol{q})$ function.

Figure 2.3 schematically shows the 3D surface in the second-order correlation space. Since the correlation function is similar to a convolution, this 3D surface represents a convolution of the spherical cap of the 3D Ewald sphere that is covered by the detector (see Fig. 2.2). Consequently, the correlation space also holds in-depth (k_z) information about the underlying emitter, and it also spans twice as long along k_x and k_y, theoretically allowing for higher spatial reconstruction resolutions. It shall be noted that a full quantum mechanical treatment of the second-order coherence function $g^{(2)}$ for single photon emitters yields a slightly different expression, which, for a high number of emitters N converges to the classical expression [33]:

$$g^{(2)}_{\mathrm{SPE}}(\boldsymbol{q}) = 1 - \frac{2}{N} + \left|g^{(1)}(\boldsymbol{q})\right|^2 . \tag{2.54}$$

In the scope of this thesis, the focus is on measuring the fluorescence of nanoparticles with millions of emitters. Therefore, the classical description of the second-order correlation function $g^{(2)}$ is considered sufficient and will be used in the following.

2.6 Speckles and photon statistics

The interference of many light waves with random phases $\phi \in [0, 2\pi)$ results in transient speckle patterns in the far-field [68, 69]. The intensity distribution of these speckles can be described by the negative exponential distribution:

$$P_{\mathrm{Exp}}(I|\mu) = e^{-\frac{I}{\mu}}, \tag{2.55}$$

where μ is the expectation value of the intensity I. Due to the quantized nature of photons n, the intensity distribution becomes a Bose-Einstein distribution [69]:

$$P_{\mathrm{BE}}(n|\mu) = \frac{1}{1+\mu}\left(\frac{\mu}{1+\mu}\right)^{n}. \tag{2.56}$$

With partial coherence, this intensity distribution transforms into a negative binomial distribution [69]:

$$P_{\mathrm{NB}}(n|\mu,\beta) = \frac{(\beta\mu)^{n}(1+\beta\mu)^{-(1+\beta n)/\beta}\,\Gamma(n+1/\beta)}{n!\,\Gamma(1/\beta)}, \tag{2.57}$$

where μ is the average photon count per pixel and β is the so-called speckle contrast. The parameterization of $P_{\mathrm{NB}}(n|\mu,\beta)$ by β is following the same reasoning as for the visibility ν in the previous section 2.5. Hence, the speckle contrast β is directly related to the number of incoherent modes in the light field: $\beta = 1/M$. For coherent light β equals 1, whereas for fully incoherent light, β approaches 0. The speckle contrast for partially coherent fluorescence can be estimated for single exposures as follows [68]:

$$\beta = \frac{\mathrm{Var}(I) - \mu}{\mu^{2}}, \tag{2.58}$$

where $\mathrm{Var}(I)$ is the variance of the photon counts on the detector. Following the standard methodology in the literature [39, 40], which assumes incident Gaussian pulses, the effective pulse duration T on the particles can be estimated from the speckle contrast as:

$$T \approx \frac{5}{27}\frac{\tau_c}{\beta}. \tag{2.59}$$

In measurements with perfectly stable conditions, the speckle contrast β and the visibility ν can theoretically be used interchangeably. However, our results in chapter 3 show large discrepancies between these two values. The reasons for this will be discussed in the respective chapter.

2.7 Simulations

In order to determine good experimental conditions such as detector distance for a given sample size, and to support the analysis of the experimental data, we implemented a simulation framework for IDI in *Python*. The simulation framework is based on the assumption that the emitters are point-like and uniformly distributed within the particle. The emitters are assumed to be independent and uncorrelated.
Since the initial phase of a fluorescence photon is random, we cannot directly employ *fast Fourier transform* (FFT)-based algorithms to calculate the far-field intensity on the detector. Instead, we need to simulate the intensity distribution on the detector by summing up the contributions of all individual emitters in a given temporal mode. The pseudo-code for this simulation is shown in Algorithm 1. In the case of spectrally-resolved IDI (see chapter 4), the simulation was modified in the following way: The wavefunction $\psi_m(k)$ for each temporal mode m was calculated only for one detector pixel column and subsequently convolved with the Lorentzian spectral profile $\tilde{S}(E)$ of the emission lines.

$$I(k, E) = \sum_{m=1}^{M} \tilde{S}(E)|\psi_m(k)|^2, \tag{2.60}$$

where the sum is over each temporal mode.

Algorithm 1: Simulation of the far-field fluorescence intensity.

Data: N: Number of emitters
M: Number of temporal modes
k: Wave vector
ϕ: Random initial phase in $[0, 2\pi)$
Result: Simulated intensity with Poisson noise
for $m \leftarrow 1$ ***to*** M **do**
  Initialize $\psi[m] \leftarrow 0$; `// Initialize wavefunction for mode` m
  for $j \leftarrow 1$ ***to*** N **do**
    $\phi_j \leftarrow$ random value in $[0, 2\pi)$; `// Assign random phase to emitter` j
    $\psi[m] \leftarrow \psi[m] + \exp(i \cdot (2\pi \cdot k \cdot r[j] + \phi_j))$; `// Sum plane waves with random phases`
  end
  $I[m] \leftarrow |\psi[m]|^2$; `// Calculate intensity for mode` m
end
$I_{\text{total}} \leftarrow \sum_{m=1}^{M} I[m]$; `// Combine intensities across all modes`
$I_{\text{poisson}} \leftarrow \text{PoissonSample}(I_{\text{total}})$; `// Poisson sample intensity`
$I_{\text{noisy}} \leftarrow I_{\text{poisson}} + \text{PoissonNoise}()$; `// Add Poisson noise`

Chapter 3

The Nature of Hard X-Ray Fluorescence from Nanoparticles under Extreme Conditions

This chapter demonstrates the first implementation of IDI of single particles. Furthermore, our study of the degree of second-order spatial coherence shows a fluence dependence that remains undetectable via speckle contrast, with profound implications IDI. Moreover, the SPI approach allows us to investigate into the fundamental light-matter interactions and coherence properties of core-shell hard X-ray fluorescence over a broad range of incident fluences.

Authors Contributions:
Tamme Wollweber: Conceptualization (supporting); Beamtime (equal); Investigation(lead); Software (lead); Writing – original draft (equal).
Kartik Ayyer: Conceptualization (lead); Funding acquisition (lead); Beamtime (equal); Investigation(supporting); Methodology (lead); Supervision (lead); Writing – original draft (equal)
Sebastian Cardoch: Theoretical modelling (lead)
Sarodi Jonak Dutta: Sample preparation (lead)

3.1 Single Particle Imaging and Fluorescence Experiment

Figure 3.1 schematically illustrates the experimental setup which was performed at the *Single particles, biomolecules and clusters/serial femtosecond crystallogra-*

phy (SPB/SFX) instrument [70] at the European X-ray free electron laser (EuXFEL) [16]. Copper oxide nanocubes with an average size of 88 nm (for sample preparation details see Appendix A.1) were aerosolized using an electrospray sample injector [71] and directed into the focus of the XFEL beam, with a nominal focal spot size of $250 \times 250\,\mathrm{nm}^2$.

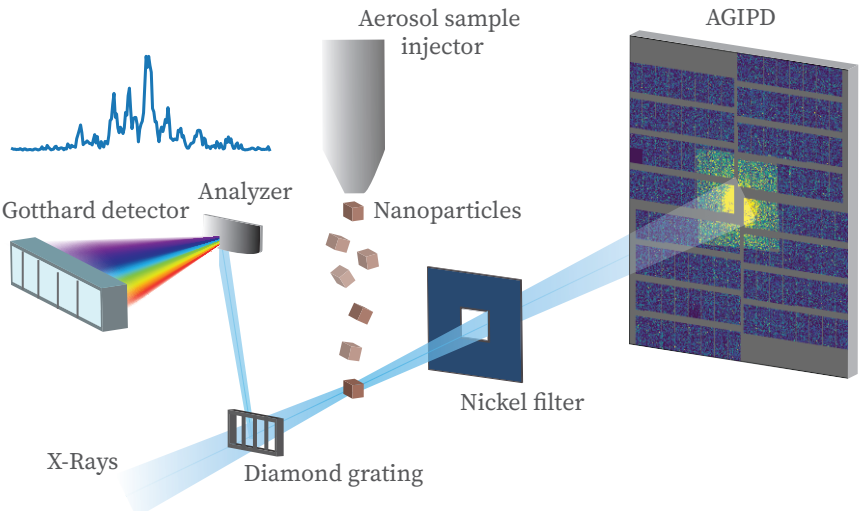


Figure 3.1: Schematic of the experimental setup. The copper nanoparticles are aerosolized and injected into the interaction region by an electrospray [71]. The nickel foil filters the coherently scattered photons as well as the K_β emission at high scattering angles. The coherent diffraction at low-$\mathbf{k}$ can be used for orientation determination and classification. The coherence properties of the K_α fluorescence can then be studied for the filtered area on the detector. Simultaneously, the spectra of the incident X-ray pulses are recorded by the *High-resolution hard X-ray single-shot* (HIREX) spectrometer [72].

A 20 µm thick nickel foil (K-edge at 8332 eV [57]) was placed between the interaction region and the *Adaptive gain integrating pixel detector* (AGIPD) [73] positioned 715 mm away to preferentially absorb the elastic scattering and the K_β fluorescence while letting the K_α photons through. The nickel foil had a 10 mm by 10 mm square aperture in the central region, which allowed the coherent elastic scattering to pass through, enabling orientation determination and structure classification using single particle imaging methods [18, 59]. In total, 391 035 frames were detected with statistically significant signal over background. Three different photon energies were used, scanning across the tabulated absorption K-edge at 8978.9 eV [57]: 8910 eV, 9015 eV, and 9170 eV. The measurements were conducted for two different XFEL operation modes, providing short and long pulses

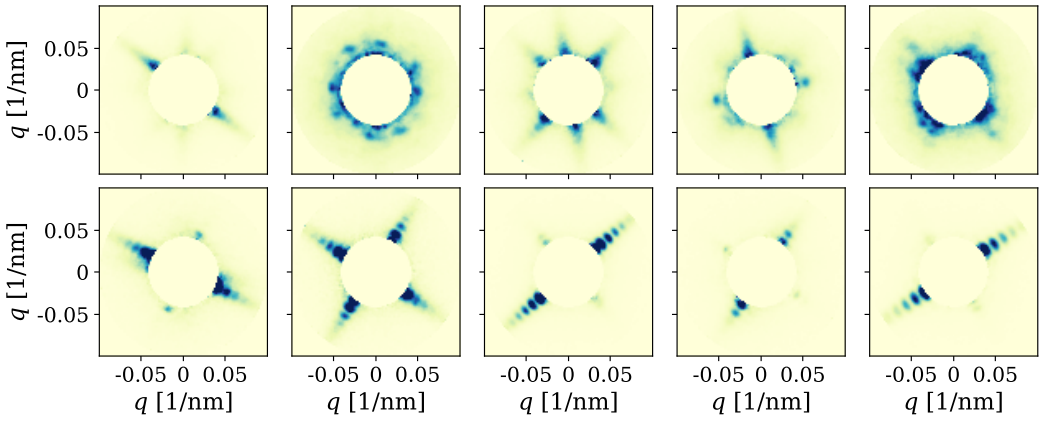


Figure 3.2: Exemplary *Dragonfly* 2D class averages for short pulses. The top row displays 5 class averages that were rejected after the first round of classification. The class averages in the bottom row correspond to the diffraction patterns contributing to the $g^{(2)}$-signal shown in Figure 3.7.

with nominal pulse durations and pulse energies of 2.5 fs, 200 µJ and 25 fs, 2 mJ, respectively. We emphasize that this single particle imaging setup inherently enables the examination of key material characteristics, such as fluorescence cross-section and degree of coherence of the K_α fluorescence, across a broad range of incident fluences, as the position of the individual particles relative to the X-ray focus varies from pulse to pulse. We performed 2D classification using the *Dragonfly* software [25] in two rounds, filtering out clusters and contaminants at the first stage (see Fig. 3.2). This resulted in 143 994 single particle diffraction patterns across the different conditions. The relative fluence factors from the classification were then converted to an absolute scale using tabulated coherent scattering cross-sections (see section 2.3.2). Figure 3.2 illustrates representative class averages: the top row includes those that were rejected after the initial classification round, while the bottom row shows the class averages of patterns that were selected for calculating the average $g^{(2)}$-signal presented in Figure 3.7.

3.1.1 Incident spectrum and pulse duration

The energy distribution of each pulse was recorded using the HIREX spectrometer (Fig. 3.3A) [72]. The energy spectra of *self-amplified spontaneous emission* (SASE) pulses exhibit shot-to-shot fluctuations, affecting the center frequency, the local spike width, and the relative intensity profile within an average Gaussian envelope. To estimate the average spike width, which ultimately determines the temporal

duration of the XFEL pulse [74], we calculate the second-order correlation function (Fig. 3.3B) for all spectra according to:

$$g^{(2)}(\Delta E) = \frac{\langle I(E) \cdot I(E + \Delta E) \rangle}{\langle I(E) \rangle^2}, \tag{3.1}$$

The correlation function shows both signatures, the average spike width and the overall envelope. A Gaussian fit to the central feature in Figure 3.3B for $g^{(2)}(\Delta E)$ yielded an average spike width of $\Delta E = 0.65\,\text{eV}$. Now, the pulse duration can be estimated by applying the time-bandwidth product for Gaussian pulses ($\Delta T \cdot \Delta f \approx 0.441$), leading to an estimate of the pulse duration of $\Delta T \approx 2.8\,\text{fs}$.

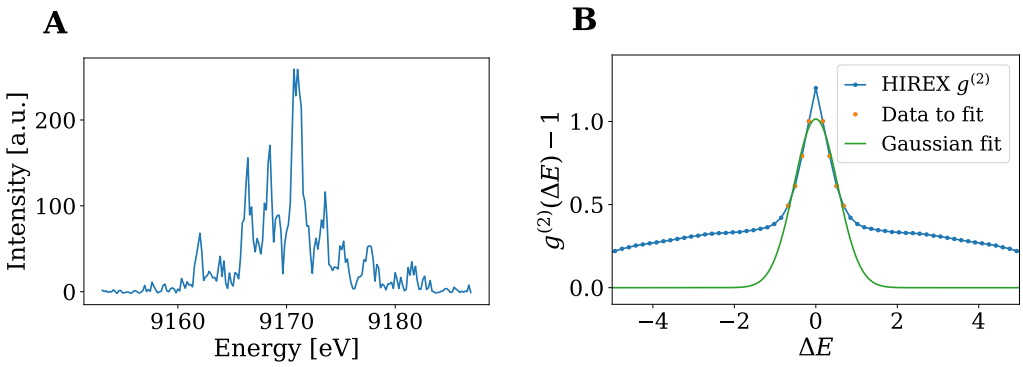


Figure 3.3: Estimation of the pulse duration. (**A**) Exemplary HIREX spectrum. (**B**) $g^{(2)}(\Delta E)$ for all spectra for a photon energy of 9170 eV. The full width at half maximum of the Gaussian fit can be used to calculate the incident pulse duration.

We note that even though the temporal structure of a SASE XFEL pulse is highly non-Gaussian, assuming the FEL spikes themselves are transform-limited, their width is a measure of the pulse duration. One can additionally estimate the number of spikes, however no information can be extracted about the relative temporal ordering and arrival time of each spike. The overall average envelope of the pulse spectrum is consistent with 250 as spikes as expected.

3.2 Degree of second-order coherence of K_α fluorescence

The integrated far-field intensity distribution of the K_α fluorescence does not yield any structural information due to the absence of first-order coherence (see sec. 2.5).

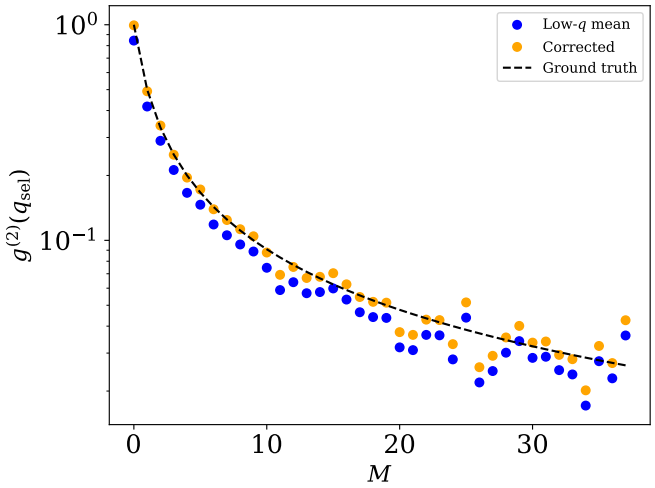


Figure 3.4: Mean $g^{(2)}$-value for the inner four non-masked voxels as a function of incoherent modes M. The comparison with the ground truth yields a correction factor of 1.18 to retrieve the visibility ν at $q = 0$.

However, the degree of second-order coherence $g^{(2)}(\mathbf{q})$ of the fluorescence is related to the Fourier transform of the atomic distribution by the well-known Siegert relation (see Eq. 2.53). The visibility ν determines the contrast of the correlation function at $\mathbf{q} = 0$, which depends primarily on the number of temporal modes M and their photon occupancy during a single exposure [36]. Comparable to standard HBT experiments for single photon emitters, where the degree of anti-bunching for $\Delta t = 0$ is retrieved [66, 67], we here apply the same methodology in the spatial domain, i.e. we extrapolate the low-q $g^{(2)}$-signal to $q = 0$, since $g^{(2)}(0)$ is physically not meaningful. Moreover, the $g^{(2)}$-signals exhibit artificially strong correlations for photons detected within the same pixel rows and columns. Therefore, we mask the voxels in the $g^{(2)}$ where $q_x = 0$ or $q_y = 0$. To estimate the visibility at $q = 0$, we now calculate the mean $g^{(2)}$-value for the inner four voxels $q_x, q_y \in \{-1, 1\}$. When applied to the simulations of an 88 nm particle, we retrieve a correction factor of 1.18 from the mean deviation to the expected values ($\nu = 1/M$) (see Fig. 3.4).

The visibility has so far been defined as the difference between the signal at $q = 0$ and the overall offset $\mathcal{O}$ of the $g^{(2)}(\mathbf{q})$ [39, 40]. However, in our case, the incident fluence on the particles and thus the fluorescence intensity on the detector μ varies dramatically from shot to shot. When we assume that the underlying true correlations $\langle I_1 \cdot I_2 \rangle$ are independent of the actual number of photons N, we can define the average $g_n^{(2)}$ of n shots as:

$$
\begin{aligned}
g_{\mathrm{n}}^{(2)}(\mathbf{q}) &= \frac{\langle\langle NI(\mathbf{k}) \cdot NI(\mathbf{k}+\mathbf{q})\rangle\rangle_n}{\langle\langle NI(\mathbf{k})\rangle^2\rangle_n} \\
&= \frac{\langle N^2\rangle_n}{\langle N\rangle_n^2} \cdot \frac{\langle I(\mathbf{k}) \cdot I(\mathbf{k}+\mathbf{q})\rangle}{\langle I(\mathbf{k})\rangle^2} \\
&= \frac{E\left[N^2\right]}{E\left[N\right]^2} \cdot \left(1 + \nu \left|\frac{\mathcal{F}(\mathbf{q})}{\mathcal{F}(0)}\right|^2\right) \\
&= \left(1 + \frac{Var(N)}{\langle N\rangle^2}\right) \cdot g_{\mathrm{single}}^{(2)}(\mathbf{q}) \\
&= \left(1 + \frac{Var(\mu)}{\langle \mu\rangle^2}\right) \cdot g_{\mathrm{single}}^{(2)}(\mathbf{q})
\end{aligned} \tag{3.2}
$$

Consequently, intensity fluctuations lead to an increase of the $g^{(2)}$-signal independent of $\mathbf{q}$, including the signal at $q = 0$ and the overall offset $\mathcal{O}$:

$$
g^{(2)} \propto 1 + \frac{\mathrm{Var}(\mu)}{\langle \mu\rangle^2}, \tag{3.3}
$$

where $\langle\mu\rangle$ denotes the signal level per pixel averaged over many exposures. Hence, the visibility has to be redefined as

$$
\nu = \frac{g^{(2)}(\mathbf{q}=0)}{\mathcal{O}} - 1. \tag{3.4}
$$

We validated our assumption with simulations for $M = 1$ and $M = 20$ and fluctuating fluences (see Fig. 3.5). The conventional definition of the visibility ($\nu = g^{(2)}(0) - \mathcal{O}$) [39, 40] yields physically unreasonable visibilities ($\nu > 1$) for fluctuating incident fluences, whereas our new definition aligns with the expected values.

Moreover, the single particle approach allows us to merge the experimental data into bins of similar signal levels, and examine the behavior of the visibility as a function of average photon counts $\langle\mu\rangle$. Using the relative fluence scaling factors from the *Dragonfly* classification (see sec. 2.3.2), we can directly relate the photon counts to the incident fluence on the particle. Figure 3.6 shows the visibility as a function of the average signal level, $\langle\mu\rangle$, for the experimental as well as

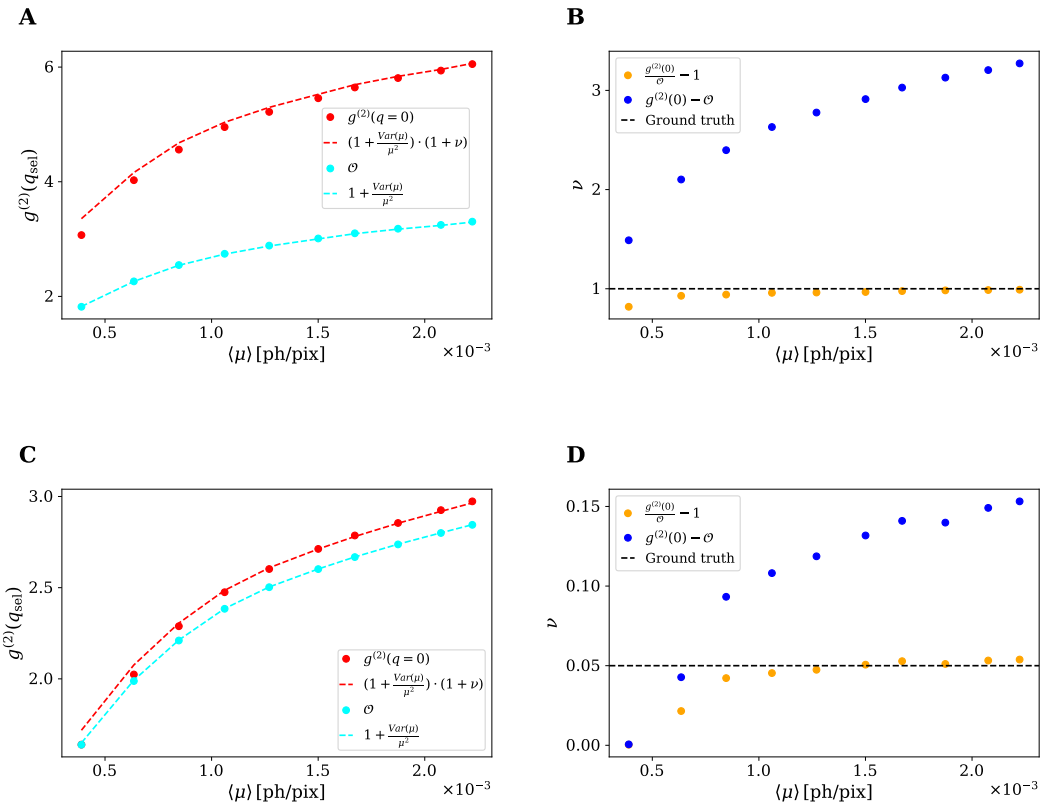


Figure 3.5: Simulations for fluctuating incident fluences for $M = 1$ (top row) and $M = 20$ (bottom row). (**A, C**) Intensity fluctuation dependence of the low-q mean $g^{(2)}$-value and the offset $\mathcal{O}$. (**B, D**) Comparing the two definitions for the visibility ν for fluctuating intensities. The conventional definition (blue) yields physically impossible visibilities ($\nu > 1$), whereas our new definition for ν (orange) converges to the expected values.

simulated data (assuming $M = 20$ incoherent modes) including elastic scattering background. Both the simulations and the experimental data show a low visibility for low μ due to dominating background. For higher signal levels, the visibility increases, as expected, and the experimental data is in good agreement with the simulations. However, there is a large discrepancy in the high signal limit. While the simulations converge to the expected value of $\nu = 0.05$, the experimental data shows a reduction of the visibility to $\nu = 0.007$, corresponding to approximately $M \approx 140$ temporal modes. Interestingly, the visibility behaves qualitatively as the product of two *sigmoid* functions. The left rise can be explained by the gas scattering background from the aerosol injection, which follows Poisson statistics ($\nu = 0$). The right fall-off at higher μ shows the same qualitative but inverse behavior, suggesting the appearance of a new source of background that does not

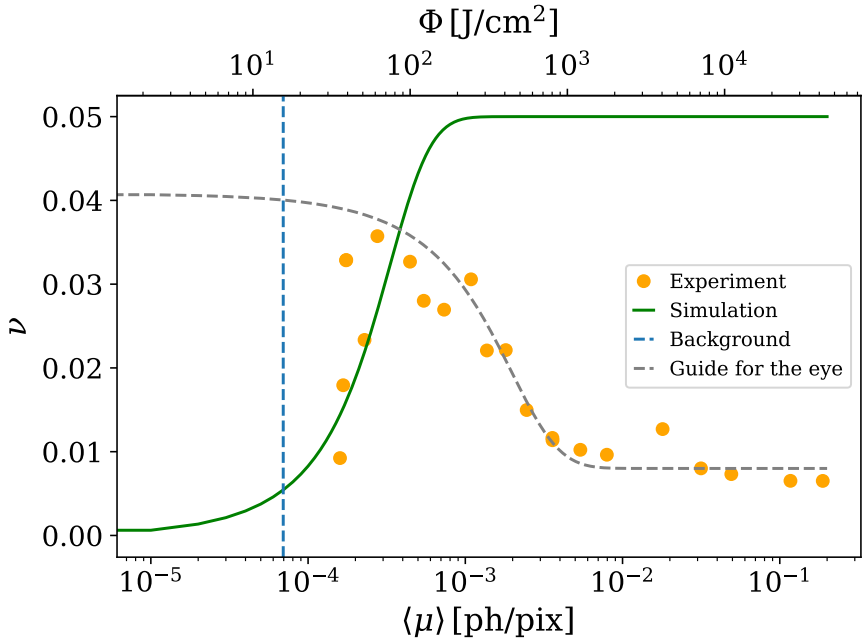


Figure 3.6: Visibility ν as a function of mean photon counts per pixel $\langle\mu\rangle$ for short pulses at 9170 eV. The green line shows the simulated results for 20 modes with the same background level (dashed blue line). The decrease of the visibility for high $\langle\mu\rangle$ shows the same qualitative (but reversed) *sigmoid* behavior (gray dashed line) as the rise for low $\langle\mu\rangle$.

contribute to the visibility. For very high μ the ratio of the spontaneous fluorescence and this new source of background seems to have converged, leading to a lowered, but finite visibility.

We hypothesize that this behavior could be explained by *amplified spontaneous emission* (ASE) [75, 76] that fluctuates from shot to shot. This emission, at the K_α photon energy, will be otherwise indistinguishable on the detector from the spontaneous fluorescence which does contribute to the visibility. In foils much thicker than the focal spot size – on which all prior experiments have been conducted – ASE co-propagates with the XFEL due to the high aspect ratio of the illuminated volume (echoing the nuclear-pumped X-ray laser concept [77]). For particles much smaller than the product of the pulse duration and the speed of light ($88\,\text{nm} \ll \Delta T \cdot c$), the spatial distribution of the ASE is expected to be isotropic, resulting, on average, in a uniform background across the detector.

3.3 IDI of single particles

Despite the reduction of the visibility for high fluences, it is still possible to use the high-signal frames for imaging purposes as they yield a significantly higher SNR than the weaker frames [36]. As described in section 3.1, we classified the diffraction patterns according to the size, shape and orientation of the particles based on the coherently scattered signal. From the *Dragonfly* class averages we selected and merged the $g^{(2)}$-signal of five similar classes (see Fig. 3.7A), corresponding to 1780 frames with an average signal level of $\mu = 4.5 \times 10^{-3}$. The horizontal line profile of the experimental data (Fig. 3.7B) aligns very well with the expected Fourier amplitudes of an 88 nm cube model, maintaining consistency up to a resolution of approximately 20 nm.

Compared to Trost *et al.* [40] this corresponds to 20 times higher resolution, while at the same time requiring only a fraction of diffraction patterns (1780 versus 60 million).

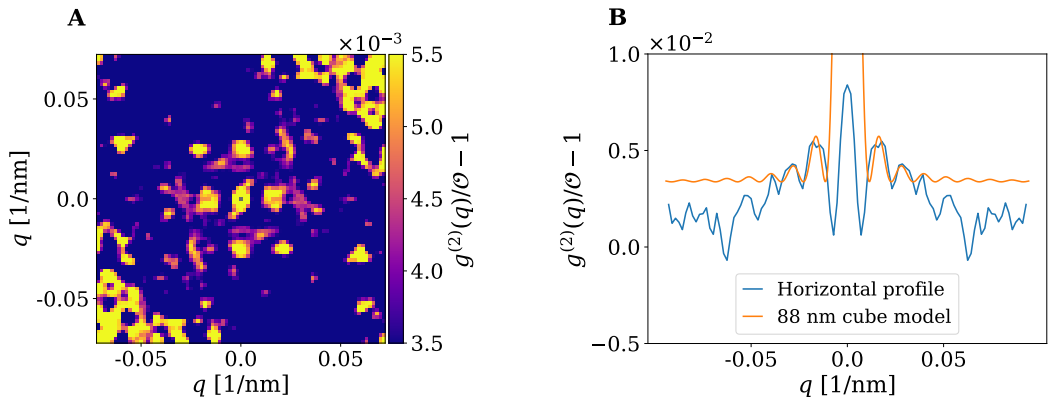


Figure 3.7: (**A**) $g^{(2)}(\mathbf{q})$ from 5 similar *Dragonfly* class averages see (Fig. 3.2). (**B**) Horizontal line profile.

3.4 (Reverse) Saturable Absorption

Let us now turn to the investigation of the light-matter interactions in the vicinity of the K-edge. The advent of X-ray free electron laser (XFEL) sources featuring ultra-short pulse durations and peak brilliance levels several orders of magnitude higher than those of conventional synchrotron sources has given rise to a plethora

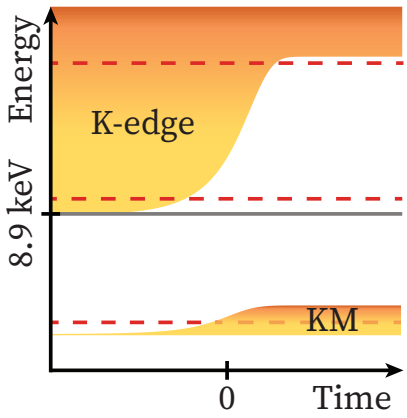


Figure 3.8: Electronic cascade leads to a shift of the absorption edge during the course of an XFEL pulse. The red dashed lines represent the three photon energies used in the scan across the tabulated absorption K-edge at 8978.9 eV (gray line) [57]. The energy 8910 eV lies near the K-to-M shell resonance, 9015 eV just above the K-edge, and 9170 eV well above the edge.

of new opportunities for investigating light-matter interactions under extreme conditions [78–80]. At very high fluences and on ultrafast timescales — on the order of a few femtoseconds or less — multiple photons can interact with a single atom during the course of an XFEL pulse [81]. Under such conditions, the electronic response of matter gives rise to novel phenomena like saturable absorption [82–85], reverse saturable absorption [86] and transient resonances [87, 88]. When matter is exposed to femtosecond hard X-ray pulses above the absorption edge of the inner K-shell, the primary light-matter interaction involves ionizing atoms by exciting electrons from the K-shell into the continuum. The additional energy imparted to the atomic system is then released via mechanisms such as X-ray fluorescence or through the Auger-Meitner effect (see Fig. 2.1). Auger-Meitner decay occurs within the first few femtoseconds after the creation of a K-shell vacancy [81, 89]. Alongside the primary ionization generated directly by the X-ray beam, this effect generates further vacancies in the material, initiating an ionization cascade and the depopulation of the outer valence states of the whole atomic ensemble [14, 90]. This results in an increase of the binding energy of the remaining electrons, or equivalently, a shift of the absorption edge to higher energies [91]. When the absorption edge moves beyond the incident pulse energy, as illustrated in Fig. 3.8B, absorption is suppressed — a phenomenon known as saturable absorption (SA) — and the material effectively becomes transparent.

The reverse behavior can the observed when exposing the material to a photon energy slightly below the edge. Although these photons are insufficiently energetic to ionize electrons from the K-shell, they can ionize electrons from the L, M or higher shells. As a result, the energy difference between the K- and the M-shells increases until this transition becomes resonant with the incident pulse energy. This resonance causes a sudden increase of the absorption cross-section, rendering the material opaque — an effect called reverse saturable absorption (RSA). The subsequent electronic processes are analogous to those of saturable absorption, with vacancies in the K-shell being filled by electrons from the L-shell, resulting in K_α fluorescence.

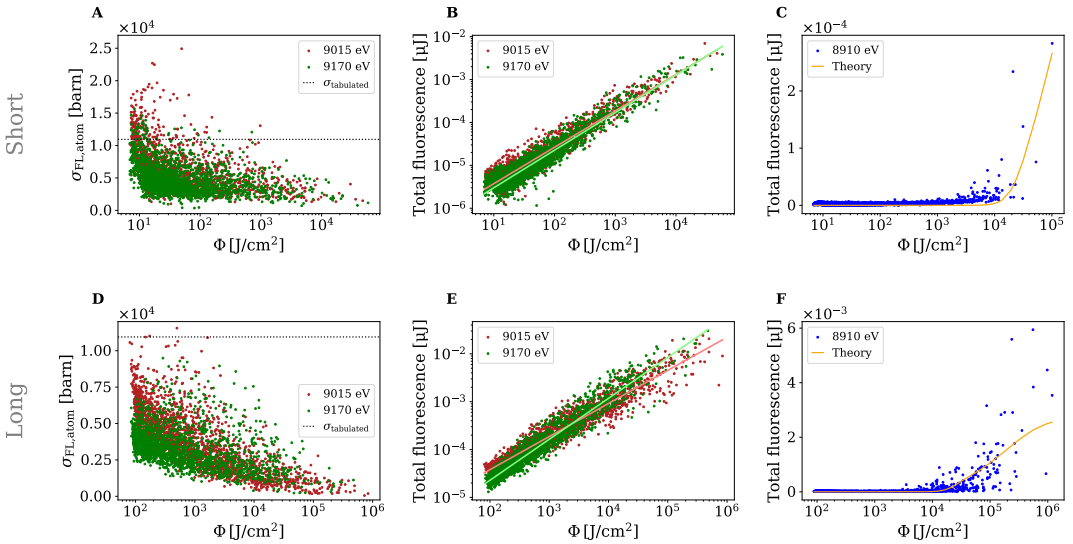


Figure 3.9: (Reverse) Saturable Absorption for short (top row) and long (bottom row) pulses as a function of incident fluence. (**A, D**) Fluorescence cross-sections for incident photon energies of 9015 eV and 9170 eV, exhibiting saturable absorption for higher fluences. (**B, E**) Total fluorescence emission shows a cross-over between the two energies, as indicated by the least-squares fits. (**C, F**) Total fluorescence emission for an excitation energy of 8910 eV and qualitative theoretical prediction, from collisional radiative simulations [92, 93] using relativistic configuration atomic data [94] (see Appendix A.2 for details), revealing reverse saturable absorption.

To calculate the total fluorescence cross-section shown in Figure 3.9, we extrapolated the measured fluorescence intensity (observed in the shadow of the nickel filter) to a full solid angle of 4π steradians, assuming uniform isotropic emission. Furthermore, we corrected for the angular dependent absorption A of the Nickel filter according to:

$$A = 1 - \exp\left(-\frac{\ell}{L\,cos(\theta)}\right), \tag{3.5}$$

where ℓ =20 µm is the thickness of the Nickel foil and L =23.95 µm is the absorption length of Nickel at 90° and for a photon energy of 8040 eV [57]. The fluorescence cross-section σ_{atom} is then given by:

$$\sigma_{\text{atom}} = \frac{E_{4\pi}}{N \cdot \Phi}, \tag{3.6}$$

where $E_{4\pi}$ is the total fluorescence energy emitted in 4π steradians, N is the number of atoms in the particle and Φ is the incident fluence. For long pulses, the absorption cross-section is significantly lower than for short pulses, even at low fluences, and in both cases the cross-section decreases with increasing fluence, indicating saturable absorption. While the absorption behavior for the two excitation energies is qualitatively similar for the two excitation energies under short pulses, it differs distinctly for the long and more intense pulses. At low incident fluences, the fluorescence cross-section is higher at 9015 eV than at 9170 eV, which is consistent with the tabulated absorption cross-sections near the edge [57]. However, at higher fluences, the fluorescence yield at 9015 eV decreases more rapidly, resulting in a crossover in the relative emission efficiencies between the two energies (see Fig. 3.9B and E). This provides clear evidence that not only has the average cross-section of the atomic ensemble decreased, but also that the K-edge has shifted beyond the incident pulse energy of 9015 eV.

When the copper nanoparticles are exposed to pulses at 8910 eV, which is below the absorption edge, the absorption cross-section is minimal, and fluorescence is not expected. However, when the incident fluence is high enough, the excitation of lower-bound states induce M-shell vacancies and the K- to M-shell transition (8905 eV) becomes resonant with the excitation pulse energy, thereby leading to a sudden increase of the absorption cross-section and eventually fluorescence emission (Fig. 3.9C and F). Since the photon energy is below the copper's original K-edge, this fluorescence can only be attributed to the K-M-shell resonance. The effect is even more pronounced for longer pulses, where the incident fluence is approximately ten times higher than for the shorter pulses. In both cases, the resonance appears at the same incident fluence ($10^3 - 10^4 \text{J/cm}^2$), indicating that on femtosecond timescales, the resonance is governed by the energy deposited in the particle rather than the pulse duration. We also note that the resonant emis-

sion happens in the same fluence region where the cross-over happens for SA, suggesting a similar underlying response of lower-bound electronic states.

3.5 Photon statistics

The short incident pulse durations, comparable to the coherence time determined by the K_α linewidth, allow for the analysis of speckle patterns from partially coherent fluorescence in single exposures [68]. This, in turn, provides information about the effective XFEL pulse duration i.e. the timescale over which the absorption edge shift induces transparency [85, 90]. To validate this so-called self-gating effect as well as the assumption of transform-limited pulses in section 3.1.1, we analyze the speckle contrast of the fluorescence emission according to section 2.6. Figure 3.10 illustrates the speckle contrast as a function of μ at 9015 eV and 9170 eV for both short and long pulses. For low μ, the limited number of higher photon counts introduces a significant variability in the estimation of the speckle contrast. As the signal level increases, the speckle contrast converges to $\beta = 0.0465$ and 0.053 for short pulses at 9015 eV and 9170 eV, respectively. Interestingly, the speckle contrast yields similar results for the long pulses, namely $\beta = 0.052$ and 0.053 at the same photon energies.

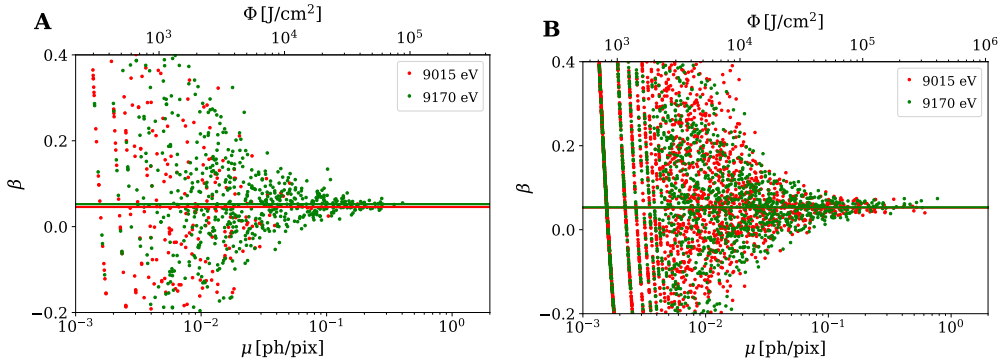


Figure 3.10: Speckle contrast of the K_α fluorescence as function of fluorescence signal per pixel μ for short (**A**) and long (**B**) pulses at 9015 eV and 9170 eV. The solid lines indicate the converged value of the speckle contrast for high μ.

Although this seems surprising at first, this behavior can easily be understood when considering the spiky nature of the SASE pulses. Despite being ten times longer, the long pulses had a ten times higher pulse energy of 2 mJ (versus the 200 µJ of the short pulses), resulting in the same peak intensity within these spikes.

Consequently, we infer that the same number of SASE spikes induce the absorption and emission processes that eventually contribute to the speckle contrast. In line with the standard methodology in the literature [39, 40], we can estimate the effective pulse duration T from the speckle contrast according to Eq. 2.59. With a coherence time τ_c of 0.49 fs, this yields an effective pulse duration of 1.8 fs which is in good agreement with the pulse durations retrieved from the HIREX spectra in section 3.1.1. This effective pulse duration corresponds to 35 % self-gating for the short pulses and about 93 % for the long pulses. This is much more than the so-far reported 35 % by Inoue *et al.* [85] for bulk material.

3.6 Summary

In this chapter we demonstrated the first true imaging of single nanoparticles smaller than the incident X-ray beam using IDI. This was achieved by combining IDI with conventional CDI for calibration and orientation determination. Despite having a much reduced emission from the single particles and a reduced particle hit rate, we achieved a resolution of 20 nm, more than one order of magnitude better than previously reported [39, 40]. At the same time the number of required shots could be reduced by four orders of magnitude, primarily due to the fact that the smaller sample size allowed a much closer detector placement and collecting a larger signal. Contrary to previous expectations, higher incident fluences and higher photon counts on the detector did not necessarily yield higher $g^{(2)}$-signals. Instead, it appears that intense X-ray pulses alter the electronic structures of the particles in a manner that reduces the efficiency of IDI. This could be confirmed by the spatial approach of the standard Hanbury Brown & Twiss [30] methodology which was adapted to an imaging setup where fluence fluctuations strongly contribute to the overall q-independent scaling of the second-order intensity correlation function. An unexpected reduction of the visibility ν at fluence levels above $1 \times 10^2\,\mathrm{J/cm^2}$ was observed, hinting at another fluence-dependent source of background. We hypothesize that this background may arise from shot-wise fluctuating *amplified spontaneous emission* (ASE) [75, 76], which, in our experiment already occurs for lower peak intensities ($1 \times 10^{17}\,\mathrm{W/cm^2}$) than the reported $1 \times 10^{19}\,\mathrm{W/cm^2}$ for ASE in bulk copper [75]. The ASE, being phase coherent, would not adversely affect the speckle contrast, explaining the inconsistency between the two measures of the degree of coherence.

From our analysis of the coherence properties of the fluorescence emission, we can

report the same speckle contrast of $\beta \approx 0.05$ for the short (nominal 2.5 fs) and long (nominal 25 fs) XFEL pulses. In line with the reasoning of Inoue *et al.* [39] and Trost *et al.* [68] this would correspond to pulse shortening due to self-gating of 35 % and up to 93 % for the short and long pulses, respectively. These results also indicate that the important parameters that lead to the reported changes in the absorption cross-section are energy per FEL spike and the number of spikes, as both pulse durations provided the same energy per spike. This also implies that care must be taken when interpreting the data in terms of a single Gaussian pulse duration. In addition, we observed for the first time non-linear reverse saturable absorption and saturable absorption in single copper nanoparticles as predicted by Cardoch *et al.* [90]. Our results confirm that, on femtosecond timescales, the non-linear response primarily depends only on the incident fluence and not on the pulse duration.

Chapter 4

Nanoscale X-Ray Imaging with High Spectral Sensitivity Using Fluorescence Intensity Correlations

Many of the experimental challenges of IDI described in the previous chapter can be addressed by a technique that we call *Spectral Incoherent Diffractive Imaging* (SIDI). Most of the following discussions are in line with those in our paper:

T. Wollweber *and K. Ayyer, "Nanoscale x-ray imaging with high spectral sensitivity using fluorescence intensity correlations," Structural Dynamics, vol. 11, no. 2, Mar. 2024, AIP Publishing.*

Authors Contributions:
Tamme Wollweber: Conceptualization (supporting); Investigation(lead); Software (lead); Writing – original draft (equal).
Kartik Ayyer: Conceptualization (lead); Funding acquisition (lead); Investigation(supporting); Methodology (lead); Supervision (lead); Writing – original draft (equal)

SIDI enables spectrally resolved imaging by substituting one dimension of the wave vector $\mathbf{k}$, with the photon energy E. Figure 4.1 illustrates how this can be achieved by introducing an analyzer crystal between the sample and the detector, effectively acting as a mirror along one of the $\mathbf{k}$ dimensions, while employing Bragg reflection along the other dimension to split the photons according to their energy.

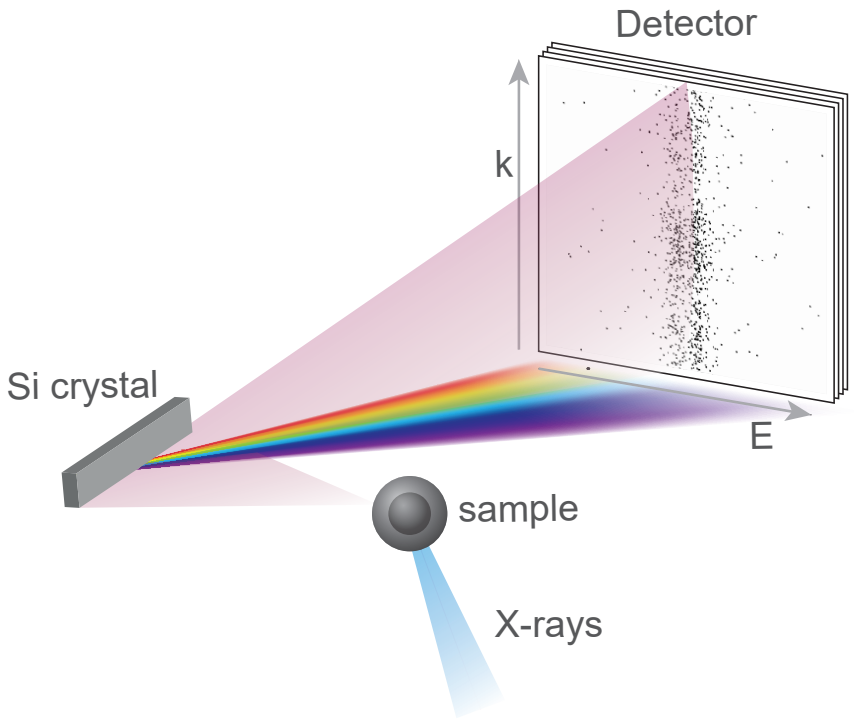


Figure 4.1: Schematic of the *Spectral Incoherent Diffractive Imaging* (SIDI) setup. The silicon crystal analyzer disperses the emitted photons in one direction while acting as a simple mirror along the orthogonal dimension. Thus, the position of a detected photon on the two-dimensional detector in the far field corresponds to its energy and one component of its wave vector.

Hence, when the intensity correlations are performed for different energies independently, SIDI can achieve much better energy resolution than conventional IDI, thereby increasing the coherence time of the emitted light field and eventually the $g^{(2)}$-contrast.
Furthermore, SIDI exhibits sensitivity to subtle shifts in the spectral emission profile for different oxidation states, analogous to *X-ray Emission Spectroscopy* (XES). XES has become an essential tool for investigating electronic transitions across various research fields such as physics, material science and environmental sciences [95]. Particularly, $3d$ transition metals are frequently studied using XES to analyze K_β line intensities and shifts corresponding to different oxidation states when bonding to different ligands [95–97]. This is in particular interesting for the search of new catalysts or more efficient energy storage materials. While

the combination of XES with conventional CDI or crystallography [98, 99] allows simultaneous imaging of the emitter distribution and the recording of emission spectra, elastic scattering cross-sections are only very weakly sensitive to changes in the oxidation states and so only information about the relative populations of different oxidation states is obtained. In conventional IDI, where the entire emission spectrum is combined, this leads to loss of contrast since the correlation of photons with different energies adds to the background. This problem was circumvented to some extent in prior experiments by filtering out the K_β emission and correlating just the oxidation-state-insensitive K_α photons [39, 40]. Our proposed approach provides the flexibility to position the detector strategically, enabling the acquisition of specific regions of interest, such as only the K_α or even the more sensitive $K_{\beta 1,3}$ and $K_{\beta 2,5}$ lines (see Fig. 2.1). This facilitates the study of structures with heterogeneous oxidation states, where only subtle shifts in the emission spectra occur. Leveraging the potential for time-resolved measurements at XFELs, our method opens the possibility of simultaneously capturing spatially and spectrally resolved movies of redox reactions in complex systems.

4.1 Simulations

To illustrate the principle of spectrally resolved imaging of nanostructures, consider first a spherical Mn nanoparticle, which is exposed to a 6.2 fs long, 6580 eV SASE XFEL pulse. The incident X-ray pulse was simulated[1] as a Gaussian function with a full width at half maximum (FWHM) of 6.2 fs. Depending on the energy resolution of the actual sample-detector configuration, the pulse was binned into different temporal modes M. The photon occupancy in each mode was then calculated from the Gaussian distribution while allowing for 80 % variations to account for SASE beam fluctuations. A flat silicon analyzer crystal and the detector are positioned to satisfy the Bragg condition for the silicon 422 peak concerning the $K_{\alpha 1}$ and $K_{\alpha 2}$ lines (refer to emission properties in Table 2.1). We expect 4000 photons per exposure on a 1024×1024 pixel detector with a pixel size of 75 µm at an effective detector distance of 1 m. Details about signal estimation are described in Appendix B.1. In conventional IDI, the K_α fluorescence of Mn is characterized by a coherence time of $\tau_c = 0.5$ fs (see Tab. 2.1). Considering our

[1] The code for both simulation and $g^{(2)}$-calculation are available at `https://github.com/TammeWollweber/spectralIDI`.

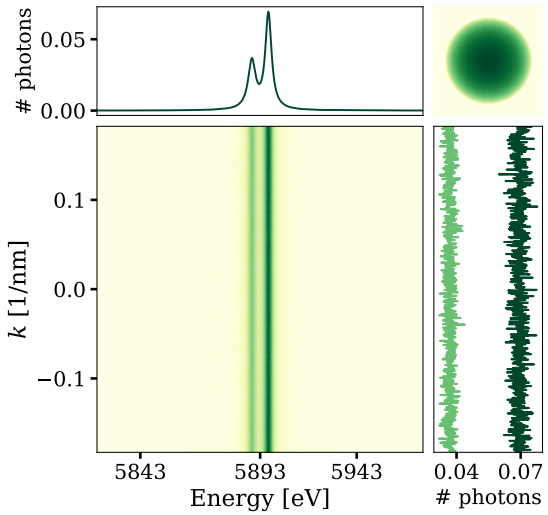


Figure 4.2: Integrated 2D detector image showing the two K_α lines of Mn. As expected, there is no structure along the k-axis. The inset in the upper right shows the projection of the spherical nanoparticle.

experimental geometry and small sample volume, the energy resolution is constrained primarily by the pixel size of the detector, which results in an effective resolution of 295 meV and a corresponding increase of the coherence time to 4.4 fs and the coherence length to 1.3 µm. The energy resolution can be increased by an order of magnitude with the use of back-scattering analyzers as employed in *Resonant Inelastic X-ray Scattering* (RIXS) experiments [100][2]. In order to retrieve the Fourier amplitudes $|F(q)|$ from the flat intensity profile along q, we calculate the second-order cross-correlation function $g^{(2)}(q)$ (see Eq. 2.53). In the case of spectrally dispersed photons, the recorded photons have both a measured wave vector, k, and a photon energy, E, yielding the correlation function $g^{(2)}(q, E_1, E_2)$. Two special cases of this three-dimensional function are especially interesting. The first is when we correlate photons of the same energy ($E_1 = E_2 \equiv E$), yielding $g^{(2)}(q, E)$, which we explore in Section 4.3. One can also average over all pairs of photons with the same energy difference, $\Delta E = E_1 - E_2$, giving $g^{(2)}(q, \Delta E)$. The application of such a marginalization will be investigated in Section 4.2.
The statistical significance of the measured $g^{(2)}$-value in comparison to the null hypothesis of $g^{(2)} = 1$ is expressed through the Z-score:

[2]In order to retain one **k** dimension, the surface needs to have a cylindrical profile rather than a spherical one.

$$Z\text{-score}(\mathbf{q}) = \frac{\langle I(\mathbf{k})I(\mathbf{k}+\mathbf{q})\rangle \sqrt{N}}{\sqrt{\left\langle \left(I(\mathbf{k})I(\mathbf{k}+\mathbf{q})\right)^2 \right\rangle - \langle I(\mathbf{k})I(\mathbf{k}+\mathbf{q})\rangle^2}}\,, \tag{4.1}$$

where N is the number contributing frames.

4.2 Coherence between K_α decay channels

Figure 4.2 displays the integrated far-field intensity for the two $K_{\alpha 1,2}$ lines after 10 000 exposures, showing well-separated flat intensity profiles along q, as expected. Summing the integrated intensity along q yields the emission spectrum similar to a conventional XES experiment as seen in the horizontal profile in Fig. 4.2. However, the intensity correlation approach can provide more insight into the coherence of the quantum evolution of the system following the creation of the $1s$ core hole. If the decay occurs before decoherence due to coupling with the environment, the measured intensity will be a coherent combination of the two photon wavefunctions for each spectral line:

$$I \propto |\Psi|^2 = |\psi_{\alpha 1} + \psi_{\alpha 2}|^2\,, \tag{4.2}$$

This result differs fundamentally from the case where emission from the two different decay channels combines *incoherently*,

$$I \propto |\psi_{\alpha 1}|^2 + |\psi_{\alpha 2}|^2\,, \tag{4.3}$$

By correlating the photon positions between the two spectral lines, the two-dimensional $g^{(2)}(q, \Delta E)$ can be used as a measure of the phase coherence, and thus the degree of superposition of the two quantum states $L_1(2_{\mathrm{p},1/2})$ and $L_3(2_{\mathrm{p},3/2})$ associated with these emission lines (Fig. 2.1). The corresponding two-dimensional spatial intensity correlations are shown in Fig. 4.3A and 4.3B for the coherent (Eq. 4.2) and the incoherent (Eq. 4.3) sum of the wave functions, respectively. The shape of the central vertical profile remains the same in both cases, as seen in the sum of the autocorrelation for each detector column. However, the inter-level components in Fig. 4.3A distinctly reveals $g^{(2)}$-correlations for a ΔE value of $E_{\mathrm{K}_{\alpha 1}} - E_{\mathrm{K}_{\alpha 2}}$, which are absent when the wave functions are added incoherently

(Fig 4.3B). In both cases, there are weak first-order fringes visible along the q dimension. However, the Z-score is only significant for the central speckle, as shown in Fig. 4.3C and Fig. 4.3D. In order to achieve higher $g^{(2)}$-contrast and better SNR, it would be necessary to increase the number of photon counts or to acquire more frames [36].

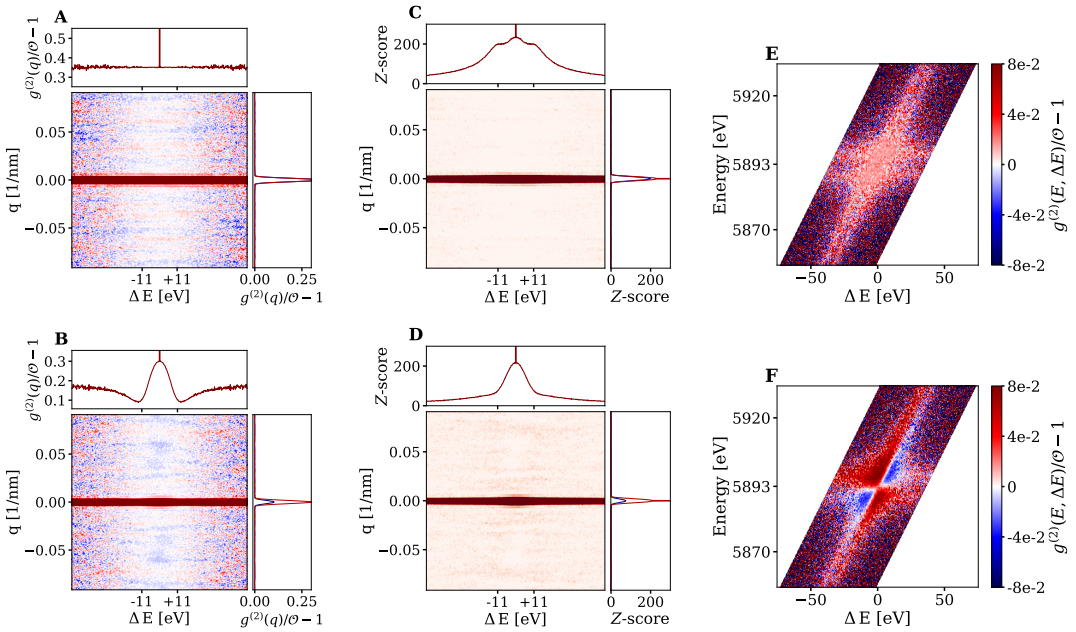


Figure 4.3: K_α SIDI simulations. The top row shows the behavior for full phase correlation between the $K_{\alpha1}$ and $K_{\alpha2}$ wavefunctions, while the bottom row shows the case of no phase correlation. (**A, B**) $g^{(2)}(q, \Delta E)$ images obtained by averaging 2D intensity correlations for each exposure. (**C, D**) Z-score for the images in **A** and **B**, respectively. The horizontal profiles in (**A** – **D**) correspond to the central line cuts and the vertical profiles to the central (red) and the off-central cuts (blue) at a ΔE value of $E_{K_{\alpha1}} - E_{K_{\alpha2}}$. (**E, F**) $g^{(2)}(E, \Delta E)$-signal for $q = 2.14\,\mu m^{-1}$ showing a clear difference between the two cases.

As already shown in Figs. 4.3A and 4.3B, SIDI yields the second degree of coherence for different energy separations. In fact, the underlying data can be analyzed as a three-dimensional correlation function $g^{(2)}(q, E, \Delta E)$, which is now also a function of the energy of the first photon. Figures 4.3E and 4.3F show the variation of the correlation $g^{(2)}(E, \Delta E)$ for a fixed q. For the coherent case in Figure 4.3E, the magnitude of the correlation signal is independent of the energies of the photons involved, just becoming more noisy for the cases where the photons are chosen far from the spectral peaks. However, when the wave functions are combined incoherently in Figure 4.3F, one sees a significantly lower value when

the two photons are from different spectral peaks rather than from the same peak. The projection over all E values here gives the horizontal line plot in Figure 4.3B, showing a minimum near the peak separation of 11 eV. In the simulations in this section, we neglect one effect which will dampen the signal at large $|\Delta E|$, namely that the interference signal is lost if the frequencies of the photons are too different. The difference between the coherent and incoherent cases will be most apparent experimentally at ΔE values less than 10 eV where the beat period between the two frequencies is comparable to the lifetime (see horizontal line cuts in Fig. 4.3C and D).

4.3 Nanoscale mapping of oxidation states

Let us now consider the case of a heterogeneous nanoparticle comprising a Mn sphere encapsulated in a MnO or similar Mn^{2+} shell (see sample inset in Fig. 4.4). The sample was approximated as a 300 nm sphere, in the heterogeneous case with an inner core of 215 nm of Mn and a 85 nm shell of Mn^{2+}. The particle is excited with a photon energy of $E_{\text{elastic}} = 6580\,\text{eV}$, which is 41 eV above the K-edge and 90 eV above the $K_{\beta 1,3}$ emission line. The Si analyzer and the detector are positioned to capture the $K_{\beta 1,3}$ lines as well as the elastic scattering at a detector distance of 1.5 m. By exploiting the atomic form factor of elastic scattering, its relative intensity can be tuned by placing the Si crystal near-normal to the incident $\mathbf{k}_0$ vector. We expect 250 photons per exposure due to the lower fluorescence yield of the $K_{\beta 1,3}$ line as well as the reduced solid angle of the detector (see Appendix B.1). We simulated 1 000 000 exposures, which would correspond to about 1 hour of data acquisition at the European XFEL [40].

The integrated intensity in Figure 4.4 shows both the K_β lines and the coherent diffraction of the entire particle due to its insensitivity to the oxidation state. The spectral shift for the $K_{\beta 1,3}$ line from neutral Mn metal to the Mn^2+ oxidation state is 1.7 eV [101]. However, since the shift is less than the width of the individual emission lines, the integrated intensity exhibits only one broadened $K_{\beta 1,3}$ emission line. Given that the emission for the two different $K_{\beta 1,3}$ lines arises from two distinguishable materials of distinct shapes, it is reasonable to perform the $g^{(2)}$-calculation solely along the q-direction. Additionally, a 2D analysis would be counterproductive here, as it would include correlations from the elastic scattering that contribute only to the offset in the second-order correlation function (see

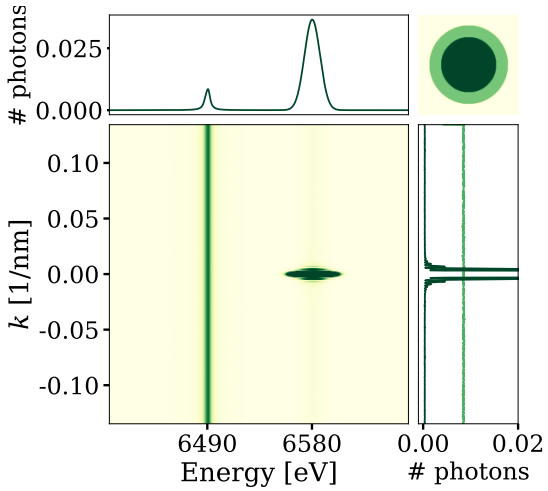


Figure 4.4: Integrated 2D detector image showing the broadened K_β lines of the Mn-Mn^{2+} compound as well as coherent elastic scattering. One can already see the structure of the whole particle reflected in the coherent signal (dark profile to the right), while the fluorescence yields a flat profile (light green).

Eq. 2.53). In Fig. 4.5A the one-dimensional $g^{(2)}(q, E)$ profiles for the different energies are shown. Notably, discernible differences along q are evident for different energies within the broadened $K_{\beta 1,3}$ line. The different central peak widths reflect the different shapes of the underlying emitter distributions in the $Mn - Mn^{2+}$ compound contributing to each emission line. Higher order features in the q direction contain information about finer structural features. For the elastic scattering, the $g^{(2)}$-profile remains flat and does not provide any additional information, as expected. Figure 4.5B shows the $g^{(2)}(q)$ line profiles. One can clearly see the different Fourier amplitudes corresponding to the core and shell for the two $K_{\beta 1,3}$ energies.

In an experiment where SIDI is combined with forward scattering for coherent diffraction, the detector can also be positioned farther away from the interaction region to enhance the energy resolution and, particularly, to increase the splitting for the two $K_{\beta 1,3}$ lines. This would improve the $g^{(2)}$-contrast on the one hand, but also decrease the solid angle of the detector leading to a lower photon count per exposure and thus a lower SNR. One can also envision using a different analyzer crystal geometry for higher energy resolution, efficiency or both [95].

In this example with manganese, we utilized $K_{\beta 1,3}$ line shifts in order to visualize the core-shell structure. In other systems it may be more efficient to use changes in other decay channels, including K_α energy and width changes. While these effects may be smaller, this must be balanced with the much higher count rates

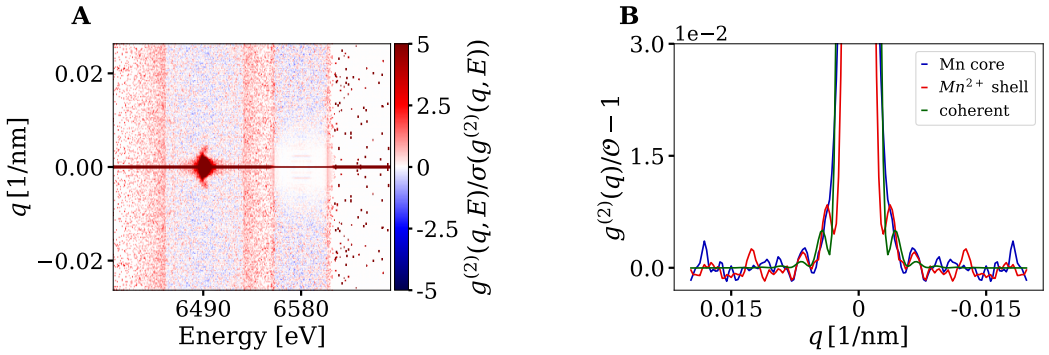


Figure 4.5: K_β simulations for the Mn-Mn^{2+} compound. (**A**) Intensity correlations $g^{(2)}(q, E)$ for each energy channel, i.e. for each pixel column of the detector independently, normalized by its standard deviation. Since the spatial distribution of each Mn subspecies differs (see inset in the upper right of Fig. 4.4), one can see different signals within the K_β line. (**B**) The energy-dependent line profiles along q for the two oxidation states can be used to independently reconstruct the structure of each state.

for the K_α emission. In the event where one is studying a heterogeneous structure with different elements, then one can use any of the emission lines, and possibly even combine the signal from all of them to obtain the substructure images.

4.4 Summary

To overcome the limitations of conventional IDI regarding short coherence times associated with core-shell fluorescence, we introduced *Spectral Incoherent Diffractive Imaging* (SIDI). This method enables spectrally sensitive imaging by replacing one **k**-dimension by the photon energy. A silicon analyzer crystal, positioned between the sample and detector, disperses photons based on their energy (via Bragg reflection) while preserving one component of the wave vector, effectively encoding both spatial and spectral information. The simulations presented here demonstrate the feasibility of SIDI for imaging Mn nanoparticles and heterogeneous Mn/Mn^{2+} core-shell structures using realistic XFEL parameters. The second-order intensity correlation function is used to retrieve structural information from spectrally resolved data. Furthermore, the technique can probe quantum coherence between decay channels (e.g., $K_{\alpha 1}$ and $K_{\alpha 2}$), distinguishing coherent and incoherent emission via differences in $g^{(2)}(q, \Delta E)$.

When applied to a mixed-oxidation-state sample, SIDI enables nanoscale mapping of oxidation states by resolving structural differences encoded in energy-dependent $g^{(2)}(q, E)$ correlations. This capability opens pathways for real-time, spatially and spectrally resolved imaging of redox dynamics in functional materials and catalysts.

Chapter 5

Perspectives for Optical Sensing at Room Temperature Using Fluorescence Intensity Correlations

The previous two chapters explored the potential of intensity correlation techniques for dark-field imaging in the X-ray regime. In this chapter, we will explore the potential applications of these methods in optical sensing within the visible spectrum. In this context, the use of intensity correlations for imaging is commonly referred to as intensity interferometry, a concept first introduced by Hanbury Brown and Twiss in 1956 [30]. Since then, intensity interferometry has been extended to imaging through scattering media such as ground glass diffusers, biological tissues, and turbulent air [102–104]. These implementations typically rely on wavefront modulations of otherwise coherent light sources, such as lasers. In contrast, this chapter focuses on performing intensity correlation analysis on intrinsically incoherent fluorescent light sources, where additional factors must be taken into account, such as fluorescence lifetime, spectral broadening, limited fluorescence yield, and photobleaching.

Using fluorescence for dark-field imaging in the visible regime is well established and has been used for many years in the field of microscopy [28]. With high-NA[1] objectives, it is possible to achieve resolutions down to 200 nm [105]. Modern tech-

[1]The numerical aperture (NA) of an objective is defined as: $\mathrm{NA} = n \sin\theta$, where n is index of refraction of the working medium and θ is the half-angle of the maximum cone of light that enters the objective.

niques that exploit non-linear emission phenomena, such as STED microscopy, can even achieve resolutions down to 20 nm [42, 106] (see chapter 1).

The first step is to demonstrate in a proof-of-principle experiment that IDI can be used in the visible regime. This is a non-trivial task, as the coherence properties of the emitted fluorescence are significantly different from those of X-ray fluorescence. The excitation and emission processes in the visible regime happen in the outer valence states and are strongly influenced by environmental conditions (see also chapter 1). This leads to a broad homogeneous spectral broadening of the emission profile, up to several hundred nanometers, depending on the material. In recent years, new materials have been reported where nanoparticles exhibit narrow emission lines even at room-temperature [107]. However, the central emission wavelength of these particles is typically very sensitive to the shape and size of the individual particle, leading to heterogeneous broadening of the emission lines [107]. In this chapter, the experimental setup and methods used for IDI in the visible regime are discussed. First, an optical implementation of 2D IDI is introduced, followed by a spectrally-resolved IDI setup, analogous to the X-ray case presented in chapter 4. Finally, the challenges of IDI in the visible regime are discussed, including the limitations of the proposed experimental setups and the potential for future improvements.

5.1 Experimental Setup and Methods

Conceptually, the experimental setup for IDI in the visible regime could be implemented in a similar way as in the X-ray regime, as discussed in chapter 3, where the fluorescence emission is directly measured in the far field. In the visible regime, however, high-NA objectives can be used to increase the number of collected photons. The propagated far-field equivalent is then encoded in the back focal plane (BFP) of the objective. Furthermore, bandpass filters can be used to reduce the spectral width of the emitted fluorescence, and thus increase the coherence time of the light field. For visible light, the detection of single photons is much more challenging than in the X-ray regime, as each photon creates only a single electron in the detector. Therefore, the detection of single photons requires specialized detectors that amplify the electric signal, such as *electron multiplying charge-coupled devices* (EMCCDs) or intensified *complementary metal–oxide–semiconductor* (CMOS) detectors. This is in contrast to the X-ray

case, where each photon has enough energy to create electric signals that are well above the noise level of the detector.
Figure 5.1 shows the schematic optical setup for 2D IDI. The sample is excited by a 450 nm laser (*Thorlabs NPL45C*) with a pulse duration of 6 ns and a peak power of 1.2 W. The light is circularly polarized using a quarter-wave plate. A 1D grating can be inserted upstream of the focusing lens to create a 1D diffraction pattern on the sample (see Fig. 5.4). The emitted fluorescence is then collected by an infinity-corrected objective lens (*Mitutoyo 10x/100x* or *Olympus 100x Plan Fluorite Oil Immersion Objective*) with numerical apertures of 0.28, 0.7, and 1.33, respectively. The exact setup configurations for the results presented in this chapter are listed in table C.1.

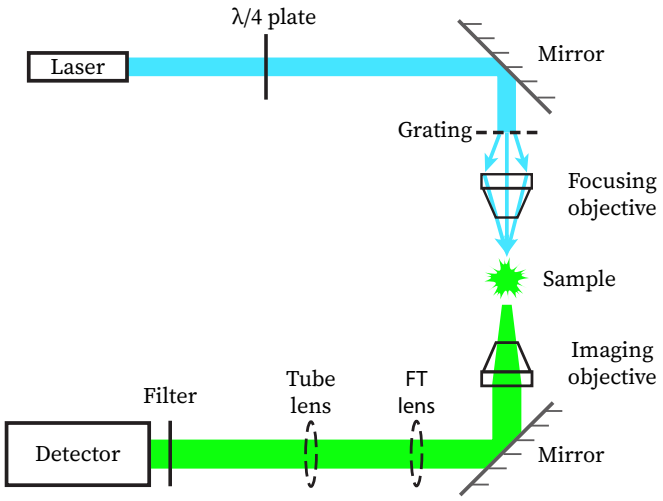


Figure 5.1: Schematic of the optical setup for 2D IDI in the visible regime. The sample is excited by a 450 nm circularly polarized laser pulse and the emitted fluorescence is collected by an infinity-corrected objective lens and subsequently filtered and directed towards the detector. The setup allows direct imaging of the focal plane of the objective via the tube lens, or, alternatively, imaging of the BFP using the so-called FT-lens. For details, see text.

The setup allows switching between two different imaging modes: (i) direct imaging of the focal plane of the objective via the tube lens, or (ii) imaging of the BFP using the so-called FT-lens. It is worth noting that, when using infinity-corrected objectives, the far field information is not just the propagated wave field downstream of the objective (which is a collimated wave field), but rather is encoded in the BFP of the objective. This BFP can even lie inside the objective itself.

Hence, the FT-lens and the detector have to be positioned to perform one-lens imaging of this BFP to retrieve the far field diffraction pattern. The fluorescence is filtered by a band-pass filter (*Thorlabs FB532-4* or *Photonic Solutions Ultra narrow bandpass filter*, 532 nm, FWHM $\leq$ 0.2 nm) to reduce the spectral width of the emitted fluorescence as well as environmental background. Ultimately, the fluorescence is detected by an intensified CMOS detector (*Andor iStar sCMOS*). This detector is equipped with a micro-channel plate (MCP) that amplifies the photoelectric signal from the photocathode. These secondary electrons are accelerated towards a phosphor screen which converts the electric energy into photons. These are then directed via optical fibers towards the CMOS sensor. This amplification process allows for the detection of single photons even in the visible regime. Furthermore, the MCP can be gated with a delay to wait for the incident laser pulse to pass and only measure fluorescence with the shortest possible gating window of 3 ns. The CMOS sensor has 2560 $\times$ 2160 pixels with a pixel size of 6.5 µm, which corresponds to an active sensor area of 16.6 $\times$ 14 mm. The circular phosphor screen has a diameter of 18 mm, which reduces the active area at the corners of the sensor (see Fig. 5.2A). However, the spatial resolution of a measured photon on the CMOS sensor is not limited by the pixel size, but by the spatial resolution of the phosphor screen. The secondary electrons produced by the MCP and the subsequent phosphorescence produce electric signals that are spread over several pixels. Therefore, a 4 $\times$ 4 pixel binning is used, which also reduces data volume and detector downtime due to data transfer. The binned data is measured at a frame rate of 50 Hz.

During this work, we have used three different types of samples: (i) a rotating ground glass disc (GGD), (ii) a fluorescent slide (*Thorlabs FSK2, Green*), and (iii) a 50 µm thick cerium-doped (0.1 %) Yttrium-Aluminum-Garnet (YAG:Ce) crystal (purchased from *crytur*). The GGD is used as a test sample to ensure the functionality of the experimental setup. It is a thin glass disc with a rough surface that scatters the incident light and induces random phases of the scattered photons. This leads to shot-wise random speckle patterns in the far field, imitating the diffraction of an incoherent light source [102, 103]. The intensity correlations then yield the Fourier amplitudes according to Eq. 2.53.

The fluorescent slide is made of cast acrylic substrate with an (unknown) fluorescent dye embedded in the polymer matrix. The slide was thinned to a thickness of $\sim$500 µm to reduce the fluorescence background from outside the focal plane of the objective. The third sample, a YAG:Ce crystal, is a well-known material for optical applications due to its high fluorescence yield and photostability [108, 109]. Since

fluorescence emission at room temperature is typically very broad, a bandpass filter is used to reduce its spectral width, thereby increasing the coherence time. Generally, the coherence time associated with the spectral width of a bandpass filter can be calculated as follows:

$$\tau_c \approx \frac{1}{\Delta\nu} = \frac{1}{\left|\frac{d\nu}{d\lambda}\right| \Delta\lambda}$$
$$\Rightarrow \qquad \tau_c \approx \frac{\lambda_0^2}{c\Delta\lambda}, \tag{5.1}$$

where λ_0 is the central wavelength, $\Delta\lambda$ is the nominal spectral width of the bandpass filter, and c is the speed of light. For a 4 nm filter, the coherence time then yields $\tau \approx 236$ fs. Using the shortest possible gating time of the detector (3 ns), this corresponds to 12 700 incoherent modes. This is a significant increase compared to the X-ray case, discussed in chapter 3, where the temporal resolution of the imaging setup was on the same order of magnitude as the coherence time of emitted fluorescence. However, with the high fluorescence yield of the samples, combined with the high-NA objectives, the number of detected photons per frame is expected to be much higher in the visible regime.

5.2 Detector characterization

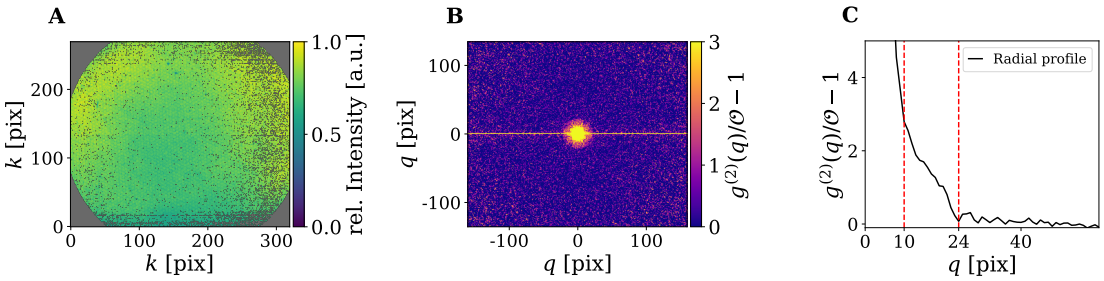


Figure 5.2: Detector characterization (Run #4). (**A**) Integrated far-field fluorescence intensity from the slide. (**B**) Intensity correlation $g^{(2)}(\boldsymbol{q})$ and its radial profile (**C**). The central peak is due to the cross-talk of the MCP, while the horizontal line is a common mode effect.

Figure 5.2 shows the characteristic detector behavior for the described experiment: the integrated far-field intensity from the fluorescent slide (Fig. 5.2A), the

intensity correlation $g^{(2)}(\boldsymbol{q})$ (Fig. 5.2B) and its radial profile (Fig. 5.2C). The integrated intensity shows the circular active area of the phosphor screen and the slight intensity variations which can be distinguished are due its non-uniform yield. Furthermore, the integrated intensity shows a weak honey-comb pattern which is a shadowing effect from the fiber coupling of the phosphor screen to the CMOS sensor. The intensity correlation $g^{(2)}(\boldsymbol{q})$ shows two distinct features that are independent of the underlying sample: (i) the central circular peak at the center is the so-called cross-talk induced by the MCP [110]. Within the MCP, secondary electrons are mainly accelerated by the electric field towards the phosphor screen. However, some secondary electrons can be scattered backwards and re-enter the MCP in a different channel (see Fig. 5.3).

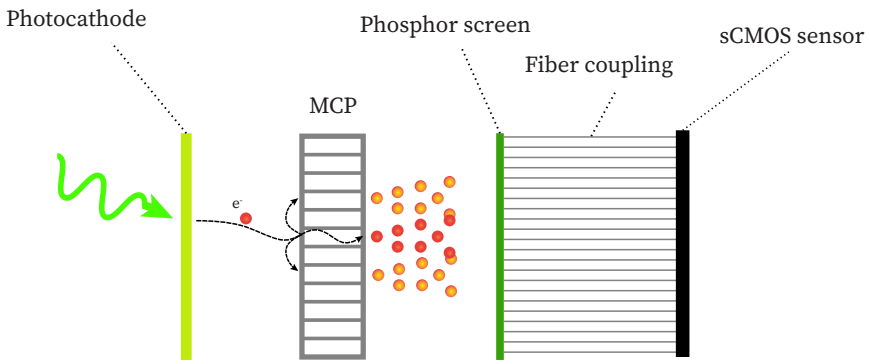


Figure 5.3: Schematic of the MCP cross-talk within an intensified CMOS detector. The incoming photon hits the photocathode and generates a photoelectron. This electron is accelerated towards the MCP by an electric field, where it generates secondary electrons. These secondary electrons are then accelerated towards the phosphor screen, where they generate photons that are detected by the CMOS sensor. However, some secondary electrons can be scattered backwards and re-enter the MCP in a different channel, leading to a correlation of the detected signal on the CMOS sensor and thus to a peak in the second-order correlation function at low-q.

This isotropic effect leads to a correlation of the detected photons and thus to a peak in the second-order correlation function at low-q. (ii) The second feature is a central horizontal line which is similar to a common mode effect known from charge-coupled devices (CCDs). To prevent potential signal overlap with this detector artifact, the detector is tilted by approximately $\sim 7°$ relative to the optical axis. From the radial profile of the $g^{(2)}(q)$ (Fig. 5.2C) two "orders" of cross-talk

can be distinguished, one up to 10 pixels and one up to 24 pixels. These detector characteristics and in particular the MCP cross-talk at low-q are much stronger than any correlation signal expected from the sample. In addition, the cross-talk is a statistical correlative effect which does not behave as a static background. Consequently, the best approach to correct for this cross-talk in the $g^{(2)}(q)$ is still uncertain. This is a significant limitation for this optical setup, as the low-q area contains the most relevant information about the sample.

5.3 2D IDI in the visible regime

In order to verify the correct operation of the experimental setup, the first measurements were performed using the GGD as a test sample. Figure 5.4 shows the real-space beam profile of the incident beam on the GGD and the corresponding $g^{(2)}(\boldsymbol{q})$, which exhibits interference fringes, as expected. From the size d of the real-space object and the position of the first maximum y_1 in the $g^{(2)}(\boldsymbol{q})$, the effective detector distance D can be calculated using geometric optics:

$$D = \frac{y_1}{\tan\left(\sin^{-1}\left(\frac{\lambda}{d}\right)\right)} \approx 16.8\,\text{mm} \tag{5.2}$$

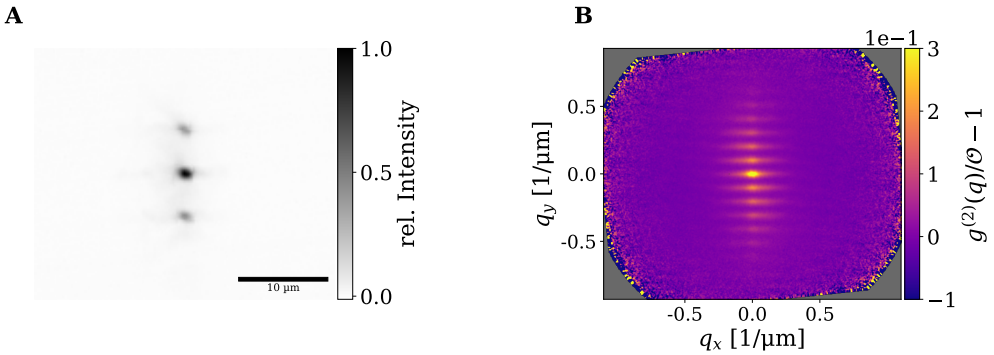


Figure 5.4: GGD verification (Runs #1 and #2). (**A**) Real-space beam profile of the incident beam on the GGD. (**B**) Corresponding $g^{(2)}(\boldsymbol{q})$, which exhibits interference fringes.

With the established setup, we then performed measurements on the fluorescent slide (Fig. 5.5). Over the course of the measurement, the intensity drops significantly due to bleaching of the fluorescent dye in the polymer matrix (Fig. 5.5B). This effect makes it difficult to obtain a reliable $g^{(2)}(\boldsymbol{q})$, as the bleaching indicates

a change in the spatial emitter distribution over time. On the other hand, we can exploit this bleaching effect by binning the data in time and subtract these intensity correlations from the first temporal bin (100 000 frames). The resulting $g^{(2)}(\boldsymbol{q})$ is shown in Figure 5.5D. As the expected correlation signal is smooth, we use a Gaussian filter to reduce the noise. The correlation shows a clear central speckle with an aspect ratio of 1:4, which matches the aspect ratio of the incident beam profile on the sample.

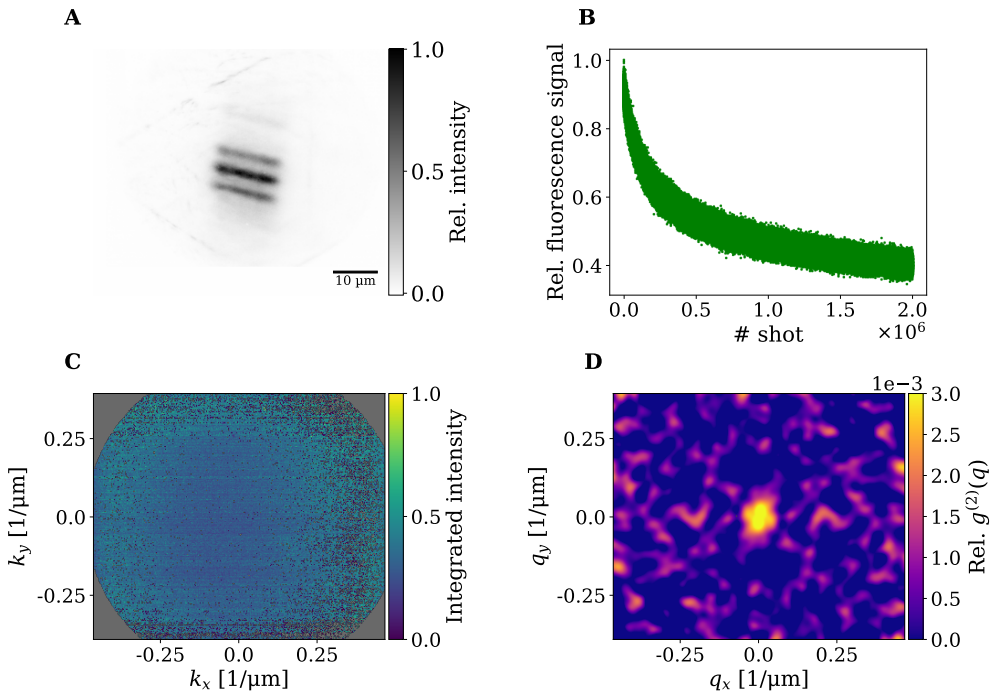


Figure 5.5: IDI of the fluorescent slide (Runs #3 and #4). (**A**) Real-space beam profile of the incident beam on the slide. (**B**) The fluorescence signal level decreases over time due to bleaching. (**C**) Integrated intensity of the whole measurement. (**D**) Gaussian filtered $g^{(2)}(\boldsymbol{q})$ of the first 100 000 frames, subtracted by the average $g^{(2)}(\boldsymbol{q})$ of the subsequent temporal bins, exhibiting the central speckle.

Now, in order to eliminate bleaching effects, the slide was replaced by the YAG:Ce crystal. Furthermore, the bandpass filter was changed to a 0.2 nm filter to increase the coherence time of the emitted fluorescence to $\tau_c \approx 4.72$ ps. With a polarizing filter, this corresponds to $\sim$ 635 incoherent modes. Figure 5.6A shows the real-space beam profile of the incident beam on the YAG:Ce crystal, the signal level over the whole measurement (B), the integrated intensity on the detector (C), and the $g^{(2)}(\boldsymbol{q})$ of $\sim$ 14 200 000 frames (D). Despite having reduced the number of incoherent modes by a factor of $\sim$ 40, there is no $g^{(2)}(\boldsymbol{q})$-signal visible outside

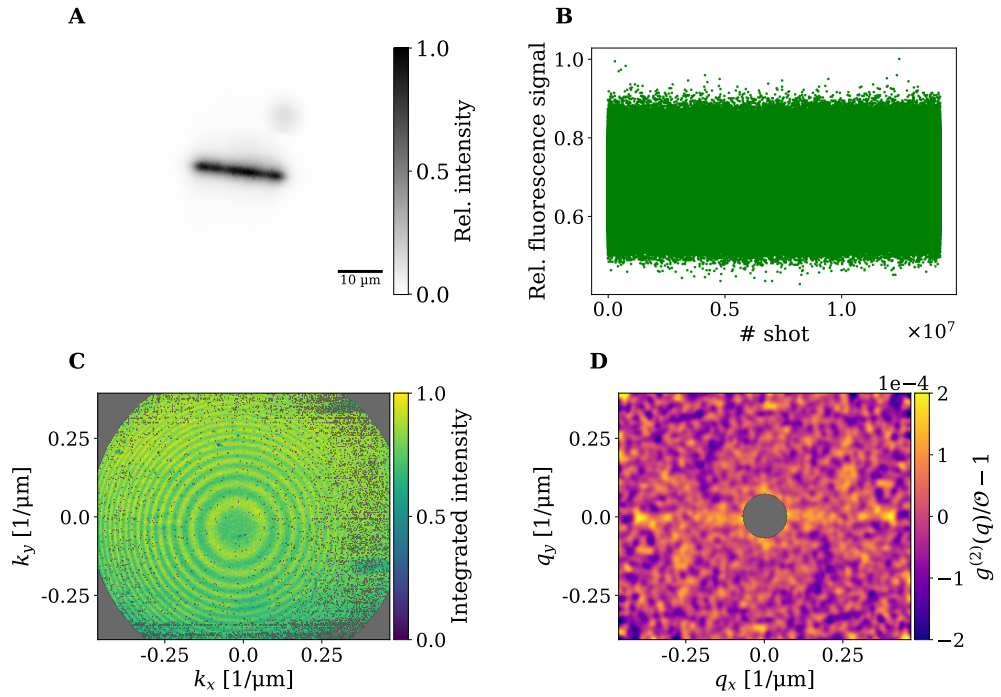


Figure 5.6: Fluorescence from YAG:Ce crystal (Runs #5 and #6). (**A**) Real-space beam profile of the incident beam on the YAG:Ce crystal. (**B**) Fluorescence signal level over the whole measurement. (**C**) Integrated fluorescence intensity. (**D**) 2D intensity correlation $g^{(2)}(\boldsymbol{q})$.

the (masked) cross-talk area. However, the integrated far-field intensity shows interference fringes in the form of Newton rings [111]. These rings are typically observed when coherent light is reflected between two closely spaced surfaces, one of which is a spherical lens and the other a flat reflective surface. The Newton rings are strongly pronounced for the thin 50 µm YAG:Ce crystal and when the ultra-narrow bandpass filter (0.2 nm) is used. For a 100 µm YAG:Ce crystal, the rings are much weaker, and for a 500 µm thick sample, the effect disappears completely. This indicates that the Newton rings only appear when the sample thickness is much less than the coherence length associated with the bandpass filter. In this case, the coherence length is $L_c = \tau_c \cdot c \approx 1.4\,\text{mm}$, which is much larger than the sample thickness of 50 µm. Since the fluorescence photons have random initial phases and are thus mutually incoherent, the interference fringes can only be explained by the self-interference of the emitted fluorescence photons. The fluorescence emission corresponds to a spherical wave field, that self-interferes with the reflection from the crystal surfaces. As the Newton rings are a static effect, they are corrected for by the normalization in the second-order intensity corre-

lation function $g^{(2)}(\boldsymbol{q})$ (see Eq. 2.53). However, with the ultra-narrow bandpass filter, the thin sample and the short gating time with respect to the fluorescence lifetime of the sample ($\sim$ 60 ns [109]), the number of detected photons per frame ($\sim$ 200) is significantly reduced and lower than the number of incoherent modes ($\sim$ 630) in the light field. If a sufficiently large number of frames is acquired, even a small number of detected photons per frame can yield a statistically significant $g^{(2)}(\boldsymbol{q})$-signal, as photons belonging to the same mode, will, statistically, be detected occasionally. However, due to the MCP cross-talk at low-q, there is no discernible $g^{(2)}(\boldsymbol{q})$-signal is observed, even after collecting more than 14 000 000 frames.

5.4 SIDI in the visible regime

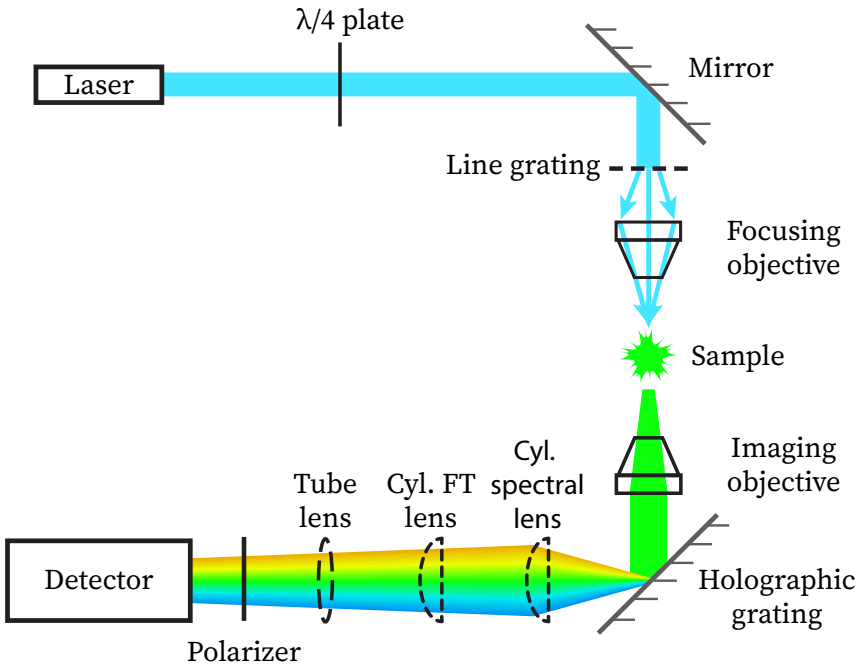


Figure 5.7: SIDI schematic setup, similar to the 2D IDI configuration. Here, a grating is placed downstream of the objective to spectrally disperse the fluorescence. The FT lens and the so-called spectral lens, which refocuses the photons according to their energy, are now cylindrical.

In order to increase the photon counts per frame while at the same time improve the energy resolution and thus the coherence time of the fluorescence light field, a spectrally-resolved IDI setup was implemented — equivalent to the X-ray setup

described in chapter 4. As shown in Figure 5.7, the setup is similar to the 2D IDI configuration, with the key distinction being the addition of a holographic reflective grating (*Thorlabs GH50-24V*) placed downstream of the objective to spectrally disperse the emitted fluorescence.

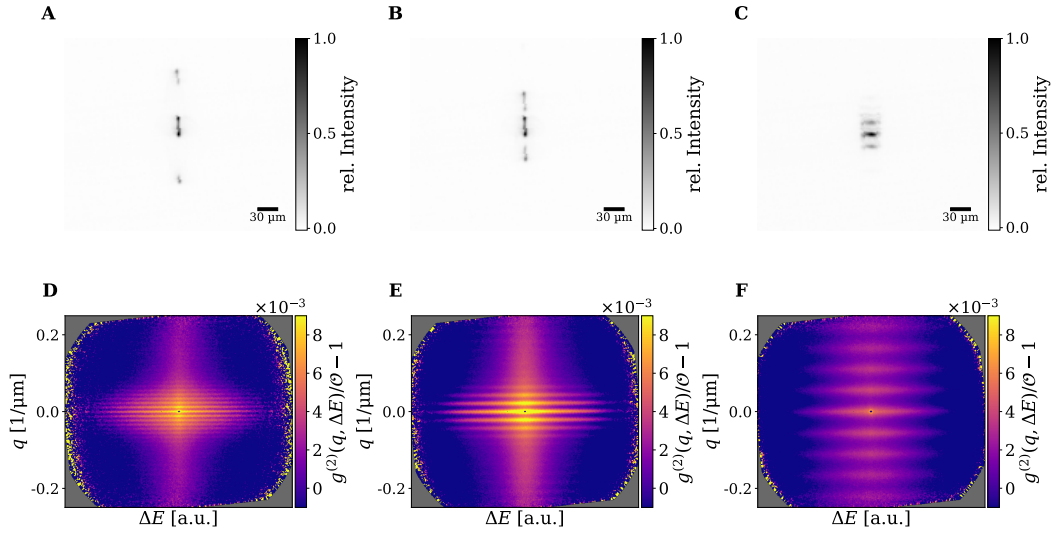


Figure 5.8: SIDI of the GGD (Runs #7 – #12). Top row: Real-space beam profiles on the GGD. Bottom row: Corresponding intensity correlation function $g^{(2)}(q, \Delta E)$.

The dispersing photons are then focused along the energy dimension using a cylindrical (spectral) lens. Accordingly, the FT lens is now also a cylindrical lens, which only images the BFP in the orthogonal direction. Repeating the procedure of the 2D IDI case, the spectrally-resolved IDI setup was first tested using the GGD test sample. Figure 5.8 shows the illuminated area for three different line spacings on the GGD (A-C) and the corresponding intensity correlation function $g^{(2)}(q, \Delta E)$ (D-F). The next step was to perform measurements on the fluorescent slide. To avoid bleaching effects as in Figure 5.5, the slide was rotated during the measurement (25 °/s). Figure 5.9 shows the real-space image in the focal plane (A), the integrated far-field intensity (B), and the corresponding $g^{(2)}(q, \Delta E)$ (C). While the $g^{(2)}(q, \Delta E)$ shows a clear central speckle, there are two caveats: (i) the correlation signal only appears when the sample is rotated during the measurement and disappears when the sample is stationary. This indicates that the correlation signal is not due to the actual illuminated area, but rather due to the sample rotating in and out of the focal plane of the objective. (ii) The $g^{(2)}(q, \Delta E)$ shows no energy dependence, which is physically unreasonable, and indicates that the grating is not dispersing the emitted fluorescence as expected. This is likely be-

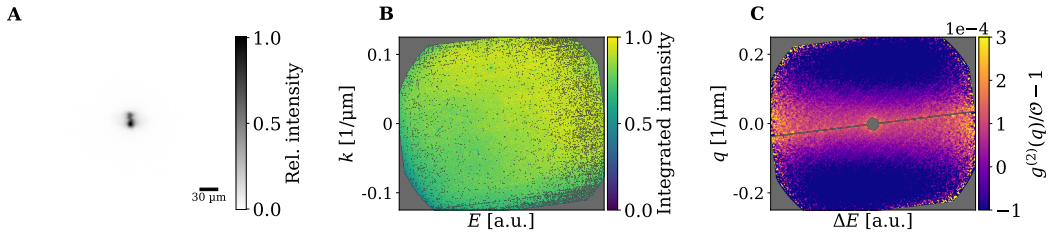


Figure 5.9: SIDI of the rotating fluorescent slide (Runs #13 and #14). (**A**) Real-space beam profile of the incident beam on the slide. (**B**) Integrated far field intensity. (**C**) Intensity correlation function $g^{(2)}(q, \Delta E)$.

cause the photons emerging from the objective do not form a single collimated light field, but rather a set of collimated yet diverging plane waves, determined by the lateral positions of individual emitters in the focal plane. Hence, with this angular divergence of the incoming fluorescence light field, the grating is not able to disperse the fluorescence photons according to their energy.

5.5 1D IDI

After testing 2D IDI and spectrally resolved IDI, let's take a step back and consider the simplest case — 1D IDI. For this, the setup is similar to the SIDI setup, using the two cylindrical lenses, but now the grating is replaced by a mirror. The detected fluorescence on the detector is then an image of the focal plane of the objective along one dimension, and orthogonally, the far-field fluorescence is detected (see Fig. 5.10). Compared to the setups discussed above, this 1D configuration has the advantage that many more photons can be detected per frame, as the imaging lens is refocusing all photons along one dimension onto the detector. This is different to the SIDI setup, where photons are lost in other diffraction orders of the grating.

In the 1D case, the second-order intensity correlation $g^{(2)}(q, \Delta x)$ is now a function of separation of the wave vectors q and the horizontal displacement vector Δx of the emitted photons. Figures 5.10C and D now show first signs of a $g^{(2)}$-signal outside the (masked) cross-talk area, most likely due to the higher photon counts per diffraction pattern. However, without being able to access the low-q information, it remains difficult to achieve a convincing result.

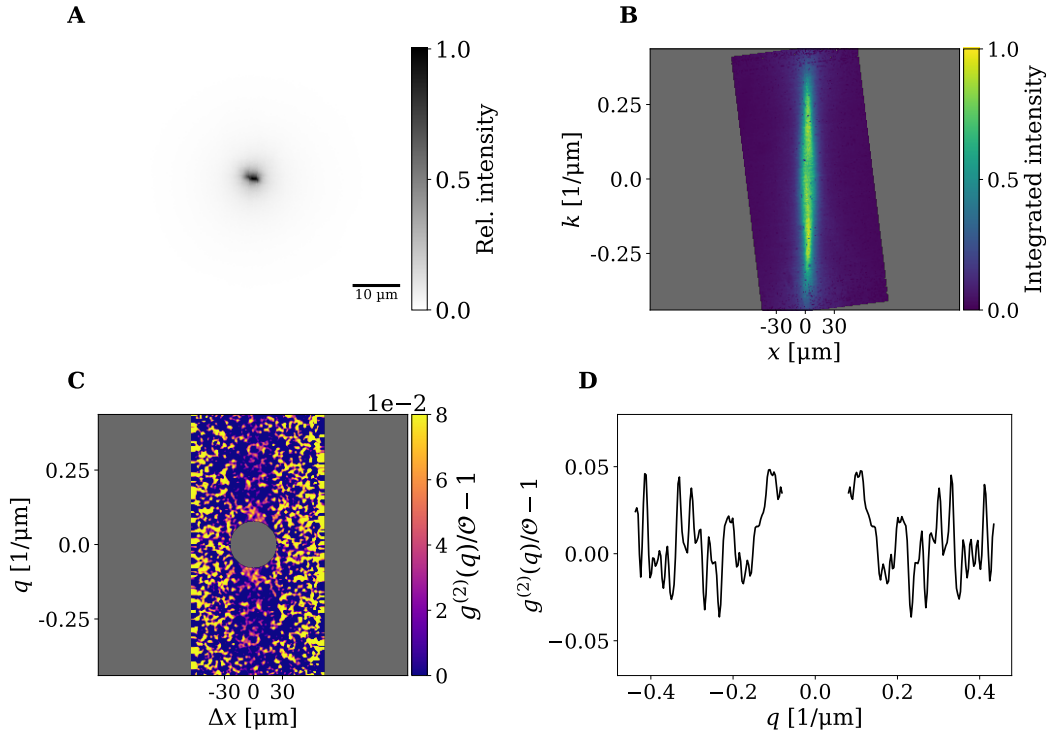


Figure 5.10: 1D IDI of YAG:Ce (Runs #15 and #16). (**A**) Real-space beam profile in the focal plane. (**B**) Integrated intensity of the fluorescence. Real-space imaging along the horizontal axis, and far-field intensity distribution along the vertical axis. (**C**). Intensity correlation function $g^{(2)}(q, \Delta x)$. (**D**) Vertical central line profile of $g^{(2)}(q, \Delta x)$.

5.6 Challenges of Optical IDI

The previous sections have shown that IDI can be performed in the visible regime, but there are several challenges that need to be addressed in order to achieve reliable results. Optical IDI at room temperature is mainly limited by the broad fluorescence emission spectra and the corresponding short coherence times compared to the temporal resolution of single photon detectors for visible light. With the use of an ultra-narrow bandpass filter, the coherence time can be increased to the order of picoseconds, but this comes at the cost of filtering out most of the photons. Furthermore, a picosecond coherence time is still three orders of magnitude shorter than the minimum gating time of detectors with a built-in MCP. Moreover, the MCP cross-talk is a significant limitation for the optical setup, as it is much stronger than any correlation signal expected from the sample. The cross-talk is a statistical correlative effect which does not behave as a static back-

ground. Therefore, it is difficult to subtract the cross-talk from the measured intensity correlations in a reliable manner. This is a substantial restriction for this optical setup, as the low-q area contains the most relevant information about the sample. Another well-established detector technology capable of single-photon detection without an MCP, the EMCCD, is limited by its temporal resolution ($\sim$ µs[112]) and is therefore not suitable for IDI. However, recently, two new detector technologies have been developed that provide single-photon detection with a temporal resolution of ≤ 200 ps: the time-gated *single-photon avalanche diodes* (SPADs) [113] and the *Timepix4* [114]. These detectors are not yet widely available, but they hold great potential for future IDI experiments in the visible regime. Another limiting factor of IDI in the visible regime are the long fluorescence lifetimes of many samples with respect to their coherence time. In the case of the YAG:Ce crystal, the fluorescence lifetime is ~ 60 ns [109], which is much longer than the coherence time of the emitted fluorescence ($\sim$ fs). Consequently, by gating the detector and using narrow bandpass filters, only a small fraction of the emitted photons is detected. This is a strong motivation to use a spectrally-resolved IDI setup, where no emission filters are needed and the emitted fluorescence can be detected over a relatively broad spectral range, while at the same time maintaining a high energy resolution, depending on the exact setup configuration. However, by using objectives with a high magnification, the collected light field is not a single collimated wave field but rather a set of diverging plane waves, where the outgoing angle depends on the lateral position of the underlying emitters in the focal plane. This angular divergence of the incoming photons on the grating leads to a significant reduction of the energy resolution. In our proposed setup, the spectral resolution could not be improved compared to the 2D IDI setup.
Finally, the use of a grating in the SIDI setup leads to a significant loss of photons in other diffraction orders. Hence, the 1D IDI approach was tested as an alternative to achieve the highest possible photons counts per frame. With this setup, it was possible to get first signatures of a 1D $g^{(2)}$-signal from the YAG:Ce crystal outside the cross-talk area.

Chapter 6

Conclusion

This thesis presents three major advances in lensless fluorescence imaging. First, it demonstrates the first true imaging of single nanoparticles smaller than the X-ray beam using *Incoherent Diffractive Imaging* (IDI), achieving a resolution of 20 nm — more than ten times better than previously reported by Inoue *et al.* [39] and Trost *et al.* [40]. This was accomplished while requiring significantly fewer shots, owing to improved detector placement and shorter incident pulses. However, high incident fluences did not enhance the $g^{(2)}$-signal. The spatial Hanbury Brown & Twiss [30] approach confirmed a fluence-dependent reduction of the visibility. We hypothesize that this reduction arises from *amplified spontaneous emission* (ASE), which may reduce the visibility without affecting speckle contrast. Indeed, the speckle contrast remained constant regardless of the incident pulse duration, suggesting that pulse energy per spike, rather than total pulse duration, governs absorption changes. Finally, this study reports the first observation of nonlinear saturable absorption and reverse saturable absorption in single copper nanoparticles, confirming a fluence-dependent response on femtosecond timescales [90].
Our results indicate self-gating at incident fluences of $\Phi > 1 \times 10^{17}\,\mathrm{W/cm^2}$, which is two orders of magnitude lower than reported by Inoue *et al.* [85] for a 10 µm-thick copper foil ($\Phi > 1 \times 10^{19}\,\mathrm{W/cm^2}$). This difference is likely due to the significantly smaller size of the copper nanoparticles in our study, which are much smaller than the product of the pulse duration and the speed of light (900 nm). Furthermore, Inoue *et al.* [85] report a reduction in self-gating for thinner foils ($\sim 5\,\mu\mathrm{m}$), which is opposite to our finding of strong self-gating in nanoparticles. However, their samples are still considered thick compared to the pulse length. The same reasoning applies to our hypothesis of ASE. For thick samples, such as foils, the volume of the sample that becomes population-inverted by the incident

X-ray pulse is highly anisotropic, as the pulse can only induce inversion along the direction of incidence. With a fluorescence lifetime of approximately 0.3 fs, which is much shorter than the incident pulse duration, ASE will predominantly occur in the forward direction that is freshly pumped. In contrast, for small nanoparticles such as those examined here, population inversion is created uniformly across the sample, and ASE is thus expected to be isotropic. Consequently, to understand the fundamental processes of nonlinear light-matter interactions at the nanoscale, it is crucial to study small particles, as they exhibit fundamentally different behavior from bulk materials.

With the advent of 200 µJ scale attosecond hard X-ray pulses [74], it is now possible to outrun nonlinear absorption effects as these ultra-short pulse durations are shorter than the timescales of electron damage caused by Auger decay [14, 90]. However, nonlinear emission phenomena like ASE will likely remain unaffected by these short pulse durations and pose significant challenges towards the ultimate goal of single-shot IDI, which includes orientation determination based on a frame-wise intensity correlation. This may set a fundamental limit to the efficiency of IDI when the coherent effect becomes dominant over spontaneous fluorescence. Consequently, it is favorable to stay within the linear emission regime and focus on improving the energy resolution of the imaging system. Such a spectrally resolved implementation of IDI (SIDI) was introduced in the second part of this work. SIDI is capable of performing lensless fluorescence-based imaging of structures with heterogeneous oxidation states for each spectral state independently. Here, IDI is combined with a spectral analyzer similar to XES or RIXS. This enhanced insight comes at the expense of sacrificing one spatial dimension in comparison to conventional IDI. Utilizing a single detector restricts imaging to one dimension, but owing to the isotropic nature of fluorescence emission, the detector can be positioned in any suitable orientation, and a second or even third crystal-detector pair can be used to probe the orthogonal spatial dimensions. The superior energy resolution of SIDI, in comparison to conventional IDI, not only results in improved $g^{(2)}$-contrast but also expands the maximum feasible transverse sample size to beyond a micrometer, overcoming a seemingly fundamental limit in conventional IDI set by the small coherence length and high signal requirements [37]. With its oxidation-sensitive imaging, SIDI provides additional insights beyond the conventional approach of combining coherent diffraction and XES, where the spectrum and the total emitter distributions are acquired, yet the precise emitter oxidation configuration inside the scattering particle is not revealed. Furthermore, SIDI could be used to validate the hypothesis of ASE in chapter 3, as this would,

on average, lead to a relative amplification of the $K_{\alpha 1}$ emission line. While the simulations presented here were performed for manganese, the approach of analyzing the fundamental emission and coherence properties of the K_α emission lines is equally applicable to other elements. In the case of oxidation state sensitive imaging, this technique is applicable for materials that exhibit either a shift of the central emission energy or a line broadening for different oxidation states. In the latter case, the edges of the emission lines would exhibit a different spatial profile than the central region of the emission line.

For single particle imaging applications, as discussed in chapter 3, where each pulse probes a different particle, coherent diffraction can be employed to determine the particle orientation in the case of non-spherical samples [18]. This orientation determination cannot be achieved using IDI alone, as the $g^{(2)}$-contrast is typically too low in a single shot. Moreover, SIDI yields only one-dimensional spatial information, which is insufficient for resolving orientation. However, with each two-dimensional coherent diffraction pattern, additional one-dimensional $g^{(2)}(q, E)$-profiles can be obtained, which are sensitive to the electronic configurations of subdomains within heterogeneous particles.

Our proposed methods open avenues for time-resolved, element specific and oxidation state-specific X-ray imaging of electron transfer in 3d-transition metal compounds or to study heterogeneous catalysts and battery materials where the nanoscale spatial distribution of elemental oxidation states are crucial for understanding function. Overall, our findings underscore the complexity and importance of understanding light-matter interactions at the nanoscale under extreme conditions in the X-ray regime. There is a clear need for comprehensive studies across a broad range of incident fluences and photon energies near the absorption K-edge. As our understanding of the underlying atomic processes improves, we are confident that our techniques will establish a new benchmark for the complex analysis of X-ray fluorescence and will serve for a wide range of applications within attosecond X-ray science.

The third part of this work discussed the prospects of extending IDI and SIDI to the visible regime at room temperature. These techniques could enable spatially resolved sensing of the local chemical environment at the nanoscale, offering new opportunities for studying material properties. However, the implementation of IDI and SIDI in the visible regime presents several challenges. Most importantly, due to the broad emission profiles of most samples at room temperature [28, 115], the coherence time of the fluorescence is on the order of femtoseconds, which is

significantly shorter than the temporal resolution achievable with single photon detectors. Typically, such detectors have temporal resolutions in the microsecond range (EMCCDs [112]), or in the nanosecond range for MCP-gated detectors such as the one used in this work. Recent advances in detector technology, such as SPADs [113] and the *Timepix4* [114], have enabled temporal resolutions in the picosecond range. However, these detectors are not yet widely available. Even with such improvements, the applicability of IDI in the visible regime remains limited due to the mismatch between fluorescence lifetimes (∼ns) and coherence times (on the order of femtoseconds to picoseconds), with ratios on the order of $\sim 1 \times 10^4$. Shortening the measurement time to match the coherence time would drastically reduce the signal levels. This stands in contrast to the X-ray regime, where the coherence times are even shorter ($< 1\,\mathrm{fs}$), but fluorescence lifetimes are on comparable timescales. Consequently, reducing the measurement time via shorter incident pulse durations can improve the performance of IDI in the X-ray regime without causing the same signal loss constraints as in the visible regime. A similar trade-off applies to the use of emission filters, which could, in principle, extend the coherence time but would also reduce the detected signal.

These limitations were addressed by implementing the spectrally resolved (SIDI) approach in the visible regime. However, our results indicate that this technique is incompatible with using objectives with high magnifications, as these lead to a significant reduction in the energy resolution.

Even the most promising materials, such as lead halide perovskite quantum dots [107], do not exhibit sufficiently narrow emission lines at room temperature to be suitable for IDI. Consequently, achieving the original goal of using IDI for optical sensing appears only feasible at cryogenic temperatures, where the emission lines approach the lifetime-limited regime [116]. A particularly promising platform is nitrogen-vacancy centers in diamond, where phenomena such as heterogeneous broadening and spectral diffusion — time-dependent fluctuations in the emission lines of individual emitters — can now be effectively controlled [117, 118].

Appendix A

The Nature of Hard X-Ray Fluorescence from Nanoparticles under Extreme Conditions

A.1 Sample preparation

Authors Contributions:
Sarodi Jonak Dutta: Sample preparation (lead)

Copper(II) sulfate pentahydrate ($CuSO_4.5H_2O \geq 99\%$), (+)-sodium L-ascorbate ($\geq$ 98%), and sodium dodecyl sulfate (SDS, $\geq$ 98.5%) were purchased from Sigma-Aldrich (USA). Sodium hydroxide (NaOH, $\geq$ 99%) was obtained from Roth (Germany). Ethanol (denat., $\geq$ 96%) was bought from VWR (USA). α-Methoxypoly(ethylene glycol)-ω-(11-mercaptoundecanoate) (PEGMUA:2 kDa, $M_n = 2000\,g\,mol^{-1}$ or 5 kDa, $M_n = 5000\,g\,mol^{-1}$) was synthesized as described by Schulz *et al.* [119]. Ultrapure water (18.2 MΩ, Millipore) was used for all procedures.

Copper(I) oxide (Cu_2O) nanocubes (NCs) were synthesized based on the protocol presented Thoka *et al.* [120], which was upscaled 25-fold to achieve a higher Cu_2O NCs concentration. For the synthesis, SDS (1.44 g, 5 mmol) was dissolved in 239 mL of ultrapure water and the solution was stirred for 5 min. Then $Cu_2SO_4{\cdot}5H_2O$ (2.5 mL, 0.1 M) and NaOH (1 mL, 1.0 M) were added under constant stirring. The solution turned light bluish after a few seconds which confirmed the formation of $Cu(OH)_2$. To that sodium ascorbate (7.5 mL, 0.2 M) was added, and

the mixture stirred for another 5 minutes. Subsequently, an undisturbed aging for 10 minutes was required for the crystal growth and the solution turned bright orange. The particles were centrifuged at 9500 g_0 for 10 min and further washed (9500 g_0 x 3 x 10 minutes) with a 1:1 volume ratio of water and ethanol. Finally, the Cu_2O NCs were dissolved in 10 mL of ethanol.

Cu_2O NCs were functionalized by adding PEGMUA (2 kDa or 5 kDa, 10 mL, 1 mM) to the freshly prepared NCs. The solution was stirred overnight followed by further purification (9500 g_0 x 3 x 10 minutes). At the end, the solution was concentrated to a volume of 1 mL.

A.2 Theoretical modelling of RSA

Authors Contributions:
Sebastian Cardoch: Theory (lead)

The copper nanoparticles are modeled as a one-dimensional 88 nm-thick system with a density of 8.96 g/cm^3 and initial temperature of 0.025 eV. The atomic data expends to $n \leq 3, l \leq 2$ and $n = 4, l = 0$ quantum numbers with at most one excitation from the K- and L-shell and two excitations from the M-shell. We use a *Steward-Pyatt* continuum lowering model [121] that is scaled by a factor of 0.53 to achieve Cu^{1+} ionization, approximating copper's conduction band at room temperature, at the beginning of the simulation. The X-ray pulse is described temporally as a Gaussian with a full width at half maximum of 2.5 fs (short) and 25 fs (long) duration, and energetically as a flat-top profile with 0.1 % bandwidth. Photon energies are shifted by 17 eV to match the atomic model's K-edge to its tabulated value [57]. The temperature of free electrons follows a *Maxwell Boltzmann* distribution. Radiation transport is solved over a coarse energy grid consisting of 100 logarithmically-spaced points that span from 0.1 eV to 1×10^4 eV. To resolve finer details around the Cu K-edge, we include an additional logarithmically-spaced grid of 100 points between 7.8 keV to 9.2 keV. Using converged solutions, the code computes a higher 1.3 eV-resolution spectrum of the K_α emission region, which we use to calculate fluorescence intensities. The total fluorescence is obtained by assuming a detector solid angle of 8 % and a K_α transmission of 40 % through the nickel foil.

Appendix B

Nanoscale X-Ray Imaging with High Spectral Sensitivity Using Fluorescence Intensity Correlations

B.1 Signal estimation

The intensity $I(k, E)$ on the detector for a particular fluorescence channel in number of photons can be calculated as follows:

$$I(k, E) = I_0 \, \sigma_{\text{abs}} \, \Phi \, N \, \Omega \, \tilde{S}(E), \tag{B.1}$$

where I_0 is the incident fluence, σ_{abs} is the absorption cross-section for a single atom, Φ is the fluorescence yield of the given emission line, N is the number of scattering atoms and Ω is the effective solid angle of the detector, taking into account that the silicon crystal is placed 300 mm from the interaction point and that only a small strip of the crystal is reflective for a given energy. $\tilde{S}(E)$ is again the normalized Lorentzian spectral profile. The intensity is independent of the vertical position on the detector, k.

We considered a 100 µJ X-ray pulse focussed to a 300 nm spot, yielding a fluence of 1.34×10^{12} ph/µm^2. This yields on average 5.47 absorption events per atom [57], so we assumed saturated absorption i.e. $I_0 \sigma_{\text{abs}} = 1$ in Eq. B.1.

For a 300 nm particle, the number of absorbing atoms is 2.6×10^9. The tabulated fluorescence yield values of $\Phi_\alpha = 0.27$ and $\Phi_\beta = 0.038$ were used for each simulation [122]. The effective solid angles of the detector are $\Omega_\alpha = 5.76 \times 10^{-6}$ sr and $\Omega_\beta = 2.56 \times 10^{-6}$ sr for a detector distance of 1 m and 1.5 m, respectively.

Appendix C

Perspectives for Optical Sensing at Room Temperature Using Fluorescence Intensity Correlations

Table C.1: Experimental run summary and setup configurations.

#	Date	ID	Fluorescence	Diffraction	Spectral	Objective	BP filter	# shots	Description
1	2023-01-20	3	no	no	no	100x	-	1	Imaging grating diffraction on GGD
2	2023-01-20	4	no	yes	no	100x	-	1	2D far field
3	2023-04-13	2	yes	no	no	100x	4 nm	1	Imaging grating diffraction on slide
4	2023-04-13	3	yes	yes	no	100x	4 nm	2 000 000	2D far field
5	2023-05-04	0	yes	no	no	100x	0.2 nm	1	Imaging on 50 µm YAG:Ce
6	2023-05-11	2	yes	yes	no	100x	0.2 nm	14 200 000	2D far field
7	2022-11-15	11	no	no	no	10x	-	1	Imaging grating diffraction on GGD
8	2022-11-15	10	no	yes	yes	10x	-	1	1D spectral far field
9	2022-11-15	12	no	no	no	10x	-	1	Imaging grating diffraction on GGD
10	2022-11-15	13	no	yes	yes	10x	-	1	1D spectral far field
11	2022-11-15	14	no	no	no	10x	-	1	Imaging grating diffraction on GGD
12	2022-11-15	15	no	yes	yes	10x	-	1	1D spectral far field
13	2022-12-01	12	yes	no	no	10x	-	1	Imaging focus on slide
14	2022-11-29	3	yes	yes	yes	10x	-	250 000	1D spectral far field
15	2023-12-14	0	yes	no	no	100x, oil	4 nm	1	Imaging focus on YAG:Ce
16	2023-12-14	1	yes	yes	no	100x, oil	4 nm	500 000	1D far field

Bibliography

1. Henderson, R. The potential and limitations of neutrons, electrons and X-rays for atomic resolution microscopy of unstained biological molecules. *Quarterly Reviews of Biophysics* **28,** 171–193 (1995).
2. Miao, J., Charalambous, P., Kirz, J. & Sayre, D. Extending the methodology of X-ray crystallography to allow imaging of micrometre-sized non-crystalline specimens. *Nature* **400,** 342–344 (1999).
3. Sakdinawat, A. & Attwood, D. Nanoscale X-ray imaging. *Nature photonics* **4,** 840–848 (2010).
4. Rodenburg, J. M. *et al.* Hard-x-ray lensless imaging of extended objects. *Physical review letters* **98,** 034801 (2007).
5. Chapman, H. N. & Nugent, K. A. Coherent lensless X-ray imaging. *Nature photonics* **4,** 833–839 (2010).
6. Kendrew, J. C. *et al.* A three-dimensional model of the myoglobin molecule obtained by x-ray analysis. *Nature* **181,** 662–666 (1958).
7. Shi, Y. A glimpse of structural biology through X-ray crystallography. *Cell* **159,** 995–1014 (2014).
8. Miao, J., Ishikawa, T., Robinson, I. K. & Murnane, M. M. Beyond crystallography: Diffractive imaging using coherent x-ray light sources. *Science* **348,** 530–535 (2015).
9. Pfeiffer, F. X-ray ptychography. *Nature Photonics* **12,** 9–17 (2018).
10. Chapman, H. N. *et al.* Femtosecond X-ray protein nanocrystallography. *Nature* **470,** 73–77 (2011).

11. Debye, P. Interferenz von röntgenstrahlen und wärmebewegung. *Annalen der Physik* **348,** 49–92 (1913).

12. Neutze, R., Wouts, R., Van der Spoel, D., Weckert, E. & Hajdu, J. Potential for biomolecular imaging with femtosecond X-ray pulses. *Nature* **406,** 752–757 (2000).

13. Howells, M. R. *et al.* An assessment of the resolution limitation due to radiation-damage in x-ray diffraction microscopy. *Journal of electron spectroscopy and related phenomena* **170,** 4–12 (2009).

14. Caleman, C. *et al.* On the feasibility of nanocrystal imaging using intense and ultrashort X-ray pulses. *ACS nano* **5,** 139–146 (2011).

15. Emma, P. *et al.* First lasing and operation of an ångstrom-wavelength free-electron laser. *nature photonics* **4,** 641–647 (2010).

16. Decking, W. *et al.* A MHz-repetition-rate hard X-ray free-electron laser driven by a superconducting linear accelerator. *Nature photonics* **14,** 391–397 (2020).

17. Aquila, A. *et al.* The linac coherent light source single particle imaging road map. *Structural Dynamics* **2** (2015).

18. Ayyer, K. *et al.* 3D diffractive imaging of nanoparticle ensembles using an x-ray laser. *Optica* **8,** 15–23 (2021).

19. Seibert, M. M. *et al.* Single mimivirus particles intercepted and imaged with an X-ray laser. *Nature* **470,** 78–81 (2011).

20. Mall, A. *et al.* Observation of Aerosolization-induced Morphological Changes in Viral Capsids. *arXiv preprint arXiv:2407.11687* (2024).

21. Ekeberg, T. *et al.* Observation of a single protein by ultrafast X-ray diffraction. *Light: Science & Applications* **13,** 15 (2024).

22. Chapman, H. N. *et al.* Femtosecond diffractive imaging with a soft-X-ray free-electron laser. *Nature Physics* **2,** 839–843 (2006).

23. Bogan, M. J. *et al.* Single particle X-ray diffractive imaging. *Nano letters* **8,** 310–316 (2008).

24. Munke, A. *et al.* Coherent diffraction of single Rice Dwarf virus particles using hard X-rays at the Linac Coherent Light Source. *Scientific data* **3,** 1–12 (2016).

25. Ayyer, K., Lan, T.-Y., Elser, V. & Loh, N. D. Dragonfly: an implementation of the expand–maximize–compress algorithm for single-particle imaging. *Journal of applied crystallography* **49,** 1320–1335 (2016).

26. Sobolev, E. *et al.* Megahertz single-particle imaging at the European XFEL. *Communications Physics* **3,** 97 (2020).

27. Daurer, B. J. *et al.* Experimental strategies for imaging bioparticles with femtosecond hard X-ray pulses. *IUCrJ* **4,** 251–262 (2017).

28. Lichtman, J. W. & Conchello, J.-A. Fluorescence microscopy. *Nature methods* **2,** 910–919 (2005).

29. Slowik, J. M., Son, S.-K., Dixit, G., Jurek, Z. & Santra, R. Incoherent x-ray scattering in single molecule imaging. *New Journal of Physics* **16,** 073042 (2014).

30. Hanbury Brown, R. & Twiss, R. A Test of a new type of stellar interferometer on Sirius. *Nature* **178,** 1046–1048 (1956).

31. Brown, R. H. & Twiss, R. Q. Correlation between photons in two coherent beams of light. *Nature* **177,** 27–29 (1956).

32. Victor, T. W. *et al.* X-ray fluorescence nanotomography of single bacteria with a sub-15 nm beam. *Scientific reports* **8,** 13415 (2018).

33. Classen, A., Ayyer, K., Chapman, H. N., Röhlsberger, R. & von Zanthier, J. Incoherent diffractive imaging via intensity correlations of hard x rays. *Physical review letters* **119,** 053401 (2017).

34. Sayers, D. E., Stern, E. A. & Lytle, F. W. New technique for investigating noncrystalline structures: Fourier analysis of the extended x-ray—absorption fine structure. *Physical review letters* **27,** 1204 (1971).

35. Kuzmin, A. & Chaboy, J. EXAFS and XANES analysis of oxides at the nanoscale. *IUCrJ* **1,** 571–589 (2014).

36. Trost, F., Ayyer, K. & Chapman, H. N. Photon statistics and signal to noise ratio for incoherent diffraction imaging. *New Journal of Physics* **22,** 083070 (2020).

37. Lohse, L. M., Vassholz, M. & Salditt, T. On incoherent diffractive imaging. *Acta Crystallographica Section A: Foundations and Advances* **77,** 480–496 (2021).

38. Nakamura, N. *et al.* Focus characterization of an X-ray free-electron laser by intensity correlation measurement of X-ray fluorescence. *Journal of Synchrotron Radiation* **27,** 1366–1371 (2020).

39. Inoue, I., Tamasaku, K., Osaka, T., Inubushi, Y. & Yabashi, M. Determination of X-ray pulse duration via intensity correlation measurements of X-ray fluorescence. *Journal of synchrotron radiation* **26,** 2050–2054 (2019).

40. Trost, F. *et al.* Imaging via correlation of x-ray fluorescence photons. *Physical Review Letters* **130,** 173201 (2023).

41. Heintzmann, R. & Huser, T. Super-resolution structured illumination microscopy. *Chemical reviews* **117,** 13890–13908 (2017).

42. Hell, S. W. & Wichmann, J. Breaking the diffraction resolution limit by stimulated emission: stimulated-emission-depletion fluorescence microscopy. *Optics letters* **19,** 780–782 (1994).

43. Balzarotti, F. *et al.* Nanometer resolution imaging and tracking of fluorescent molecules with minimal photon fluxes. *Science* **355,** 606–612 (2017).

44. Sreenithya, A., Kolganov, A. A., Yeu, I. W., Risansyauqi, M. H. & Pidko, E. A. Oxidation State of Single-Atom Re/TiO2 Hydrogenation Catalysts: A Computational Study. *ACS Catalysis* **14,** 18488–18498 (2024).

45. Zhu, X. *et al.* Direct observation of lithium-ion transport under an electrical field in LixCoO2 nanograins. *Scientific reports* **3,** 1084 (2013).

46. Sahm, C. D. *et al.* Tuning the local chemical environment of ZnSe quantum dots with dithiols towards photocatalytic CO 2 reduction. *Chemical Science* **13,** 5988–5998 (2022).

47. Wollweber, T. & Ayyer, K. Nanoscale x-ray imaging with high spectral sensitivity using fluorescence intensity correlations. *Structural Dynamics* **11** (2024).

48. Paganin, D. *Coherent X-ray optics* **6** (Oxford University Press, 2006).

49. Als-Nielsen, J. & McMorrow, D. *Elements of modern X-ray physics* (John Wiley & Sons, 2011).

50. SCHRÖDINGJSR, E. 2. Quantisierung als Eigenwertproblem. *Annalen der physik* **79,** 361 (1926).

51. Born, M. Quantenmechanik der stoßvorgänge. *Zeitschrift für physik* **38,** 803–827 (1926).

52. Ekstein, H. Connection between the kinematic and dynamical theories of x-ray diffraction. *Physical Review* **62,** 255 (1942).

53. Trost, F. *Imaging via photon-photon correlation of X-ray fluorescence* (Universitaet Hamburg (Germany), 2023).

54. Fienup, J. R. Reconstruction of an object from the modulus of its Fourier transform. *Optics letters* **3,** 27–29 (1978).

55. Fienup, J. R. Phase retrieval algorithms: a comparison. *Applied optics* **21,** 2758–2769 (1982).

56. Hölzer, G., Fritsch, M., Deutsch, M., Härtwig, J. & Förster, E. K α 1, 2 and K β 1, 3 x-ray emission lines of the 3 d transition metals. *Physical Review A* **56,** 4554 (1997).

57. Henke, B. L., Gullikson, E. M. & Davis, J. C. X-ray interactions: photoabsorption, scattering, transmission, and reflection at E= 50-30,000 eV, Z= 1-92. *Atomic data and nuclear data tables* **54,** 181–342 (1993).

58. Krause, M. O. & Oliver, J. Natural widths of atomic K and L levels, K α X-ray lines and several KLL Auger lines. *Journal of Physical and Chemical Reference Data* **8,** 329–338 (1979).

59. Loh, N.-T. D. & Elser, V. Reconstruction algorithm for single-particle diffraction imaging experiments. *Physical Review E—Statistical, Nonlinear, and Soft Matter Physics* **80,** 026705 (2009).

60. Hoeing, D. *et al.* Time-resolved single-particle x-ray scattering reveals electron-density gradients as coherent plasmonic-nanoparticle-oscillation source. *Nano letters* **23,** 5943–5950 (2023).

61. Michelson, A. A. On the application of interference methods to astronomical measurements. *Astrophysical Journal, vol. 51, p. 257* **51,** 257 (1920).

62. Goodman, J. W. *Statistical optics* (John Wiley & Sons, 2015).

63. Zernike, F. The concept of degree of coherence and its application to optical problems. *Physica* **5,** 785–795 (1938).

64. Siegert, A. *On the fluctuations in signals returned by many independently moving scatterers* (Radiation Laboratory, Massachusetts Institute of Technology, 1943).

65. Schirhagl, R., Chang, K., Loretz, M. & Degen, C. L. Nitrogen-vacancy centers in diamond: nanoscale sensors for physics and biology. *Annual review of physical chemistry* **65,** 83–105 (2014).

66. Bourrellier, R. *et al.* Bright UV single photon emission at point defects in h-BN. *Nano letters* **16,** 4317–4321 (2016).

67. Merino, P., Große, C., Rosławska, A., Kuhnke, K. & Kern, K. Exciton dynamics of C60-based single-photon emitters explored by Hanbury Brown–Twiss scanning tunnelling microscopy. *Nature Communications* **6,** 8461 (2015).

68. Trost, F. *et al.* Speckle contrast of interfering fluorescence X-rays. *Journal of Synchrotron Radiation* **30** (2023).

69. Goodman, J. W. *Speckle phenomena in optics: theory and applications* (Roberts and Company Publishers, 2007).

70. Mancuso, A., Aquila, A., Borchers, G., Giewekemeyer, K. & Reimers, N. Scientific instrument single particles, clusters, and biomolecules (SPB). *XFEL. EU Technical Report,* 1–232 (2013).

71. Bielecki, J. *et al.* Electrospray sample injection for single-particle imaging with x-ray lasers. *Science Advances* **5,** eaav8801 (2019).

72. Kujala, N. *et al.* Hard x-ray single-shot spectrometer at the European X-ray Free-Electron Laser. *Review of Scientific Instruments* **91** (2020).

73. Henrich, B. *et al.* The adaptive gain integrating pixel detector AGIPD a detector for the European XFEL. *Nuclear Instruments and Methods in Physics Research Section A: Accelerators, Spectrometers, Detectors and Associated Equipment* **633,** S11–S14 (2011).

74. Yan, J. *et al.* Terawatt-attosecond hard X-ray free-electron laser at high repetition rate. *Nature Photonics,* 1–6 (2024).

75. Yoneda, H. *et al.* Atomic inner-shell laser at 1.5-ångström wavelength pumped by an X-ray free-electron laser. *Nature* **524,** 446–449 (2015).

76. Benediktovitch, A. *et al.* Amplified spontaneous emission in the extreme ultraviolet by expanding xenon clusters. *Physical Review A* **101,** 063412 (2020).

77. Melnikov, S., Sinyanskii, A., Sizov, A. & Miley, G. H. *Lasers with nuclear pumping* (Springer, 2015).

78. Rudek, B. *et al.* Relativistic and resonant effects in the ionization of heavy atoms by ultra-intense hard X-rays. *Nature communications* **9,** 4200 (2018).

79. Ho, P. J. *et al.* The role of transient resonances for ultra-fast imaging of single sucrose nanoclusters. *Nature communications* **11,** 167 (2020).

80. Mercadier, L. *et al.* Transient absorption of warm dense matter created by an X-ray free-electron laser. *Nature Physics* **20,** 1564–1569 (2024).

81. Young, L. *et al.* Femtosecond electronic response of atoms to ultra-intense X-rays. *Nature* **466,** 56–61 (2010).

82. Whitcher, T. Turning solid aluminium transparent by intense soft X-ray photoionization (2009).

83. Yoneda, H. *et al.* Saturable absorption of intense hard X-rays in iron. *Nature communications* **5,** 5080 (2014).

84. Rackstraw, D. *et al.* Saturable absorption of an x-ray free-electron-laser heated solid-density aluminum plasma. *Physical review letters* **114,** 015003 (2015).

85. Inoue, I. *et al.* Shortening x-ray pulse duration via saturable absorption. *Physical Review Letters* **127,** 163903 (2021).

86. Cho, B. *et al.* Observation of reverse saturable absorption of an x-ray laser. *Physical Review Letters* **119,** 075002 (2017).

87. Wu, B. *et al.* Elimination of X-ray diffraction through stimulated X-ray transmission. *Physical review letters* **117,** 027401 (2016).

88. Kuschel, S. *et al.* Non-linear enhancement of ultrafast X-ray diffraction through transient resonances. *Nature Communications* **16,** 847 (2025).

89. Rohringer, N. & Santra, R. X-ray nonlinear optical processes using a self-amplified spontaneous emission free-electron laser. *Physical Review A—Atomic, Molecular, and Optical Physics* **76,** 033416 (2007).

90. Cardoch, S. *et al.* Decreasing ultrafast x-ray pulse durations with saturable absorption and resonant transitions. *Physical Review E* **107,** 015205 (2023).

91. Son, S.-K., Chapman, H. N. & Santra, R. Multiwavelength anomalous diffraction at high X-ray intensity. *Physical review letters* **107,** 218102 (2011).

92. Scott, H. A. & Mayle, R. W. GLF - A simulation code for X-ray lasers. *Applied Physics B* **58,** 35–43. ISSN: 1432-0649 (Jan. 1994).

93. Scott, H. A. Cretin—a radiative transfer capability for laboratory plasmas. *Radiative Properties of Hot Dense Matter* **71,** 689–701. ISSN: 0022-4073 (Oct. 2001).

94. Gu, M. F. The flexible atomic code. *Canadian Journal of Physics* **86.** Publisher: NRC Research Press, 675–689. ISSN: 0008-4204 (May 2008).

95. Zimmermann, P. *et al.* Modern X-ray spectroscopy: XAS and XES in the laboratory. *Coordination Chemistry Reviews* **423,** 213466 (2020).

96. Geoghegan, B. L. *et al.* Combining valence-to-core x-ray emission and Cu k-edge x-ray absorption spectroscopies to experimentally assess oxidation state in organometallic Cu (I)/(II)/(III) complexes. *Journal of the American Chemical Society* **144,** 2520–2534 (2022).

97. Martin-Diaconescu, V. *et al.* Kβ valence to core X-ray emission studies of Cu (i) binding proteins with mixed methionine–histidine coordination. Relevance to the reactivity of the M-and H-sites of peptidylglycine monooxygenase. *Inorganic chemistry* **55,** 3431–3439 (2016).

98. Kern, J. *et al.* Simultaneous femtosecond X-ray spectroscopy and diffraction of photosystem II at room temperature. *Science* **340,** 491–495 (2013).

99. Makita, H., Simon, P. S., Kern, J., Yano, J. & Yachandra, V. K. Combining on-line spectroscopy with synchrotron and X-ray free electron laser crystallography. *Current Opinion in Structural Biology* **80,** 102604 (2023).

100. Gog, T. *et al.* Spherical analyzers and monochromators for resonant inelastic hard X-ray scattering: a compilation of crystals and reflections. *Journal of synchrotron radiation* **20,** 74–79 (2013).

101. Peng, G. *et al.* High-resolution manganese x-ray fluorescence spectroscopy. Oxidation-state and spin-state sensitivity. *Journal of the American Chemical Society* **116,** 2914–2920 (1994).

102. Katz, O., Heidmann, P., Fink, M. & Gigan, S. Non-invasive single-shot imaging through scattering layers and around corners via speckle correlations. *Nature photonics* **8,** 784–790 (2014).

103. Lee, C.-H. *et al.* Coherent two-photon LIDAR with incoherent light. *Physical Review Letters* **131,** 223602 (2023).

104. Liu, L.-C. *et al.* Active optical intensity interferometry. *Physical Review Letters* **134,** 180201 (2025).

105. Huang, B., Bates, M. & Zhuang, X. Super-resolution fluorescence microscopy. *Annual review of biochemistry* **78,** 993–1016 (2009).

106. Göttfert, F. *et al.* Coaligned dual-channel STED nanoscopy and molecular diffusion analysis at 20 nm resolution. *Biophysical journal* **105,** L01–L03 (2013).

107. Utzat, H. *et al.* Coherent single-photon emission from colloidal lead halide perovskite quantum dots. *Science* **363,** 1068–1072 (2019).

108. Weber, M. Nonradiative decay from 5d states of rare earths in crystals. *Solid State Communications* **12,** 741–744 (1973).

109. Kolesov, R. *et al.* Mapping Spin Coherence of a Single Rare-Earth Ion in a Crystal onto a Single Photon¡? format?¿ Polarization State. *Physical review letters* **111,** 120502 (2013).

110. Lipka, M., Parniak, M. & Wasilewski, W. Microchannel plate cross-talk mitigation for spatial autocorrelation measurements. *Applied Physics Letters* **112** (2018).

111. Hooke, R. *Micrographia: or some physiological descriptions of minute bodies made by magnifying glasses, with observations and inquiries thereupon* (Courier Corporation, 2003).

112. Bestvater, F. *et al.* EMCCD-based spectrally resolved fluorescence correlation spectroscopy. *Optics express* **18,** 23818–23828 (2010).

113. Morimoto, K. *et al.* Megapixel time-gated SPAD image sensor¡? TeX\break?¿ for 2D and 3D imaging applications. *Optica* **7,** 346–354 (2020).

114. Llopart, X. *et al.* Timepix4, a large area pixel detector readout chip which can be tiled on 4 sides providing sub-200 ps timestamp binning. *Journal of Instrumentation* **17,** C01044 (2022).

115. Liang, P. *et al.* Room-temperature electron spin dynamics of Ce3+ ions in a YAG crystal. *Applied Physics Letters* **110** (2017).

116. Orphal-Kobin, L. *et al.* Optically coherent nitrogen-vacancy defect centers in diamond nanostructures. *Physical Review X* **13,** 011042 (2023).

117. Bernien, H. *et al.* Two-photon quantum interference from separate nitrogen vacancy centers in diamond. *Physical Review Letters* **108,** 043604 (2012).

118. Chu, Y. *et al.* Coherent optical transitions in implanted nitrogen vacancy centers. *Nano letters* **14,** 1982–1986 (2014).

119. Schulz, F., Vossmeyer, T., Bastús, N. G. & Weller, H. Effect of the spacer structure on the stability of gold nanoparticles functionalized with monodentate thiolated poly (ethylene glycol) ligands. *Langmuir* **29,** 9897–9908 (2013).

120. Thoka, S., Lee, A.-T. & Huang, M. H. Scalable synthesis of size-tunable small Cu2O nanocubes and octahedra for facet-dependent optical characterization and pseudomorphic conversion to Cu nanocrystals. *ACS Sustainable Chemistry & Engineering* **7,** 10467–10476 (2019).

121. Stewart, J. C. & Pyatt Jr., K. D. Lowering of Ionization Potentials in Plasmas. *The Astrophysical Journal* **144.** ADS Bibcode: 1966ApJ...144.1203S, 1203. ISSN: 0004-637X (June 1966).

122. Elam, W., Ravel, B. & Sieber, J. A new atomic database for X-ray spectroscopic calculations. *Radiation Physics and Chemistry* **63,** 121–128 (2002).

List of Publications

1. **T. Wollweber** and K. Ayyer, "Nanoscale x-ray imaging with high spectral sensitivity using fluorescence intensity correlations," Structural Dynamics, vol. 11, no. 2, Mar. 2024, AIP Publishing.

2. Z. Shen, M. Samoli, O. Erdem, J. Bielecki, A. K. Samanta, A. Estillore, C. Kim, Y. Kim, J. Koliyadu, R. Letrun, F. Locardi, J. Lübke, A. Mall, D. Melo, G. Mills, S. Rafie-Zinedine, A. Round, T. Sato, R. de Wijn, **T. Wollweber**, L. Worbs, Y. Zhuang, A. P. Mancuso, R. Bean, H. N. Chapman, J. Küpper, I. Infante, H. Lange, Z. Hens, K. Ayyer, "Direct observation of the exciton polaron by serial femtosecond crystallography on single CsPbBr quantum dots," arXiv preprint arXiv:2502.02343, Feb. 2025.

3. A. Mall, A. Munke, Z. Shen, P. Mazumder, J. Bielecki, A. Estillore, C. Kim, R. Letrun, J. Lübke, S. Rafie-Zinedine, A. Round, E. Round, M. Rütten, A. K. Samanta, A. Sarma, T. Sato, F. Schulz, C. Seuring, **T. Wollweber**, L. Worbs, P. Vagovic, R. Bean, A. P. Mancuso, N.-T. D. Loh, T. Beck, J. Küpper, F. R. N. C. Maia, H. N. Chapman, K. Ayyer, "Observation of Aerosolization-induced Morphological Changes in Viral Capsids," arXiv preprint arXiv:2407.11687, Jul. 2024.

4. Z. Shen, P. L. Xavier, R. Bean, J. Bielecki, M. Bergemann, B. J. Daurer, T. Ekeberg, A. D. Estillore, H. Fangohr, K. Giewekemeyer, M. Karnevskiy, R. A. Kirian, H. Kirkwood, Y. Kim, J. C. P. Koliyadu, H. Lange, R. Letrun, J. Lübke, A. Mall, T. Michelat, A. J. Morgan, N. Roth, A. K. Samanta, T. Sato, M. Sikorski, F. Schulz, P. Vagovic, **T. Wollweber**, L. Worbs, F. Maia, D. A. Horke, J. Küpper, A. P. Mancuso, H. N. Chapman, K. Ayyer, N. D. Loh, "Resolving Nonequilibrium Shape Variations among Millions of Gold Nanoparticles," ACS Nano, vol. 18, no. 24, pp. 15576–15589, May 2024.

5. T. Ekeberg, D. Assalauova, J. Bielecki, R. Boll, B. J. Daurer, L. A. Eichacker, L. E. Franken, D. E. Galli, L. Gelisio, L. Gumprecht, L. H. Gunn, J. Hajdu, R. Hartmann, D. Hasse, A. Ignatenko, J. Koliyadu, O. Kulyk, R. Kurta, M. Kuster, W. Lugmayr, J. Lübke, A. P. Mancuso, T. Mazza, C. Nettelblad, Y. Ovcharenko, D. E. Rivas, M. Rose, A. K. Samanta, P. Schmidt, E. Sobolev, N. Timneanu, S. Usenko, D. Westphal, **T. Wollweber**, L. Worbs, P. L. Xavier, H. Yousef, K. Ayyer, H. N. Chapman, J. A. Sellberg, C. Seuring, I.

A. Vartanyants, J. Küpper, M. Meyer, F. R. N. C. Maia, "Observation of a single protein by ultrafast X-ray diffraction," Light: Science & Applications, vol. 13, no. 1, pp. 15, Jan. 2024.

6. C. E. Blanchet, A. Round, H. D. T. Mertens, K. Ayyer, M. Graewert, S. Awel, D. Franke, K. Dörner, S. Bajt, R. Bean, T. F. Custódio, R. de Wijn, E. Juncheng, A. Henkel, A. Gruzinov, C. M. Jeffries, Y. Kim, H. Kirkwood, M. Kloos, J. Knoška, J. Koliyadu, R. Letrun, C. Löw, J. Makroczyova, A. Mall, R. Meijers, G. E. P. Murillo, D. Oberthür, E. Round, C. Seuring, M. Sikorski, P. Vagovic, J. Valerio, **T. Wollweber**, Y. Zhuang, J. Schulz, H. Haas, H. N. Chapman, A. P. Mancuso, and D. Svergun, "Form factor determination of biological molecules with X-ray free electron laser small-angle scattering (XFEL-SAS)," Commun. Biol., vol. 6, no. 1, p. 1057, Oct. 2023.

7. F. Trost, K. Ayyer, M. Prasciolu, H. Fleckenstein, M. Barthelmess, O. Yefanov, J. L. Dresselhaus, C. Li, S. Bajt, J. Carnis, **T. Wollweber**, A. Mall, Z. Shen, Y. Zhuang, S. Richter, S. Karl, S. Cardoch, K. K. Patra, J. Möller, A. Zozulya, R. Shayduk, W. Lu, F. Brauße, B. Friedrich, U. Boesenberg, I. Petrov, S. Tomin, M. Guetg, A. Madsen, N. Timneanu, C. Caleman, R. Röhlsberger, J. von Zanthier, and H. N. Chapman, "Imaging via correlation of x-ray fluorescence photons," Phys. Rev. Lett., vol. 130, no. 17, p. 173201, Apr. 2023.

8. Y. Zhuang, S. Awel, A. Barty, R. Bean, J. Bielecki, M. Bergemann, B. J. Daurer, T. Ekeberg, A. D. Estillore, H. Fangohr, K. Giewekemeyer, M. S. Hunter, M. Karnevskiy, R. A. Kirian, H. Kirkwood, Y. Kim, J. Koliyadu, H. Lange, R. Letrun, J. Lübke, A. Mall, T. Michelat, A. J. Morgan, N. Roth, A. K. Samanta, T. Sato, Z. Shen, M. Sikorski, F. Schulz, J. C. H. Spence, P. Vagovic, **T. Wollweber**, L. Worbs, P. L. Xavier, O. Yefanov, F. R. N. C. Maia, D. A. Horke, J. Küpper, N. D. Loh, A. P. Mancuso, H. N. Chapman, and K. Ayyer, "Unsupervised learning approaches to characterizing heterogeneous samples using X-ray single-particle imaging," IUCrJ, vol. 9, no. 2, pp. 204–214, Mar. 2022.

9. P. L. Xavier, K. Ayyer, J. Bielecki, Z. Shen, B. J. Daurer, A. K. Samanta, S. Awel, R. Bean, A. Barty, M. Bergemann, T. Ekeberg, A. D. Estillore, H. Fangohr, K. Giewekemeyer, M. S. Hunter, M. Karnevskiy, R. A. Kirian, H. Kirkwood, Y. Kim, J. Koliyadu, H. Lange, R. Letrun, J. Lübke, T. Michelat,

A. J. Morgan, N. Roth, T. Sato, M. Sikorski, F. Schulz, J. C. H. Spence, P. Vagovic, **T. Wollweber**, L. Worbs, O. Yefanov, Y. Zhuang, F. R. N. C. Maia, D. A. Horke, J. Küpper, N. D. Loh, A. P. Mancuso, and H. N. Chapman, "Sub-3 nm resolution 3D diffractive imaging of anisotropic gold nanoparticles with millions of patterns using MHz XFEL pulses," in Proc. WE-Heraeus-Seminar: Diffraction Limited Synchrotron Light Sources and Next Generation Free Electron Lasers, 2022.

10. K. Ayyer, P. L. Xavier, J. Bielecki, Z. Shen, B. J. Daurer, A. K. Samanta, S. Awel, R. Bean, A. Barty, M. Bergemann, T. Ekeberg, A. D. Estillore, H. Fangohr, K. Giewekemeyer, M. S. Hunter, M. Karnevskiy, R. A. Kirian, H. Kirkwood, Y. Kim, J. Koliyadu, H. Lange, R. Letrun, J. Lübke, T. Michelat, A. J. Morgan, N. Roth, T. Sato, M. Sikorski, F. Schulz, J. C. H. Spence, P. Vagovic, **T. Wollweber**, L. Worbs, O. Yefanov, Y. Zhuang, F. R. N. C. Maia, D. A. Horke, J. Küpper, N. D. Loh, A. P. Mancuso, and H. N. Chapman, "3D diffractive imaging of nanoparticle ensembles using an x-ray laser," Optica, vol. 8, no. 1, pp. 15–23, Dec. 2020.

List of Figures

1.1 Schematic showing the resolution gap between EXAFS and XFM techniques, and the potential of Incoherent Diffractive Imaging (IDI) to bridge this gap. EXAFS provides atomic-scale but locally limited information about the surrounding structure of a specific element, while the resolution in XFM is limited by the spot size of the focused X-ray beam ($\sim$ 10 nm) [32]. The gray dashed line indicates the quadratic relation between the object size and the resolving power, when scanning large 2D objects. IDI has the potential to provide high spatial resolution while maintaining elemental contrast, enabling dark-field imaging of substructures of a single element within heterostructures. 3

2.1 Atomic relaxation processes after photoionization: (**A**) Fluorescence emission and (**B**) Auger-Meitner-decay. (**C**) Characteristic X-ray fluorescence emission lines and their corresponding electronic energy levels for copper. 14

2.2 Ewald sphere construction. The incident and the scattered wave vectors $\boldsymbol{k}_0$ and $\boldsymbol{k}_f$ are shown in blue and the momentum transfer vector $\boldsymbol{q}$ is shown in red. The radius of the Ewald sphere is $1/\lambda$, where λ is the wavelength of the incident X-ray beam. 18

2.3 Schematic of the surface of the three-dimensional $g^{(2)}(\boldsymbol{q})$ function. . 24

3.1 Schematic of the experimental setup. The copper nanoparticles are aerosolized and injected into the interaction region by an electrospray [71]. The nickel foil filters the coherently scattered photons as well as the K_β emission at high scattering angles. The coherent diffraction at low-**k** can be used for orientation determination and classification. The coherence properties of the K_α fluorescence can then be studied for the filtered area on the detector. Simultaneously, the spectra of the incident X-ray pulses are recorded by the *High-resolution hard X-ray single-shot* (HIREX) spectrometer [72]. . 30

3.2 Exemplary *Dragonfly* 2D class averages for short pulses. The top row displays 5 class averages that were rejected after the first round of classification. The class averages in the bottom row correspond to the diffraction patterns contributing to the $g^{(2)}$-signal shown in Figure 3.7. 31

3.3 Estimation of the pulse duration. (**A**) Exemplary HIREX spectrum. (**B**) $g^{(2)}(\Delta E)$ for all spectra for a photon energy of 9170 eV. The full width at half maximum of the Gaussian fit can be used to calculate the incident pulse duration. 32

3.4 Mean $g^{(2)}$-value for the inner four non-masked voxels as a function of incoherent modes M. The comparison with the ground truth yields a correction factor of 1.18 to retrieve the visibility ν at $q = 0$. 33

3.5 Simulations for fluctuating incident fluences for $M = 1$ (top row) and $M = 20$ (bottom row). (**A, C**) Intensity fluctuation dependence of the low-q mean $g^{(2)}$-value and the offset $\mathcal{O}$. (**B, D**) Comparing the two definitions for the visibility ν for fluctuating intensities. The conventional definition (blue) yields physically impossible visibilities ($\nu > 1$), whereas our new definition for ν (orange) converges to the expected values. 35

3.6 Visibility ν as a function of mean photon counts per pixel $\langle\mu\rangle$ for short pulses at 9170 eV. The green line shows the simulated results for 20 modes with the same background level (dashed blue line). The decrease of the visibility for high $\langle\mu\rangle$ shows the same qualitative (but reversed) *sigmoid* behavior (gray dashed line) as the rise for low $\langle\mu\rangle$. 36

3.7 (**A**) $g^{(2)}(\mathbf{q})$ from 5 similar *Dragonfly* class averages see (Fig. 3.2). (**B**) Horizontal line profile. 37

3.8 Electronic cascade leads to a shift of the absorption edge during the course of an XFEL pulse. The red dashed lines represent the three photon energies used in the scan across the tabulated absorption K-edge at 8978.9 eV (gray line) [57]. The energy 8910 eV lies near the K-to-M shell resonance, 9015 eV just above the K-edge, and 9170 eV well above the edge. 38

3.9 (Reverse) Saturable Absorption for short (top row) and long (bottom row) pulses as a function of incident fluence. (**A, D**) Fluorescence cross-sections for incident photon energies of 9015 eV and 9170 eV, exhibiting saturable absorption for higher fluences. (**B, E**) Total fluorescence emission shows a cross-over between the two energies, as indicated by the least-squares fits. (**C, F**) Total fluorescence emission for an excitation energy of 8910 eV and qualitative theoretical prediction, from collisional radiative simulations [92, 93] using relativistic configuration atomic data [94] (see Appendix A.2 for details), revealing reverse saturable absorption. 39

3.10 Speckle contrast of the K_α fluorescence as function of fluorescence signal per pixel μ for short (**A**) and long (**B**) pulses at 9015 eV and 9170 eV. The solid lines indicate the converged value of the speckle contrast for high μ. 41

4.1 Schematic of the *Spectral Incoherent Diffractive Imaging* (SIDI) setup. The silicon crystal analyzer disperses the emitted photons in one direction while acting as a simple mirror along the orthogonal dimension. Thus, the position of a detected photon on the two-dimensional detector in the far field corresponds to its energy and one component of its wave vector. 46

4.2 Integrated 2D detector image showing the two K_α lines of Mn. As expected, there is no structure along the k-axis. The inset in the upper right shows the projection of the spherical nanoparticle. . . . 48

4.3 K_α SIDI simulations. The top row shows the behavior for full phase correlation between the $K_{\alpha 1}$ and $K_{\alpha 2}$ wavefunctions, while the bottom row shows the case of no phase correlation. (**A, B**) $g^{(2)}(q, \Delta E)$ images obtained by averaging 2D intensity correlations for each exposure. (**C, D**) Z-score for the images in **A** and **B**, respectively. The horizontal profiles in (**A** − **D**) correspond to the central line cuts and the vertical profiles to the central (red) and the off-central cuts (blue) at a ΔE value of $E_{K_{\alpha 1}} - E_{K_{\alpha 2}}$. (**E, F**) $g^{(2)}(E, \Delta E)$-signal for $q = 2.14\,\mu m^{-1}$ showing a clear difference between the two cases. 50

4.4 Integrated 2D detector image showing the broadened K_β lines of the Mn-Mn^{2+} compound as well as coherent elastic scattering. One can already see the structure of the whole particle reflected in the coherent signal (dark profile to the right), while the fluorescence yields a flat profile (light green). 52

4.5 K_β simulations for the Mn-Mn^{2+} compound. (**A**) Intensity correlations $g^{(2)}(q, E)$ for each energy channel, i.e. for each pixel column of the detector independently, normalized by its standard deviation. Since the spatial distribution of each Mn subspecies differs (see inset in the upper right of Fig. 4.4), one can see different signals within the K_β line. (**B**) The energy-dependent line profiles along q for the two oxidation states can be used to independently reconstruct the structure of each state. 53

5.1 Schematic of the optical setup for 2D IDI in the visible regime. The sample is excited by a 450 nm circularly polarized laser pulse and the emitted fluorescence is collected by an infinity-corrected objective lens and subsequently filtered and directed towards the detector. The setup allows direct imaging of the focal plane of the objective via the tube lens, or, alternatively, imaging of the BFP using the so-called FT-lens. For details, see text. 57

5.2 Detector characterization (Run #4). (**A**) Integrated far-field fluorescence intensity from the slide. (**B**) Intensity correlation $g^{(2)}(\boldsymbol{q})$ and its radial profile (**C**). The central peak is due to the cross-talk of the MCP, while the horizontal line is a common mode effect. . . 59

5.3 Schematic of the MCP cross-talk within an intensified CMOS detector. The incoming photon hits the photocathode and generates a photoelectron. This electron is accelerated towards the MCP by an electric field, where it generates secondary electrons. These secondary electrons are then accelerated towards the phosphor screen, where they generate photons that are detected by the CMOS sensor. However, some secondary electrons can be scattered backwards and re-enter the MCP in a different channel, leading to a correlation of the detected signal on the CMOS sensor and thus to a peak in the second-order correlation function at low-q. 60

5.4 GGD verification (Runs #1 and #2). (**A**) Real-space beam profile of the incident beam on the GGD. (**B**) Corresponding $g^{(2)}(\boldsymbol{q})$, which exhibits interference fringes. 61

5.5 IDI of the fluorescent slide (Runs #3 and #4). (**A**) Real-space beam profile of the incident beam on the slide. (**B**) The fluorescence signal level decreases over time due to bleaching. (**C**) Integrated intensity of the whole measurement. (**D**) Gaussian filtered $g^{(2)}(\boldsymbol{q})$ of the first 100 000 frames, subtracted by the average $g^{(2)}(\boldsymbol{q})$ of the subsequent temporal bins, exhibiting the central speckle. 62

5.6 Fluorescence from YAG:Ce crystal (Runs #5 and #6). (**A**) Real-space beam profile of the incident beam on the YAG:Ce crystal. (**B**) Fluorescence signal level over the whole measurement. (**C**) Integrated fluorescence intensity. (**D**) 2D intensity correlation $g^{(2)}(\boldsymbol{q})$. 63

5.7 SIDI schematic setup, similar to the 2D IDI configuration. Here, a grating is placed downstream of the objective to spectrally disperse the fluorescence. The FT lens and the so-called spectral lens, which refocuses the photons according to their energy, are now cylindrical. 64

5.8 SIDI of the GGD (Runs #7−#12). Top row: Real-space beam profiles on the GGD. Bottom row: Corresponding intensity correlation function $g^{(2)}(q, \Delta E)$. 65

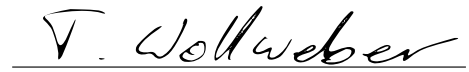
5.9 SIDI of the rotating fluorescent slide (Runs #13 and #14). (**A**) Real-space beam profile of the incident beam on the slide. (**B**) Integrated far field intensity. (**C**) Intensity correlation function $g^{(2)}(q, \Delta E)$. 66

5.10 1D IDI of YAG:Ce (Runs #15 and #16). (**A**) Real-space beam profile in the focal plane. (**B**) Integrated intensity of the fluorescence. Real-space imaging along the horizontal axis, and far-field intensity distribution along the vertical axis. (**C**). Intensity correlation function $g^{(2)}(q, \Delta x)$. (**D**) Vertical central line profile of $g^{(2)}(q, \Delta x)$. . 67

Eidesstattliche Versicherung

Hiermit versichere ich an Eides statt, die vorliegende Dissertationsschrift selbst verfasst und keine anderen als die angegebenen Hilfsmittel und Quellen benutzt zu haben.
Sofern im Zuge der Erstellung der vorliegenden Dissertationsschrift generative Künstliche Intelligenz (gKI) basierte elektronische Hilfsmittel verwendet wurden, versichere ich, dass meine eigene Leistung im Vordergrund stand und dass eine vollständige Dokumentation aller verwendeten Hilfsmittel gemäß der Guten wissenschaftlichen Praxis vorliegt. Ich trage die Verantwortung für eventuell durch die gKI generierte fehlerhafte oder verzerrte Inhalte, fehlerhafte Referenzen, Verstöße gegen das Datenschutz- und Urheberrecht oder Plagiate.

Hamburg, den 13. Oktober 2025



Lars Tamme Wollweber